Quantitative Imaging of the Choroid Plexus and the Blood-Brain Barrier with Arterial Spin Labeling MRI in Human Subjects

By

YUFEI DAVID ZHU
DISSERTATION

Submitted in partial satisfaction of the requirements for the degree of

DOCTOR OF PHILOSOPHY

in

Biomedical Engineering

in the

OFFICE OF GRADUATE STUDIES

of the

UNIVERSITY OF CALIFORNIA

DAVIS

Approved:

Audrey P. Fan (Chair)

Cameron S. Carter

Abhijit J. Chaudhari

Youngkyoo Jung

Tyler A. Lesh

Committee in Charge

2025

The Dissertation of Yufei David Zhu is approved, and it is acceptable in quality and form for publication on microfilm and electronically.

University of California Davis

2025

Dedication

To my family, who have guided
me toward a life of knowledge.

Table of Contents

List of Figures

List of Tables

List of Abbreviations

AD	Alzheimer's disease
ADRC	Alzheimer's disease research center
AIF	Arterial input function
AQP	Aquaporin
ASL	Arterial spin labeling
ATT	Arterial transit time
AUC	Area under curve
BBB	Blood-brain barrier
BCSFB	Blood-cerebrospinal fluid barrier
BOLD	Blood oxygen level dependent
CBF	Cerebral blood flow
ChP	Choroid plexus
CNS	Central nervous system
CPP	Cerebral perfusion pressure
CSF	Cerebrospinal fluid
CV	Coefficient of variation
CVR	Cerebrovascular reactivity
D	Diffusivity
DCE	Dynamic contrast enhanced
DSM	Diagnostic and Statistical Manual of Mental Disorders
DW	Diffusion-weighted
EES	Extravascular extracellular space
FDR	False discovery rate
FEAST	Flow encoding arterial spin tagging

fMRI	Functional magnetic resonance imaging
GBCA	Gadolinium-based contrast agents
GKM	General kinetic model
GLM	General linear model
GM	Gray matter
GRASE	Gradient and spin echo
ICA	Internal cerebral artery
ICC	Intraclass correlation coefficient
Kw	Water exchange rate
LD	Labeling duration
LH	Left hemisphere
ME	Multi-echo
MIA	Material immune activation
MPRAGE	Magnetization prepared rapid gradient echo
MRI	Magnetic resonance imaging
MNI	Montreal Neurological Institute
NaN	Not a number
NDV	Net displacement vector
NSF	Nephrogenic systemic fibrosis
PC	Pseudo-continuous
PCA	Posterior cerebral artery
PET	Positron emission tomography
PLD	Post-label delay
PVC	Partial volume correction
PS	Permeability-surface
QE	Qualifying exam

RF	Radio frequency
RH	Right hemisphere
ROI	Region of interest
SBD	Sub-bolus duration
SMC	Smooth muscle cell
SNR	Signal-to-noise ratio
SPA	Single pass approximation
T1	Longitudinal relaxation rate
T2	Transverse relaxation rate
TE	Echo time
Tex	Time of exchange
TGV	Total generalized variation
TI	Inflow time
TJ	Tight junction
TR	Time of repetition
WEQ	Water exchange quantification
ZO	Zonula occludin

Acknowledgements

I would like to acknowledge my primary supervisor and chair of the dissertation committee, Professor Audrey P. Fan, PhD, for her unwavering support and guidance throughout the past five years. Her expertise, optimism, and leadership made my experience here at the University of California, Davis pass by seamlessly and helped to solidify my foundational training as a research scientist in the field of MRI and brain imaging.

Chapter 3, in full, is a version of an unpublished manuscript where we investigated the ability of arterial spin labeling (MRI) to assess choroid plexus perfusion. I would like to acknowledge Moss Y. Zhao, DPhil, the late Bin Shen, PhD, and Professor Greg Zaharchuk, MD, PhD of Stanford University for their contributions and comments. Though this manuscript remains unpublished, the years of analysis put forth and the multiple drafts associated with undergoing the peer-review represent a project that introduced me to this field.

Chapter 4, in full, is a version of the manuscript that has been accepted to the journal, *Magnetic Resonance in Medicine*. I would like to acknowledge my colleague, Quimby N. Lee, for her comments and Professors Xingfeng Shao, PhD and Danny JJ Wang, PhD of the University of Southern California for their contributions and comments to this study. Additionally, I would like to thank Professor Youngkyoo Jung, PhD for his guidance on the simulation portions of this project.

Chapter 5, in full, is an early draft of a manuscript that we plan to submit to either the journal *Magnetic Resonance in Medicine* or *Journal of Magnetic Resonance Imaging*. The work presented here is ongoing and will continue past the submission of this dissertation. I would like to acknowledge my colleague Anjan Bhattarai, PhD and my undergraduate mentee, Barah Albuhwailah for their contributions to this study. I would also like to acknowledge Professors Xingfeng Shao, PhD and Danny JJ Wang, PhD of the University of Southern California along with Jan Petr, PhD, Klaus Eickel, PhD, and Matthias Günther, PhD of the DEBBIE consortium for their contributions and comments.

Chapter 6 is a preliminary analysis of the Conte Center schizophrenia study data. I would like to acknowledge Professors Cameron Carter, MD and Tyler A. Lesh, PhD for their guidance on this project

and for their co-mentorship on a two-year NIH TL1 Predoctoral Training Fellowship here at the University of California, Davis for which I was the recipient from 2023 to 2025.

I would also like to acknowledge Professors Ramsey Badawi, PhD and Felipe Godinez, PhD for agreeing to serve on my qualifying exam (QE) committee, thereby contributing to the overall structure and planning of this dissertation. I appreciate their time and expertise. Finally, I would like to acknowledge Professor Abhijit J. Chaudhari, PhD, who served on both my qualifying exam and thesis committee. His expert knowledge and warmth were most welcome during my time as a graduate student.

Vita

2011 Bachelor of Science in Biomedical Engineering, Washington University in St. Louis

2025 Doctor of Philosophy in Biomedical Engineering, University of California Davis

Publications

Zhu YD, Bhattarai A, Albuhwailah B, Shao X, Petr J, Eickel K, Gunther M, Wang DJJ, Fan AP. "Comparison of water exchange rate in young and elderly adults with diffusion prepared and multi-echo arterial spin labeling MRI" [In preparation]

Zhu YD, Lee QN, Shao X, Jung Y, Fan AP. "Repeatability of diffusion weighted arterial spin labeling MRI for mapping blood-brain barrier water exchange at different post-label delays" [Under Review at *Magnetic Resonance in Medicine*]

Pedrela B, Mahroo A, Tee M, Sneve MH, Moyaert P, Geier O, Kuijer JPA, Beun S, Nordhoy W, **Zhu YD**, et al. "Developing blood-brain barrier arterial spin labeling as a non-invasive early biomarker of Alzheimer's disease (DEBBIE-AD): a Prospective Observational Multicohort Study Protocol" *BMJ Open*. February 2024. https://doi.org/10.1136/bmjopen-2023-081635

Field of Study

Major Field: Biomedical Engineering

Studies in Arterial Spin Labeling MRI, Schizophrenia, and Aging

Professor Audrey P. Fan

Abstract of Dissertation

Quantitative Imaging of the Choroid Plexus and the Blood-Brain Barrier with Arterial Spin Labeling MRI in Human Subjects

by

Yufei David Zhu

Doctor of Philosophy in Biomedical Engineering

University of California Davis, 2025

Professor Audrey Fan, PhD (Chair)

The choroid plexus and blood-brain barrier are both structures that could offer insights into the mechanistic development of various neurological diseases. Here, we explore a relatively new noninvasive technique called arterial spin labeling MRI and its capacity to assess choroid plexus perfusion and water exchange rate across the blood-brain barrier as proxy measures for their functional status. We conclude that multi-delay arterial spin labeling is a promising technique to estimate markers of cerebral health. This is exciting given that arterial spin labeling is a water-based method that does not utilize any toxic contrast agents, thereby making this technique appropriate for use in both younger psychiatric populations and

research subjects that may require multiple scans. The work presented in this dissertation represents the foundational analysis that will support future studies to validate this relatively new usage of arterial spin labeling toward the care of patients in a clinical setting.

Introduction

This work sought to advance the utilization of a noninvasive, nonionizing and contrast-free MRI technique to study the clearance mechanisms of the human brain. Arterial spin labeling (ASL) MRI relies on magnetically labeled water molecules as tracers and has historically been used to assess cerebral perfusion. Recently, there has been efforts to model the water exchange rate (Kw) across the blood-brain barrier (BBB) as a proxy measure for its structural integrity and function. Our work sought to bring this relatively new technology to our institution, optimize important imaging parameters on our scanners, and test out this sequence in a cohort of psychiatric and aging participants with the intent of developing novel and clinically useful biomarkers to assess disease. Our preliminary data will support future studies at the University of California, Davis, which will further explore the utility of these BBB ASL techniques to assess neurodegenerative disorders, such as Alzheimer's disease.

Our work begins with two foundational background chapters to introduce the biological sciences and imaging technology. Chapter 3 is an introductory project that compares multi-delay ASL to the current gold standard in assessing cerebral perfusion, ^{15}O-water PET, and its ability to measure choroid plexus perfusion under baseline and with acetazolamide vasodilation conditions. Chapter 4 is an *in vivo* optimization and computer simulation study that explores the repeatability of the diffusion weighted (DW) ASL sequence at different post-label delay times. Chapter 5 is a comparison study of two major ASL techniques that assesses Kw across the BBB and applies it in a group of young healthy and another group of elderly healthy participants. Finally, Chapter 6 aims to apply the DW ASL technique in a group of participants with schizophrenia and seeks to correlate the regional Kw metric to different peripheral and central markers of inflammation.

The primary objective of this work is to bring these magnetically labeled water-based techniques to measure Kw across the BBB to our institution to set up further projects that will explore the potential of these methods to study diseases. The overall goal is toward the clinical adoptions of a novel,

noninvasive, nonionizing and contrast-free way to assess Kw across the BBB as a marker of cerebral vascular health.

Chapter 1 Biological Foundations

1.1 Glymphatic System

The glymphatic system is a recently discovered macroscopic waste clearance system in the brain that functions primarily during sleep and is largely inactive in wakefulness. It utilizes a unique network of perivascular tunnels, formed by astrocytes, to promote efficient elimination of soluble proteins and metabolites from the central nervous system (CNS). Additionally, the glymphatic system distributes several compounds, including glucose, lipids, amino acids, growth factors, and neuromodulators throughout the brain. [1] Clearance of excess fluid and interstitial solutes is critical to maintaining tissue homeostasis. The glymphatic system derives its name from the amalgamation of the words “glia” and “lymphatics”. In the peripheral space, the lymphatic network returns proteins and fluid from the interstitial space back to the general circulation. The lymph system extends throughout all parts of the peripheral tissues, and the density of lymph vessels correlates with the rate of tissue metabolism. Paradoxically, the CNS lack a distinct lymph system even though the brain and spinal cord are characterized by a disproportionally high metabolic rates and that neuronal synaptic transmission is very sensitive to changes in the surrounding milieu.

The glymphatic system relies primary on the perivascular space associated with the circulatory vessels. From the cortical surface, cerebral arteries extend into pial arteries running though the CSF-containing subarachnoid space and subpial space. As pial arteries dive down into the brain tissue they transition into penetrating arteries and create a perivascular space—known as the Virchow-Robin space—which are filled with cerebrospinal fluid (CSF) and bordered by a leptomeningeal cell layer on both the inner wall facing the vessel and on the outer wall facing perivascular astrocytic endfeet. A unique feature of CNS vessels is that astrocytic endfeet line all layers of cerebral vasculature including at the artery, arteriole, and capillary levels. At the capillary level, endothelial cells, pericytes and astrocytes all reside in or contact the basal lamina to form the blood-brain barrier component of the neurovascular unit (Figure

1.1). From the subarachnoid space, CSF is driven into the Virchow-Robin spaces through a combination of arterial pulsatility, respiration, slow vasomotion, and CSF pressure gradients.

CSF transport into the brain parenchyma is facilitated by aquaporin 4 (AQP4) water channels expressed in a highly polarized manner in astrocytic endfeet that ensheathe brain vessels. This movement of CSF into the brain tissue drives interstitial fluid toward the perivenous spaces surrounding the large deep veins where it then drains out of the brain toward the cervical lymphatic system. [2] Ultimately, all CSF drains into the venous circulatory system, either indirectly through the lymphatic system or directly via the arachnoid villi. It is this highly polarized—from arterial to venous—macroscopic system of convective fluid fluxes with rapid interchange of CSF and interstitial fluid that was coined the glymphatic system in a seminal 2012 study based on its similarity in function to the peripheral lymphatic system. [3]

Subsequently, researchers began to observe the important role that dysfunction of a macroscopic clearance mechanism of interstitial solute may have in the pathogenesis of neurodegenerative diseases, such as Alzheimer's, which is characterized by the accumulation of proteins, including amyloid plaques and tau tangles. In fact, Iliff et al. [3] showed in their landmark study that beta-amyloid was in fact cleared from the mouse brain along the glymphatic paravenous efflux pathways. Furthermore, imaging of CSF tracer movement in AQP4 knockout mice revealed a ~65% reduction in CSF fluid flux through the parenchyma compared to wildtype control mice and that clearance of intrastriatal injected radio-labeled beta-amyloid was reduced by ~55%. [3] Therefore, it was proposed that the paravascular glymphatic pathway driven largely by AQP4-dependent bulk flow constitutes a major clearance pathway of interstitial fluid solutes from the brain's parenchyma.

The novelty of this relatively new active area of research led the author to adopt the study of applying arterial spin labeling MRI to functionally assess structures complementary to the glymphatic system as the primary objective of this thesis work with the aim of developing of novel, quantitative and clinically useful neuroimaging biomarkers for the diagnosis and prognosis of different neurological and neuropsychiatric disorders.

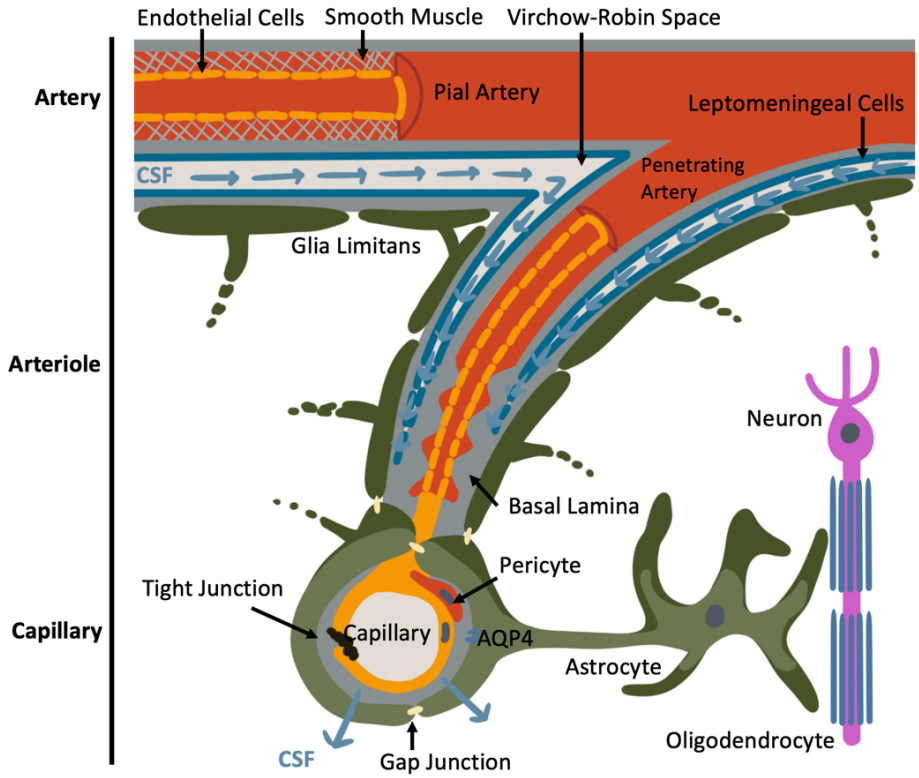

Figure 1.1: Arterial half of the glymphatic system. The neurovascular unit as shown illustrates the key structures of the glymphatic system from the arterial side. [4] Cerebrospinal fluid (CSF) from the Virchow-Robin spaces continues its flow into the perivascular spaces around arterioles through to the capillaries. Astrocytic endfeet expressing aquaporin 4 (AQP4) channels surround the entire vasculature and form the boundary of the perivascular spaces. CSF flows out of AQP4 channels into the tissue parenchyma and is returned to perivenous spaces (not shown) toward the cervical lymphatic system and, eventually, into the venous circulation.

1.2 Choroid Plexus

The choroid plexus (ChP) is responsible for the production of CSF, which plays a crucial function in the CNS by delivering nutrients, washing away waste, and providing mechanical support for the brain. [5] In this sense, the ChP-CSF system is critical for the development and maintenance of the CNS, and, thus, appropriate ChP function is imperative to the formation and the integrity of the CNS. In fact, many

studies [6, 7] have shown that too little CSF severely impairs brain growth, as CSF pressure is essential for normal brain development. Excess CSF—from overproduction, flow obstruction, or limited resorption—for instance, can lead to hydrocephalus. Additionally, excessive subarachnoid CSF may be an early marker of autism spectrum disorder. [7]

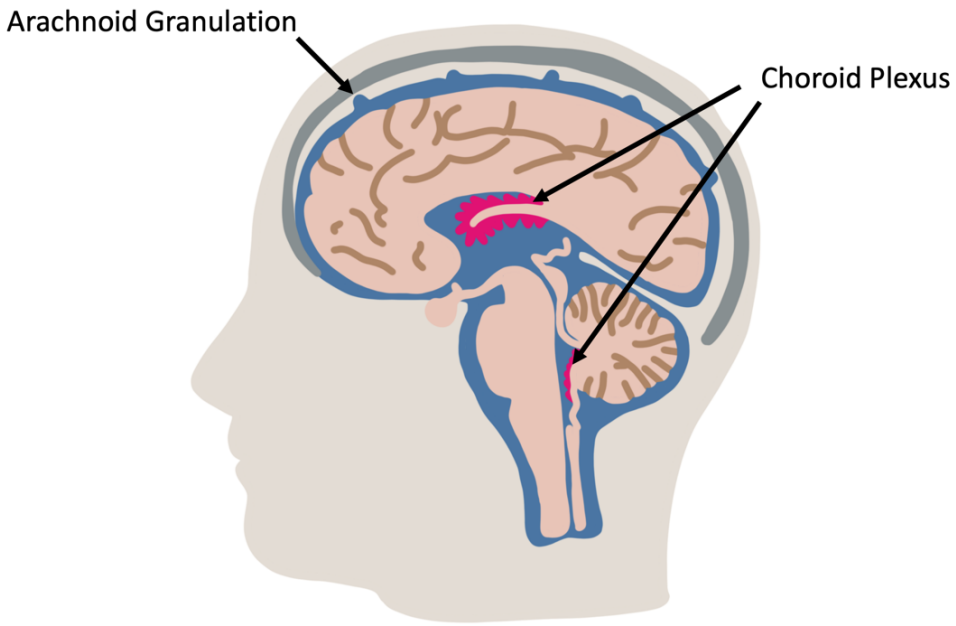

Figure 1.2: Choroid plexus is most prominent in the lateral and fourth ventricle, though it is present in all four ventricles, and is the primary producer of cerebrospinal fluid, which delivers nutrients, removes waste and provides mechanical support for the brain within the skull.

The ChP is a highly vascular tissue located in all four ventricles of the brain. It is observable in the posterior lateral ventricles (telencephalic ChP), third ventricle (diencephalic ChP), and the fourth ventricle (hindbrain ChP). Its structure reflects its secretory function and consists of a monolayer of cuboidal epithelial cells that surrounds a stromal core of capillaries and connective tissue. Tight junctions connect adjacent ChP epithelial cells, also called ependymal cells, to form the blood-CSF barrier (BCSFB), which prevents paracellular free passage of molecules from the systemic circulation into the CSF. Along with adherens junctions, tight junctions also ensure the apical-basal polarity of membrane proteins (e.g. transporters) that are critical for normal epithelial cell function.

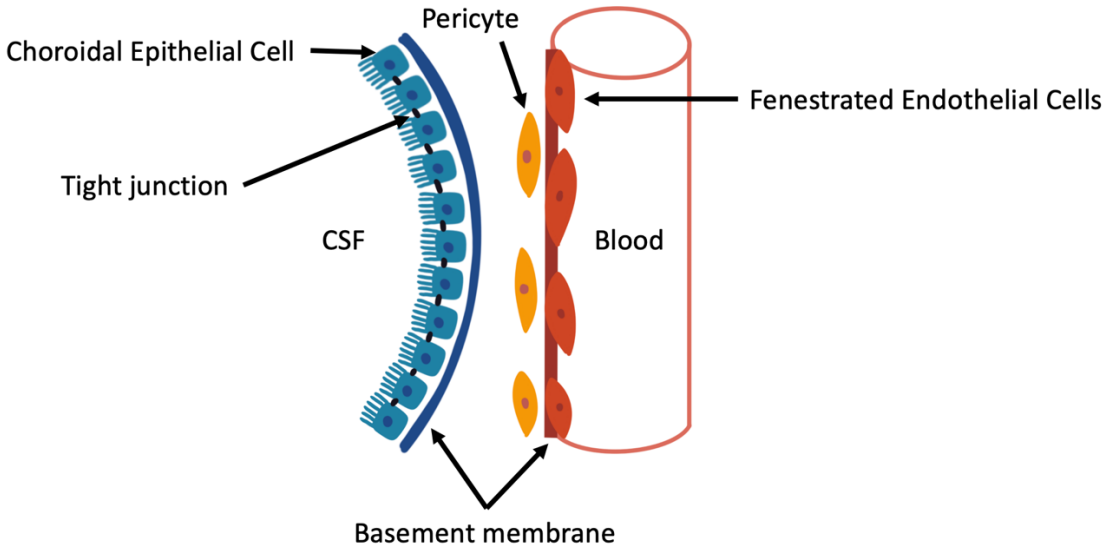

Figure 1.3: Blood-cerebrospinal fluid barrier (BCSFB) consists of vessels with a layer of fenestrated endothelial cells lying on a basement membrane. [8] Supportive pericyte cells are present in the interstitial space. Ciliated, cuboidal, choroidal epithelial cells—also called ependymal cells—are connected adjacently via tight junction proteins that prevent free paracellular flow.

The ChP receives blood supply from either the anterior or posterior circulation depending on its location. The anterior choroidal artery, which branches off the internal carotid or middle cerebral artery, supplies the telencephalic ChP. The posterior choroidal artery, which branches from the posterior cerebral artery, feeds the telencephalic ChP as well as the diencephalic ChP. The anterior and posterior inferior cerebellar arteries, which originate from the basilar and vertebral arteries, supply the hindbrain ChP. [9] Both sympathetic and parasympathetic innervation are thought to regulate blood flow and CSF secretion. Unlike the endothelium in the brain's parenchyma, capillaries of the ChP are fenestrated, and these endothelial fenestrae are connected by thin membranous diaphragms that are permeable to small molecules and water, thereby enabling rapid delivery of water through the blood to epithelial cells for CSF production. [10] Solutes can cross from the blood into the stromal space via diffusion across the endothelial fenestrae or by vesicular transport. As with capillaries in other CNS tissues, pericytes are

found in the ChP and wrap around the endothelial cells. Finally, the ChP harbors various immune cells and is a gateway for immune cell entry into the CNS.

From a histological perspective, the choroid plexus is made of numerous villi with each villus composed of a single layer of cuboidal or columnar epithelial cells that are continuous with the ependymal lining of the ventricles and rest on a basement membrane. [11] Underneath this layer lies connective tissue and a vascular network. The apical side of the epithelial cells has variable numbers of microvilli that differ in diameter and shape. On the lateral surface of the cells, desmosome and tight junctions play a major role in holding the cells together. Tight junctions are concentrated as small strands near the apical end of the cells, and it is proposed that they serve an important role in preventing the paracellular passage of molecules and, thus, contributing to the BCSFB.

The ChP has long been established as the principal—though not exclusive—producer of CSF. To this end, the ChP epithelial cells acquire their secretory, transport, and barrier functions shortly after differentiation. [10] Ion transporters at the basal and epical surfaces of ChP epithelial cells transport ions into the CSF, and water supplied by the blood is transported apically though aquaporins down an osmotic gradient. Transport across the ChP epithelium extends beyond ions to factors including proteins, nutrients, and metabolic precursors, and ChP epithelial cells also express and secrete their own proteins into the CSF.

In addition to distributing secreted signals throughout the ventricular system, the CSF has an important role in clearing the brain of toxins and waste. Recent work using two-photon imaging in mice through a cranial window led to the discovery of the glymphatic system whereby aquaporin-4 (AQP4) channels on astrocytic endfeet first facilitate the para-arterial CSF influx into the brain's parenchyma. [3] This convective flux of CSF and interstitial fluid (ISF), with the aid of arterial pulsatility, then flushes parenchymal waste via an intercellular trans-astrocytic path into the paravenous space for eventual clearance into the systemic circulation.

1.3 Blood-Brain Barrier

The blood-brain barrier (BBB) prevents neurotoxic substances, cells, and pathogens from entering the brain. [12] At the same time, it regulates transport of molecules into and out of the CNS to maintain a tightly controlled chemical composition of the neuronal milieu that is required for normal, homeostatic function. In diseased states, breakdown of the BBB and its associated dysfunction leads to leakages of harmful substances, including blood components and cells, into the CNS and aberrant transport and clearance of molecules. Together, these have been associated with cerebral blood flow (CBF) reductions and dysregulation, which contributes to neurological decline.

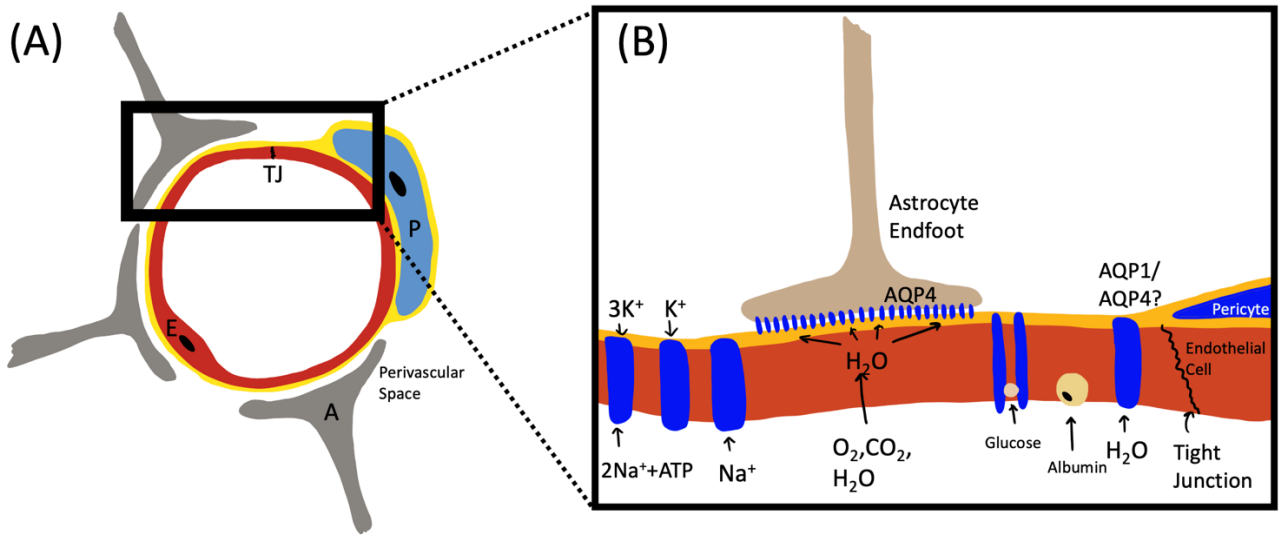

Figure 1.4: Blood-brain barrier is a cellular structure consisting of **(A)** a single endothelial cell at the capillary level (E) sealed by tight junction proteins (TJ). [13] Supportive pericyte cells (P) are present in perivascular space that is further coated by a layer of astrocytic endfeet (A). **(B)** A magnified examination of this barrier show that the passage of water and solutes is tightly controlled through the expression of various transmembrane proteins along this barrier.

The human brain is a highly vascularized organ given its high energy demand. Under normal physiological conditions, the brain receives 20% of the cardiac output and uses 20% of the body's oxygen and glucose. [14] Energy substrates are consumed by the brain as they are delivered because the brain lacks a reservoir to store fuel. In mammals, cerebral blood vessels supply CNS neuronal circuits with

blood in response to stimuli by increasing the rate of CBF and oxygen delivery through a mechanism termed neurovascular coupling, which is regulated primarily by the neurovascular unit.

The neurovascular unit comprises of vascular cells, including endothelial cells and mural cells, such as pericytes on brain capillaries, venules, and precapillary arterioles; vascular smooth muscle cells (SMC) on arterioles, small arteries, and veins; glial cells such as astrocytes, microglia, and oligodendrocytes; and neurons. [15] Molecular expression patterns in endothelial and mural cells vary at different levels of vascular tree creating arterio-capillary-venous heterogeneity, or "zonation". At the level of the penetrating arteries, endothelial cells form the inner layer of the vessel wall. The basement membrane separates endothelium from 1 to 3 layers of smooth muscle cells that are enveloped by pia (Figure 1.1). At the arteriolar level, smooth muscle cells were reduced to a single layer, whereas the endothelial layer displays a continuity with the endothelium of penetrating arteries and capillaries. At the capillary level, pericytes and endothelial cells share a basement membrane and exhibit different types of cellular connections. Both the arteriolar and capillary vessel wall is covered by astrocytic endfeet, and smooth muscle cells, pericytes, and astrocytes all have neuronal innervation. The BBB is present along the capillaries of the neurovascular unit where exchange occurs and is formed by a monolayer of tightly sealed endothelial cells extending along the vascular tree that prevents paracellular and transcellular passage.

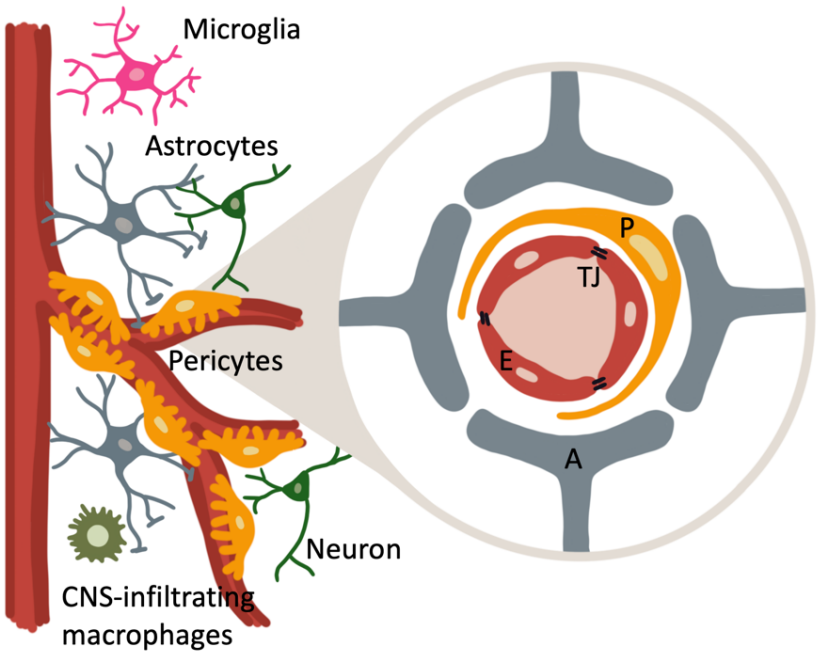

Figure 1.5: Neurovascular unit represents the coupling of the vascular and neural components of the central nervous system. [15] This interconnectedness allows for the requisite signaling that enables the brain to increase blood flow to regions where neurons are firing and, thus, have a higher demand for oxygen and metabolites.

1.4 Parceling the Human Brain

The human brain is the most complex of all biological systems, with the mature brain composed of more than 100 billion information processing cells called neurons. [16] The brain has three main parts: the cerebrum, cerebellum, and brainstem. This portion will focus primarily on the cerebrum, which is divided into right and left hemispheres and is the largest part of the brain. It is made up of folds and convolutions on its surface, with ridges found between the convolutions called gyri and the valleys between the gyri called sulci. If the sulci run deep, then they are called fissures. Both cerebral hemispheres have an outer layer of gray matter called cerebral cortex and inner subcortical white matter.

The cerebrum controls the motor and sensory information, conscious and unconscious behaviors, feelings, intelligence, and memory. [17] It is composed of four lobes. The frontal lobe is responsible for

motor function, language, and cognitive processes, such as executive function, attention, memory, affect, mood, personality, self-awareness, and social and moral reasoning. The parietal lobe is responsible for interpreting vision, hearing, motor, sensory, and memory functions. The temporal lobe contains the Wernicke area on the left side that is responsible for understanding spoken and written language. The temporal lobe is also an essential part of the social brain, as it processes sensory information to retain memories, language, and emotion. Furthermore, the temporal lobe also plays a significant role in hearing and spatial and visual perception. Finally, the occipital lobe contains the visual cortex and is responsible for interpreting visual information.

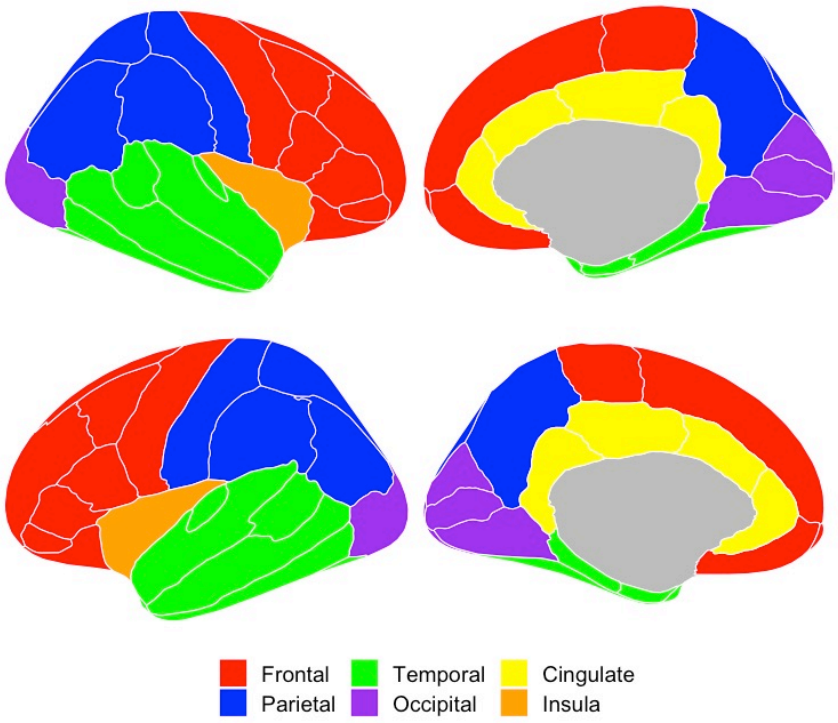

Figure 1.6: Cortical FreeSurfer parcellations are divided into four major lobes: frontal, parietal, temporal and occipital. Each lobe possesses unique functions that contribute to the basic sensory and motor abilities of the organism as well as upper-level thinking that is unique to humans.

In neuroimaging research, open-source software is often used to segment, or parcellate, the brain into different regions so that parameters, such as blood-brain barrier water exchange rate (Kw), arterial transit time (ATT), and cerebral blood flow (CBF) can be analyzed on a regional basis to best localize the

site of dysfunction (Figure 1.6). This way, we can determine just which part of the brain is abnormal to identify any patterns associated with a particular neurological or neuropsychiatric disorder. In Chapters 4, 5, and 6, FreeSurfer software [18] was used to parcellate the brain by first processing structural T1-weighted MRI scans to create 3D models of cortical surface and subcortical structures. The work in this dissertation only made use of the gray matter cortical structures. Initial steps in this process involves motion correction, intensity normalization, and removing non-brain tissue, or skull stripping. After that, the software generates 3D surface models of the brain, including the boundary between gray and white matter as well as the outer cortical surface. This is achieved using a hybrid approach that incorporates both deformable surface models and robust programming algorithms. In the segmentation, or parcellation phase (Figure 1.6), labels are applied by aligning the subject's brain surface with a pre-defined probabilistic atlas, such as the Desikan-Kiliany, containing information about the typical folding patterns of the brain. In our study, the Desikan-Kiliana atlas was applied to divide the cerebral cortex into 34 regions per hemisphere. Overall, this process enables us to extract underlying Kw parameters within each of the regions and forms the basis for our group comparison and analysis.

1.5 Pathophysiology

The BBB plays a critical role in keeping potentially neurotoxic substances out of the brain. With age, however, a natural decline of BBB function has been reported in both animal and human studies, and this has been hypothesized to contribute to cognitive decline and neurodegeneration. [19] Furthermore, recent studies are beginning to show that being female has a protective effect against BBB deterioration possibly because of either lifestyle differences or the difference in hormonal profile between men and women. [20, 21]

There exist two biological mechanisms that has been proposed to be the cause of BBB functional breakdown that is relevant to arterial spin labeling (ASL) BBB neuroimaging. The first is reduced and nonpolarized expression of AQP4 channels with "nonpolarized" being defined as the expression of the channel protein away from the astrocytic foot processes. Overall, this results in lower water exchange rate

(Kw) with disease and natural aging. Since water exchange from the blood across the endothelial cells and astrocytic foot processes is an integral step of the glymphatic system, a reduction in and nonpolarized expression of AQP4 channels would lead to the inability of the waste clearance system to wash away cellular waste. This has been proposed to be one of the causal mechanism to the development of Alzheimer's disease, which is characterized by abnormal protein aggregation. [22]

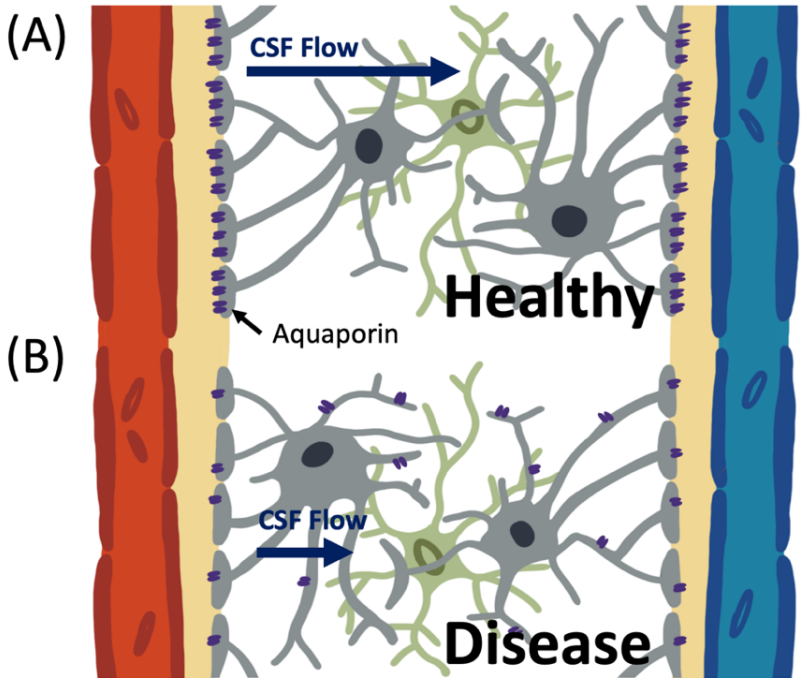

Figure 1.7: Glymphatic system in **(A)** healthy states has AQP4 water channels expressed in abundance along the astrocytic endfeet of the blood-brain barrier, and this allows for free flow of CSF across the brain parenchymal space to wash away waste. [22] In the **(B)** diseased state, aquaporin expression has been proposed to decrease and become nonpolarized, meaning that expression occurs diffusely along the astrocyte body and arms. This results in a decrease in CSF flow which further leads to the inability of the glymphatic system to clear away waste in the brain parenchymal space.

The second mechanism of BBB deterioration is tight junction breakdown, and this process has been shown to occur in both mice and humans. Interestingly, this mechanism would result in an increase in water transfer rate across the BBB. Additionally, as results of BBB integrity loss, potentially neurotoxic entities present in the blood would be able to enter the brain parenchyma. Overall, this

biological mechanism supports an inflammatory theory of BBB breakdown with normal aging and disease—though it may be important to note that inflammation also affects AQP4 expression and polarization. [23] For instance, it has been hypothesized that early maternal immune activation (MIA) is one of underlying causal mechanisms of the psychotic disorder schizophrenia. MIA proposes that immune sensitization in early gestational periods of fetus development will prime the fetal brain to be more easily inflamed after birth. With chronic inflammation, tight junction expression decreases in response to pro-inflammatory cytokines signaling and allows bloodborne immune cells to enter the brain parenchyma.

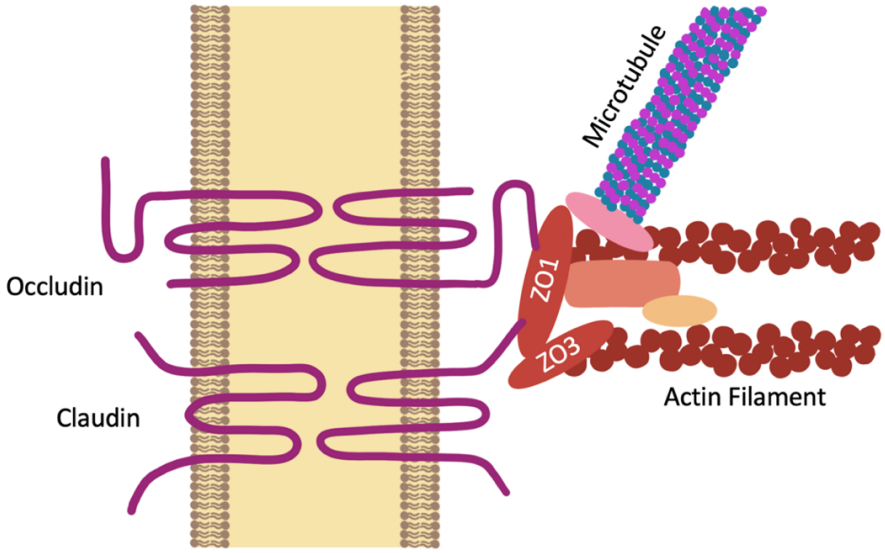

Figure 1.8: Tight junction consists of a transmembrane portion comprised of the occludin and claudin proteins along with an intracellular portion that tethers it to the intracellular cytoskeleton that consists of different isoforms of zonula occludin (ZO) proteins. [24]

1.6 Summary

To conclude, the recent discovery of the glymphatic system has ignited interest in the scientific community for the application of MRI as a noninvasive way to assess the functional status of the brain's waste clearance system and associated structures, such as the ChP and the BBB. The overall effort is toward the development of novel imaging biomarkers that can serve as a diagnostic and prognostic indicators of different neurological diseases. The BBB, a cellular structure interdependent with the

glymphatic system, is the focus for many advanced imaging modalities that will be discussed in the coming chapters. It is hypothesized that assessment of Kw as a proxy measure for BBB integrity and function in different regions of the brain could serve as a biological indicator of the tissue's health within that region.

Chapter 2 Current Methods to Image the Brain

2.1 Dynamic Contrast Enhanced MRI

Loss of BBB integrity can result in the flux of blood borne low-molecular weight MRI contrast agent into the tissue parenchyma. [25] Accumulation of contrast material in the extravascular extracellular space (EES) leads to increased longitudinal relaxation rate and, thus, increased signal in T1-weighted images. Dynamic contrast enhanced (DCE) MRI takes advantage of T1 shortening to evaluate and detect regions of BBB disruption. DCE-MRI typically involves intravenous injection of contrast agent followed by repeated acquisition of T1-weighted images, thereby capturing measurements of signal enhancement as a function of time (Figure 2.1). The resulting kinetic curve can be used to further extract quantitative or semi-quantitative information regarding BBB integrity.

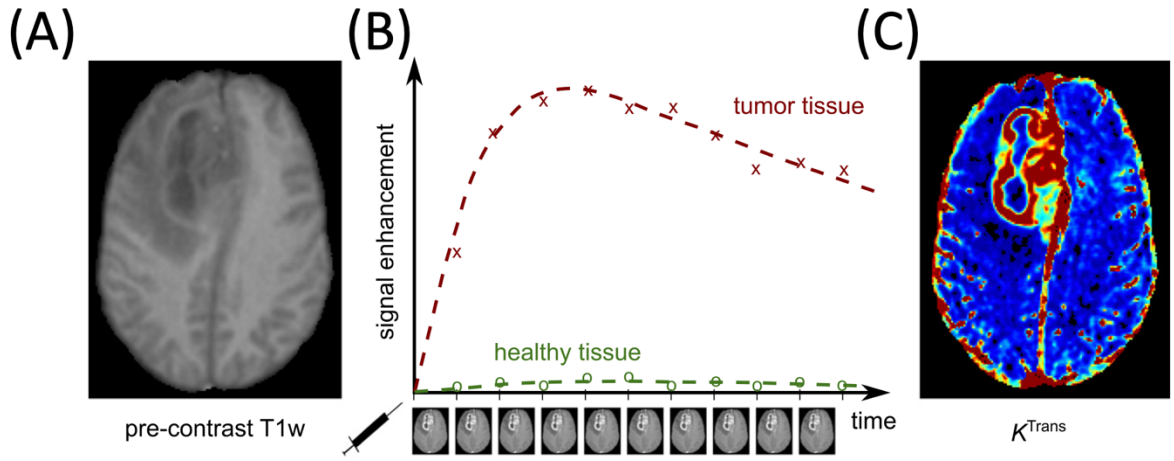

Figure 2.1: Dynamic contrast enhanced MRI kinetic curve in a patient with glioma. [25] Repeated acquisition of T1-weighted images after contrast agent injection allows the calculation of signal enhancement as a function of time **(B)** when compared to the pre-contrast signal intensity **(A)**. These curves can be used to calculate maps of quantitative pharmacokinetic parameters like K_{trans} **(C)**.

Gadolinium chelates represent the major contrast agents used for MRI. Though, historically, the use of these agents have been considered safe, recent findings has uncovered an association between gadolinium-based contrast agents (GBCAs) administration and the development of nephrogenic systemic

fibrosis (NSF) in patients with severe renal impairment. [26] Additionally, there is evidence regarding the accumulation of gadolinium in various tissues of patients who do not have renal impairment, including bone, brain, and kidneys. Together, these toxicity concerns represent a major limitation of GBCAs and restricts their use in longitudinal studies involving repeat scans as well as in the young healthy population.

Many approaches have been developed to analyze the T1 enhanced signal curve of DCE-MRI. Model-free approaches involve looking at the signal curve to glean semi-quantitative measures of BBB disruption, such as area under the curve (AUC) and the time to maximum enhancement. These parameters are easy to calculate but can be challenging to interpret. On the other hand, model-based approaches provide a link between the tissue signal enhancement and physiologically relevant parameters such as microvascular permeability, blood flow, blood volume fraction and interstitial volume fraction.

Two popular model-based approaches include the Toft model [27] and the Patlak model [28], both of which are based on a general tissue model that estimates contrast agent exchange between blood plasma and EES (Figure 2.2). The target parameters of pharmacokinetic modeling in DCE-MRI are the fractional plasma volume v_p, the fractional interstitial volume v_e, the plasma flow F_p, and the permeability-surface area product PS, which measures the rate at which contrast agent particles leak out of the plasma and into the EES per unit tissue volume and plasma concentration. Additionally, the volume transfer constant, K_{trans}, is another important DCE-MRI parameter that represents the rate at which contrast agent is delivered to the EES per volume of tissue and contrast agent concentration in the arterial blood plasma.

While PS and K_{trans} are sometimes used interchangeably, PS represents the clearance for contrast agent leaking from the capillary plasma into the EES. In other words, PS represents the flux of contrast agent across the BBB normalized to the tissue plasma concentration and tissue volume. In contrast, K_{trans} is the contrast clearance normalized to the arterial plasma concentration and, thus, is a function of both the plasma flow F_p supplying the capillaries in addition to PS with the exact relationship dependent on the model used. Thus, K_{trans} is inevitably equal to the product of F_p and the extraction fraction E according to

the Renkin-Crone equation, which models E of a solute from blood in a capillary showing how it depends on the PS and F. [13]

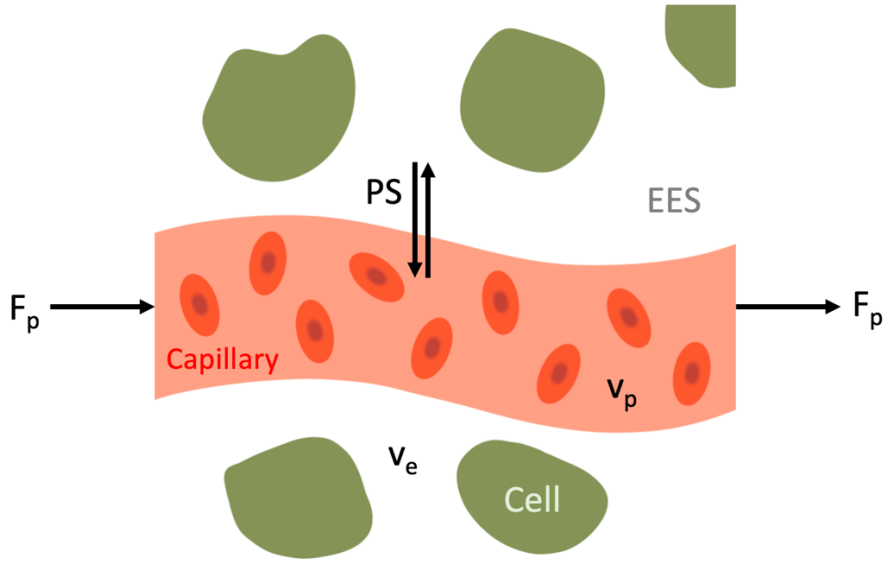

Figure 2.2: Schematic illustration of the general tissue model for DCE MRI and target parameters. The exchange between the extravascular extracellular space (EES, volume fraction v_e) and capillary blood plasma (volume fraction v_p) is determined by plasma flow F_p and the permeability-surface area product PS.

2.2 Positron Emission Tomography

2.2.1 Perfusion

The current reference standard for cerebral blood flow measurements is positron emission tomography (PET) using injection of the ^{15}O-water radiotracer. [29] Despite the use of ^{15}O-water radiotracer in both healthy and diseased patients in research studies, this method has not been adopted clinical practice due to the need for an onsite cyclotron, invasive nature of the arterial blood sampling, and procedural complexity. In a typical experiment, ^{15}O-water is injected into the patient and modeled as a freely diffusible, but not metabolized, tracer that enters the cerebral tissue. Integration of the PET signal

reflects the perfusion status of the brain as equilibrium is achieved in a few minutes. Additionally, because of the short half-life of oxygen-15 (~2 minutes), an onsite cyclotron must be present to perform the experiment. On top of that, patients must undergo invasive arterial cannulation to determine an arterial input function (AIF). Together, these complexities represent major hinderances against the adoption of ^{15}O-water PET perfusion imaging in the clinics.

PET imaging not only allows for the visualization of injected radiotracers, but it also could apply quantitative models to the signal to quantify biomedical functions such as perfusion. [30] Compartmental modeling is the basic way to analyze dynamic PET data, which represents the tracer concentration at a certain point in time. To interpret the observed PET data over time, we assume there are physiologically separate pools of tracer substances called "compartments". Kinetic models for dynamic PET signals vary in complexity (i.e., number of compartments) depending on the tracer and underlying physiological assumptions. The simplest form and the one used in this work is the one-tissue compartment model (Figure 2.3), which is appropriate to estimate blood flow, or perfusion, measurements in ^{15}O-water imaging with PET.

In the one-tissue compartment model, the first compartment (C_p) is for the input function (i.e. plasma or blood curve) that is traditionally measured through arterial cannulation. The second compartment (C_T) is for the radiotracer label in tissue. Together these two compartments are connected by two rate constants, K_1 and k_2. The ordinary differential equation for simulation of the change over time in tissue compartment, C_T is given by:

$$\frac{dC_T(t)}{dt} = K_1 C_p(t) - k_2 C_T(t) \qquad \text{[E2.1]}$$

The rate constant K_1 represents the unidirectional transport of the tracer from plasma or blood compartment to the first tissue compartment. Through the Fick principle and the Renkin-Crone model, K_1 is dependent on perfusion f and the product of capillary permeability and capillary surface area PS.

$$K_1 = f(1 - e^{-PS/f}) \qquad \text{[E2.2]}$$

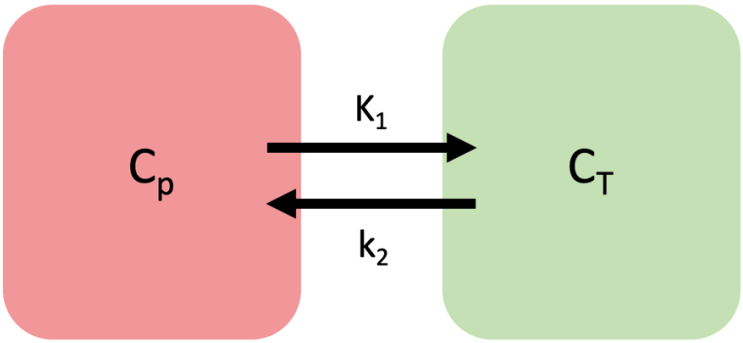

Figure 2.3: Single tissue compartment model. This model has only one compartment in tissue and exchange radiotracer between plasma compartment (C_p) and tissue compartment (C_T) by two rate constants K_1 and k_2. [30]

2.2.2 Blood-Brain Barrier Imaging with PET

BBB imaging with positron emission tomography (PET) can be done in both quantitative (i.e. kinetic modeling) [31] and qualitative ways (i.e. visual analysis of tracer uptake) and has been performed in both animal and human research. However, because of the challenges associated with PET, such as the short half-life of radiotracers, need for onsite cyclotron, and procedural complexity, this method is typically found only at large research hospitals and reserved for research studies. Additionally, the risk for exposure to ionizing radiation makes BBB imaging with PET not preferred in repeat studies in the young healthy population or in longitudinal studies. Together, these attributes make PET imaging unfavored for studying the psychiatric population as patients tend to be younger and study design is most robust when longitudinal follow up is instigated.

PET is a molecular imaging method that relies on the labeling of radioactive isotopes onto endogenous molecules, which act as imaging tracers. Depending on the radiotracer, different mechanism of BBB change will be assessed as different radiolabeled molecules will interact with the endogenous biology in its own unique way. These changes may include 1) increased BBB permeability, 2) impaired glucose transport, 3) impaired efflux transport, and 4) dysregulated fluid exchange. [15] Additionally, the tissue extraction fraction, which may be different for each radiotracer, can influence the overall

permeability and exchange metric being calculated. Thus, given the wide range of radiotracers available, PET can offer a molecularly specific assessment of BBB dysfunction. Overall, the specific attributes of PET imaging make this modality more suitable to be used in preclinical animal models and perhaps in the study of pharmacological effects.

2.3 Arterial Spin Labeling MRI

2.3.1 Introduction

Even though arterial spin labeling (ASL) was invented [32] around the same time as the blood oxygen level dependent (BOLD) effect, it took decades for ASL to be more widely adopted by the neuroimaging community. This advancement was made possible through a combination of technological developments including the advent of parallel imaging, the development of pseudo-continuous labeling, and background suppression schemes that, together, ensure that ASL scans can be acquired with enough speed and quality to be useful for researchers and clinicians alike. In 2014, the MR community came together to make a set of recommendations for a "standard" ASL implementation. [33] Even though these parameters may not be the ideal ones under every physiological scenario, this standardization of ASL protocol has helped different vendors implement ASL pulse sequences that can be distributed as a packaged product to the research community. Together, these efforts help to establish gold standards for calibration of validation of ASL images as a quantitative biomarker. [34]

In ASL, the tracer used is the water molecules in the blood itself, making this method nonionizing, thus, appropriate for use in young, healthy research participants. To label the tracer, the magnetization of water molecules in the blood is inverted with a train of RF pulses at artery that feeds the organ of interest. With brain imaging, the labeling plane is typically located around the bifurcation of the internal and external carotid artery of the neck. As this "labeled" blood travels to the brain tissue, it reduces the available magnetization in the tissue and, consequently, the images collected downstream of the labeling location appear slightly darker. If we subtract the labeled images from a set of control images (i.e. without label), we get a subtraction image from which we can then estimate the amount of blood that

has entered the organ since the beginning of the labeling period. Furthermore, if we apply a two-compartment mathematical model [35-37] to the ASL signal in each voxel that separates the signal into a theoretical tissue and blood component, we can then model the water exchange rate (Kw) between the two compartments as a proxy for BBB integrity. ASL sequences that rely on different mechanisms to separate the ASL signal into a tissue and blood compartment constitutes the primary focus of this thesis.

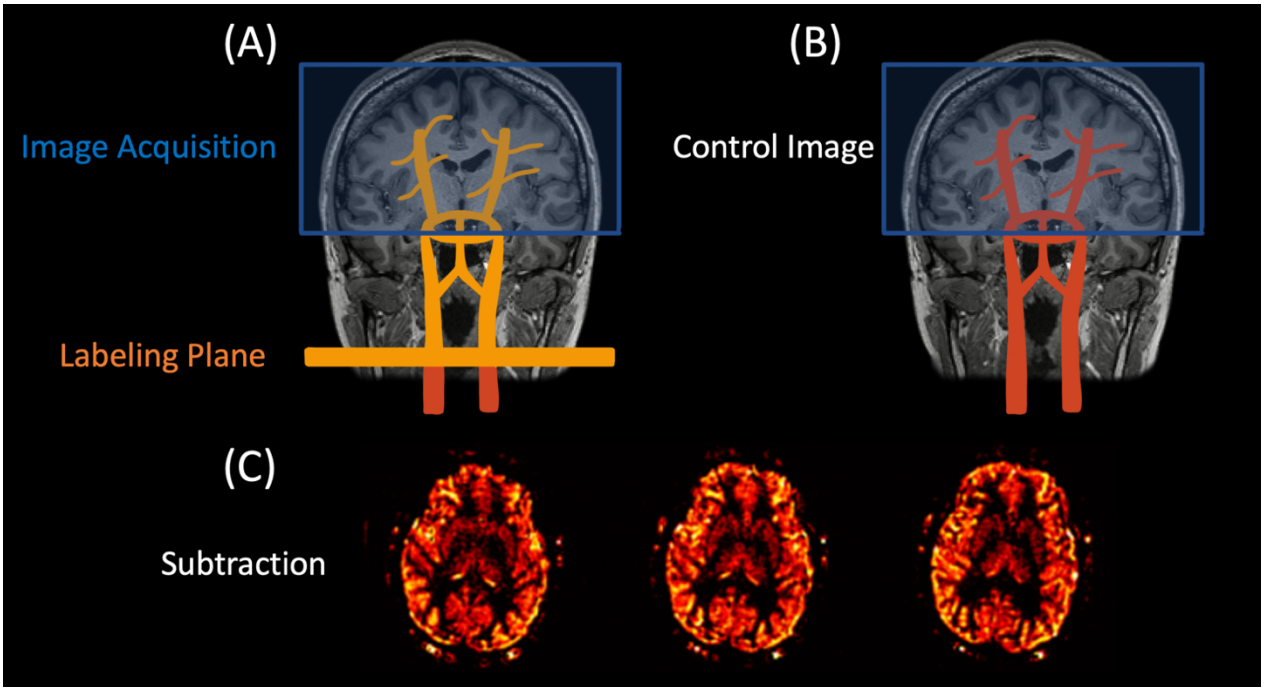

Figure 2.4: Pseudo-continuous ASL (PCASL) experiment. Arterial water is inverted as it crosses a labeling plane through the neck prior to acquiring the **(A)** "labeled" image. A second **(B)** "control" image is acquired without the label. The subtraction of control minus label yields a **(C)** perfusion weighted image. [34]

2.3.2 Perfusion

Blood perfusion serves a critical physiological role by delivering oxygen and nutrients to the tissue and is a metric that is intricately tied to tissue function in the sense that disorders of abnormal perfusion are major sources of medical morbidity and mortality. Since the first study demonstrating the feasibility of arterial spin labeling to measure perfusion was published in the early 90s [32], an abundance of basic science and clinical applications of ASL MRI have been introduced with most of these studies

focusing on the brain. [38] Since that time, numerous technical improvements have been made in the methodology which have made the acquisition of whole-brain ASL data possible in both the research and clinical settings. The brain has been studied most because of this organ's high blood supply demand, its spatially straightforward blood supply, the lack of major motion issues, and the normally tight coupling between regional cerebral blood flow and neural activity.

Clinical applications of ASL have been made possible through the distribution of commercial ASL sequences for most major clinical MRI platforms. Applications have largely been applied to disorders associated with the cerebral vascular system such as cerebrovascular disease, acute stroke, sickle cell disease, arterial occlusive disease, and brain malignancies. [38] Additionally, in most organs including the brain, changes in perfusion are coupled with changes in metabolism, and this relationship provides the physiological basis of functional MRI (fMRI) studies that has clinical relevance. For instance, several studies have supported the use of ASL MRI to detecting patterns of regional hypoperfusion, which suggest a diagnosis of Alzheimer's dementia or frontotemporal dementia. [39-41] This noninvasive method could serve as a complement to existing molecular imaging studies, which are costly and not always available.

ASL is particularly suitable for basic science research because this method is both quantitative and is one of the few MRI contrast mechanisms for which the biological basis is well understood. Its application has been broad in the field of neuroscience and has been increasingly included in multimodal neuroimaging protocols as well. In developmental biology, for instance, ASL is currently being used as a biomarker for functional brain development in both the healthy and abnormal populations. This method is appropriate in the pediatric population because of its noninvasive nature. Furthermore, blood flow is typically higher in children (except newborns) compared to adults thereby giving this method an SNR boost in this population. [38] Within the cognitive neuroscience fields, ASL MRI can be used to monitor task-correlated cerebral blood flow (CBF) changes in a manner much like BOLD fMRI. Though task-correlated percentage signal changes in ASL are weaker than BOLD changes, there is evidence to suggest that ASL changes are better localized both spatially and temporally than BOLD changes. [38]

To conclude, ASL is a unique MRI contrast mechanism because it directly detects and quantifies the physiological process of CBF, which is a versatile biomarker of both normal and pathological brain function. Thus, the inclusion of ASL in large cross-sectional and longitudinal databases will likely contribute to new insights into the neural basis for a range of behaviors and disorders.

2.3.3 Two-Compartment Model

The two-compartment model for arterial spin labeling was first proposed by Parkes and Tofts [35] and directly estimates permeability surface area (PS) by fitting data acquired at multiple PLDs into a modified Bloch equation. It is more accurate in assessing perfusion than the one-compartment (or Kety) model (Figure 2.5A), which assumes instantaneous mixture of labeled blood with the tissue upon arrival at a given voxel. The Kety model has been shown to overestimate perfusion at low physiological flow rates and underestimate it at high physiological flow rates. [42]

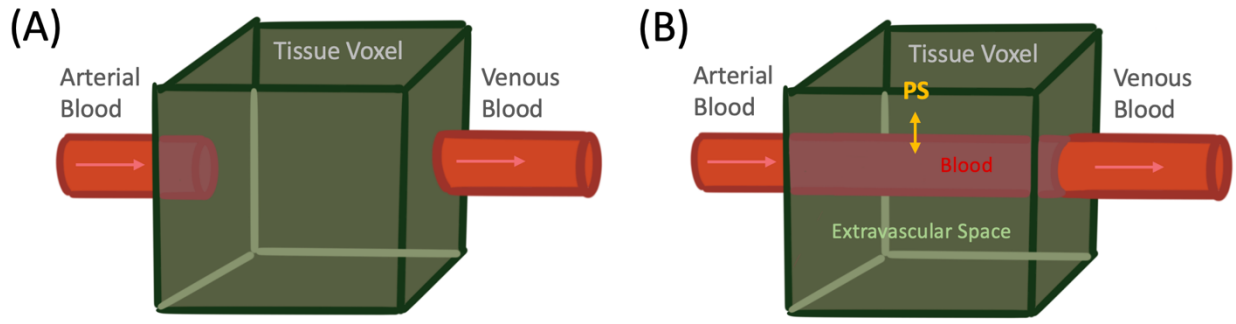

Figure 2.5: Compartmental models for arterial spin labeling MRI. **(A)** The original one-compartment, or Kety model, that assumes instantaneous mixture of labeled water molecules with the tissue upon arrival at a brain voxel. **(B)** The modified two-compartment model.

While the implementation of the two-compartment model was initially meant to be an advancement to improve the accuracy of the assessed perfusion, the integration of the new *PS* term—meant to represent the permeability of the hypothetical endothelium separating the blood and tissue compartments—led to interest in the assessment of the water exchange rate (Kw) between the two

compartments as a proxy measure for BBB functional status and integrity. Since the 2002 publication by Parkes et al. [35], a number of groups have been implementing different strategies to separate the ASL blood and tissue signal in order to model this water exchange rate term (Figure 2.6).

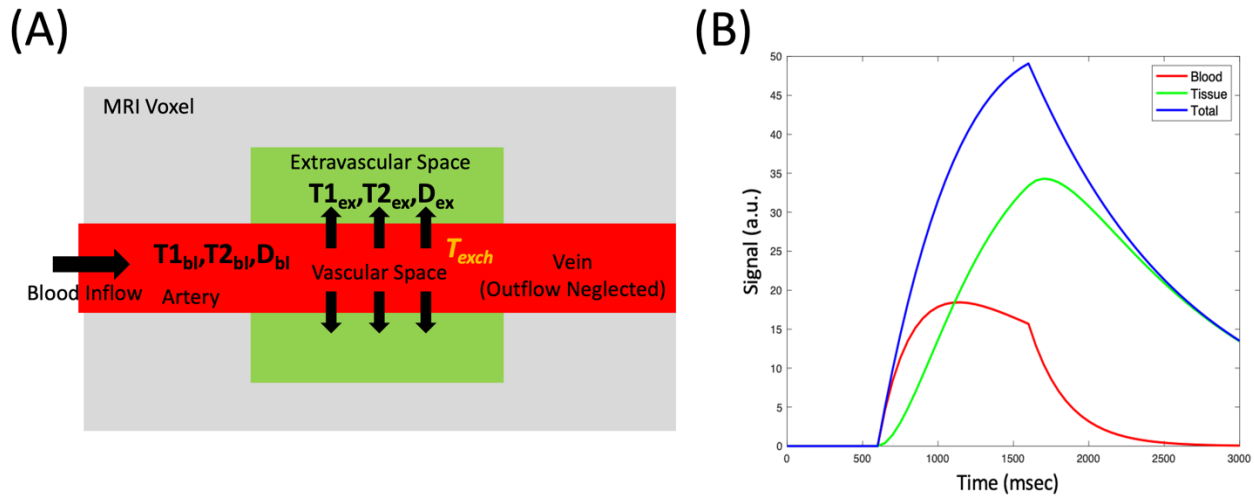

Figure 2.6: Separation of ASL signal in the two-compartment model. **(A)** Diffusion-weighted (DW) ASL and multi-echo time (ME) ASL rely on the assumption of significant differences in pseudo diffusivity (D) and transverse relaxation time (T2) to mathematically split the overall ASL signal into an intravascular and extravascular component. **(B)** The ASL kinetic curve with the total signal (blue) split into an intravascular (red) and extravascular (green) component.

Diffusion-weighted (DW) ASL utilizes the two-compartment model to separate the capillary and tissue components of the labeled blood water signal in the voxel, thereby allowing the rate of water exchange between the two compartments to be estimated. Since water molecule in the capillary space has a faster diffusion rate than that of tissue (~100 times), applying an optimized diffusion gradient before image acquisition will crush the signal from the blood while preserving the tissue signal. By applying different diffusion weighting to generate different ratios between the two components, the underlying water exchange rate can be estimated by fitting the signal to a set of mathematical equations. [43]

Multi-echo time (ME) ASL, on the other hand, separates the intravascular and extravascular signals by relying on the significant T2 relaxation time difference between tissue and blood water. Wells

et al. [44] first noticed that blood water molecules that have entered the tissue have increased T2 when the authors observed that the apparent T2 increased with PLD, indicating that the labeled water has entered the extravascular space. The same study reported the use of ME ASL for estimating blood-tissue exchange time by fitting the multi-echo data to the bi-exponential curves [45, 46] or a model considering both T1 and T2. [37]

2.3.4 Diffusion-Weighted Arterial Spin Labeling

The theory behind DW ASL is based on a two-compartment model developed by St. Lawrence et al. [36] and is called the two-stage single pass approximation (SPA) model for estimating water exchange rate. “Two-stage” refers to two separate scans with different PLDs to estimate 1) the ATT and 2) the Kw, and the SPA assumes that there is no venous outflow (i.e. all the labeled water molecules exchanges into the tissue space) and that the exchange is unidirectional. These assumptions are reasonable because, biologically, the capillary space is significantly smaller than the interstitial tissue space, and the image acquisition time is much faster than the vascular transit time.

In the first stage of DW ASL approach, the flow encoding arterial spin tagging (FEAST) sequence developed by Wang et al. [47] measures the ATT (Figure 2.7). Because of the relatively short PLD used, this method assumes that labeled spins remain primarily in the vasculature and microvasculature rather than exchanging completely with tissue water. By setting the fractional ASL signal with and without bipolar gradient to a set of theoretical equations (not shown), ATT can be deduced as it becomes the only unknown variable.

Once ATT is measured, the second stage of the DW ASL sequence utilizes a much longer PLD to allow the labeled water molecules to reach the tissue compartment. Additionally, a bipolar gradient whose strength is dictated by a b-factor is also applied to suppress the spins moving through the microvasculature. Kw is subsequently estimated analogously to the FEAST protocol where the ASL signal fractional signal with and without bipolar gradient is set to a set of theoretical two-compartment model equations where Kw is the only unknown.

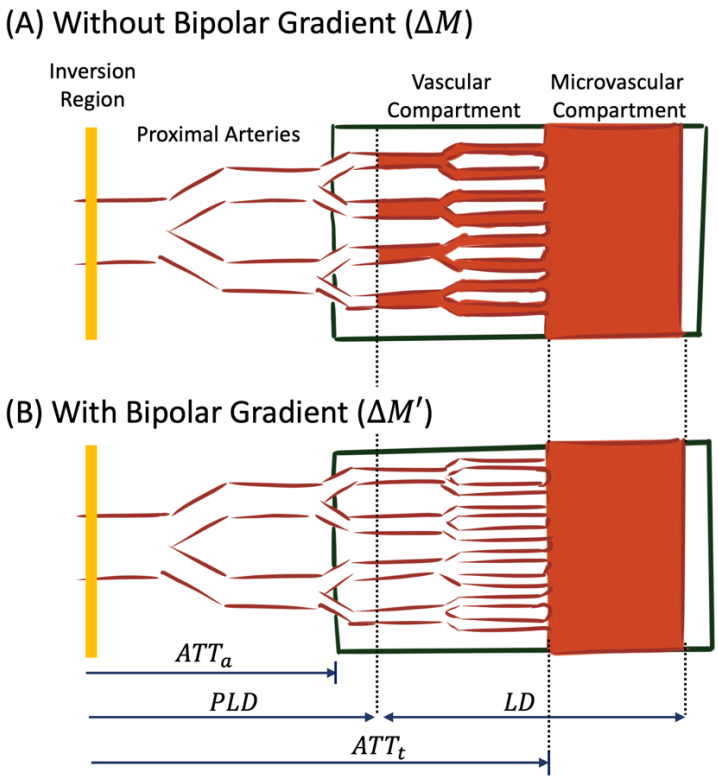

Figure 2.7: Flow encoding arterial spin tagging (FEAST) to measure arterial transit time (ATT). FEAST is a technique to measure ATT, which is derived from the ratio between ASL signal with ($\Delta M'$) and without (ΔM) a diffusion weighted bipolar gradient applied. The tissue transit time (ATT_t) can be deduced from the fractional ASL signal with and without bipolar gradient ($\frac{\Delta M'}{\Delta M}$) given the known imaging parameter of PLD or labeling duration (LD).

The SPA model is characterized by the following equation:

$$\Delta M(t) = CBF \int_0^t q(u)\Delta M_a(t-u)du \quad \text{[E2.3]}$$

Where ΔM is the total ASL signal, $\Delta M_a(t)$ is the difference in arterial blood magnetization between control and label, and $q(t)$ is the impulse residue function, which is further divided into a capillary, $q_c(t)$, and brain tissue, $q_b(t)$, component each defined as:

$$q_c(t) = e^{-\alpha t} \quad \text{[E2.4]}$$

$$q_b(t) = \beta[e^{-R_{1b}t} - e^{-\alpha t}] \quad \text{[E2.5]}$$

For pseudo-continuous ASL (PCASL), $\Delta M_a(t)$ is defined as:

$$\Delta M_a(t) = \begin{cases} 0 & 0 < t < ATT \\ -\frac{2\mathcal{E}M_0}{\lambda} e^{-R_{1a}t} & ATT \leq t \leq \tau + ATT \\ 0 & \tau + ATT < t \end{cases} \quad \text{[E2.6]}$$

Where ε is the labeling efficiency, M_0 is the tissue equilibrium magnetization, λ is the partition coefficient of water in the brain, and τ is the labeling duration.

Under these conditions, the ASL contributions and solutions to the equation E2.3 for the capillary, $\Delta M_c(t)$, and tissue, $\Delta M_b(t)$, components are given by the following:

$$\Delta M_c(t) = -\frac{2CBF\varepsilon M_0}{\lambda\alpha} e^{-(R_{1a}-\alpha)ATT}\left(e^{-\alpha(t-\tau)} - e^{-\alpha t}\right) \quad \text{[E2.7]}$$

$$\Delta M_b(t) = -\frac{2CBF\varepsilon M_0\beta}{\lambda}\left[\frac{e^{-(R_{1a}-R_{1b})ATT}}{R_{1b}}\left(e^{-R_{1b}(1-\tau)} - e^{-R_{1b}t}\right) - \frac{e^{-(R_{1a}-\alpha)ATT}}{\alpha}\left(e^{-\alpha(t-\tau)} - e^{-\alpha t}\right)\right] \quad \text{[E2.8]}$$

To estimate Kw, *in vivo* ASL signals with ($\Delta M(b_{DW})$) and without ($\Delta M(b_0)$) diffusion gradients are set to the fractional form of the theoretical equations. These are also referred to as the blood and tissue signal fractions or $A_1(t)$ and $A_2(t)$, respectively.

$$A_1(t) = \frac{\Delta M_c(t)}{\Delta M_c(t)+\Delta M_b(t)} = 1 - \frac{\Delta M(b_{DW})}{\Delta M(b_0)} \quad \text{[E2.9]}$$

$$A_2(t) = \frac{\Delta M_b(t)}{\Delta M_c(t)+\Delta M_b(t)} = \frac{\Delta M(b_{DW})}{\Delta M(b_0)} \quad \text{[E2.10]}$$

2.3.5 Multi-Echo Arterial Spin Labeling

The theoretical two-compartment model equations for ME ASL is derived by extending the General Kinetic Model (GKM) [48] for T2 decay. The GKM is a set of equations that models the magnetization of the tagged water molecules in the brain. The water exchange parameter in these sets of equations is the time of exchange (Texch), which is formally defined as the time it takes for a water molecule to move from the intravascular compartment to the extravascular compartment.

Two-Compartment Model and T1 Relaxation

In the two-compartment model, the overall signal, $S(t)$, can originate from either the blood, $S_{bl}(t)$, or tissue space, $S_{ex}(t)$, giving way to the following relationship:

$$S(t) = S_{bl}(t) + S_{ex}(t) \qquad \text{[E2.11]}$$

In the GKM, the components are calculated forming the convolution over the input function $c(t)$ with a residue function, generally modeling signal loss:

$$S_{bl}(t) = 2 \cdot M_{a,0} \cdot f \int_0^t c(t') \cdot r_{exch}(t - t') \cdot m_{bl}(t - t') \cdot r_{bl,out}(t - t')dt' \qquad \text{[E2.12]}$$

$$S_{ex}(t) = 2 \cdot M_{a,0} \cdot f \int_0^t c(t') \cdot (1 - r_{exch}(t - t')) \cdot m_{ex}(t - t') \cdot r_{ex,out}(t - t')dt' \qquad \text{[E2.13]}$$

Where $r_{exch}(t)$ is the exchange function, $m(t)$ is the magnetization decay function, and $r_{out}(t) \equiv 1$ is the negligible outflow function.

The input function, $c(t)$, is defined as:

$$c(t) = \begin{cases} 0 & t < \tau \\ \alpha \cdot e^{-tR1_{bl}} & \tau < t < \tau_2 \\ 0 & t > \tau_2 \end{cases} \qquad \text{[E2.14]}$$

Where τ is the arterial transit time (ATT) and $\tau_2 = \tau + Labeling\ Duration$.

The exchange function, $r_{exch}(t)$, is defined as the following:

$$r_{exch}(t) = e^{-t/T_{exch}} \qquad \text{[E2.15]}$$

The magnetization decay function, $m(t)$, is defined as:

$$m_{bl}(t) = e^{-tR1_{bl}} \qquad \text{[E2.16]}$$

$$m_{ex}(t) = e^{-tR1_{ex}} \qquad \text{[E2.17]}$$

And with the assumption of a negligible outflow function:

$$r_{bl,out}(t) \equiv r_{ex,out}(t) \equiv 1 \qquad \text{[E2.18]}$$

Two-Compartment Model and T2 Relaxation

Once the tagged water bolus reaches the brain after an inflow time (TI), a 90° RF pulse is applied that tips the magnetization into the transverse plane resulting in the signal becoming a function of both T1 and T2. From here, the total ASL signal, $S(ti, te)$, and its intravascular, $S_{bl}(ti, te)$, and extravascular, $S_{ex}(ti, te)$, components can then be modeled as three-dimensional planes (Figure 2.8) that satisfy the follow relationship:

$$S(ti, te) = S_{bl}(ti, te) + S_{ex}(ti, te) \qquad \text{[E2.19]}$$

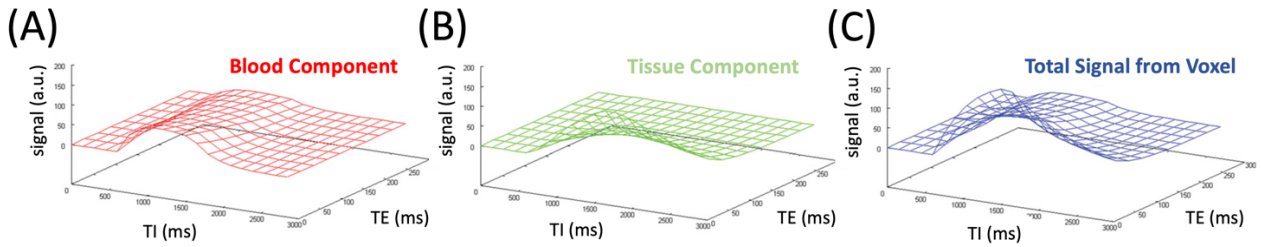

Figure 2.8: Multi-Echo Time (ME) ASL two-compartment model and T2 relaxation. [37] (A) Blood component, (B) Tissue component, and (C) the total ASL signal as a function of inversion time (TI) and echo time (TE).

Once the signal is tipped into the transverse place, a subsequent train of 180° refocusing pulses can be played to generate echoes. At this point, the GKM can be modified to include transverse relaxation and inflow from TI until TI + TE as follows:

$$S2_{bl,TI}(te) = 2 * M_{a,0} * f * \int_0^{te} c2_{TI}(t') * r_{exch}(te - t') * m2_{bl}(te - t') * r_{bl,out}(t - t')dt' \quad \text{[E2.20]}$$

$$S2_{ex,TI}(te) = 2 * M_{a,0} * f * \int_0^{te} c2_{TI}(t') * \left(1 - r_{exch}(te - t')\right) * m2_{ex}(te - t') * r_{ex,out}(t - t')dt' + S_{ex,TI} * m2_{ex}(te) \quad \text{[E2.21]}$$

Here, the input function, $C2_{TI}(t)$, now becomes

$$C2_{TI}(t) = \begin{cases} 0 & te < \max(\tau - TI, 0) \\ \alpha \cdot e^{-TIR1_{bl}} \cdot e^{-teR2_{bl}} + \delta(0 - te) \cdot \frac{S_{bl}(TI)}{2 \cdot M_{a,0} \cdot f} & \max(\tau - TI, 0) < te < \tau_2 - TI \\ 0 & t > \tau_2 \end{cases} \quad \text{[E2.22]}$$

The exchange function is the same as equation E2.15 and outflow remains negligible. The magnetization decay function, $m2(t)$, is modified to include the T2 time constants:

$$m2_{bl}(te) = e^{-teR2_{bl}} \quad \text{[E2.23]}$$

$$m2_{ex}(te) = e^{-teR2_{ex}} \quad \text{[E2.24]}$$

It is important to note that the exchange term, $r_{exch}(t)$, and the time constant, Texch, introduced here describes the average time it takes labeled blood water to diffuse from the blood compartment into

the tissue compartment. In addition to diffusion, the transfer rate of labeled blood also depends on physiological factors, such as the partial capillary volume fraction (V_c) and permeability surface area (PS), thereby yielding the following relationship:

$$r_{exch}(t) = e^{-\left(\frac{PS}{V_c}\right)t} \qquad \text{[E2.25]}$$

Where,

$$\frac{PS}{V_c} = K_w = \frac{1}{T_{exch}} \qquad \text{[E2.26]}$$

It is this link in equation E2.26 between Texch and Kw that connects the two-compartment model theory of the two sequences and enables simulation studies to be performed with each set of equations.

2.4 Summary

Blood-brain barrier water exchange rate (Kw) is a promising parameter that has the potential to be a novel biomarker for both aging and different neurological disorders. Different groups have already begun to investigate how Kw changes with age and sex as well as correlating it with existing clinical markers such as body mass index, blood pressure, and various cognitive and metabolic measures. [20, 21, 49] However, clinical adoption of BBB ASL imaging like perfusion imaging with ASL would require additional validation studies, which is challenging as there currently is not set gold standard for assessing BBB integrity. Furthermore, future work needs to reconcile the opposite direction of water exchange rate between DW and ME ASL to better understand exactly what biological mechanism is being probed by the Kw modeling.

Moreover, it is important to highlight some of the key differences between ASL and DCE MRI, currently most popular magnetic resonance method to assess BBB exchange kinetics. [50] The primary benefit of DCE MRI is that the image is performed at a higher resolution than ASL. Yet, much like ASL, DCE MRI suffers from low signal-to-noise ratio. The key limitations of DCE MRI over ASL are that 1) DCE MRI utilizes toxic GBCAs which accumulates in the brain and damages kidney tissue and 2) because of the relatively large size of GBCAs compared to water molecules, DCE MRI is not as effective

as detecting subtle perturbations in BBB integrity versus ASL. The latter is, for instance, listed as one of the major limitations of a study that used DCE to study healthy normal aging. [51] Thus, the emerging investigation of using ASL to assess Kw, a proxy measure for BBB integrity, represents an exciting development that could see the addition of a new tool to the clinician's armamentarium.

In addition, it is important to discuss several key assumptions of the two-compartment model. First, we must assume that exchange happens the instance the tagged water molecules arrive at a given voxel. This assumption has been challenged by some groups with the integration of an intravascular transit time (ITT) term that simulates the time the water molecule spends in the muscular arterioles where no exchange occurs. [52] Second, there is an assumption of negligible venous outflow in the sense that all the labeled blood water molecules exchange into the tissue space. This is a valid assumption because, biologically, the tissue compartment is many orders of magnitude larger than the smaller capillary spaces where exchange occurs. Finally, the model also assumes a uniform capillary *PS* within a single voxel. Together, these assumptions are important attributes of the two-compartment model that ultimately estimates Kw within each voxel of the scan. Adjustments to these model features could impact the absolute value of the estimated Kw and represents an opportunity for future work to improve the overall accuracy of the Kw measurements.

To conclude, it is relevant to note that the Kw metric fitted by the two-compartment model is a relatively proxy for the health of the underlying anatomy. The model itself has numerous versions that tries to account for different compartments and timing associated with the cerebral vasculature. [13] Nevertheless, the adoption of any new neuroimaging method into clinical application would require a validation to existing modalities. For BBB exchange, this is an inherently tricky proposition as there currently does not exist a gold standard for measuring BBB water exchange. Thus, a multimodal approach and experimental set applying multiple existing BBB neuroimaging methods is determine if this Kw metric is useful in a clinical setting.

Chapter 3 Assessment of Choroid Plexus Perfusion with Arterial Spin Labeling MRI and ^{15}O-Water PET

3.1 Introduction

The choroid plexus is an organ that is often likened to a cauliflower because of its extensive surface folds. [53] It is located predominantly in the posterior lateral ventricles and produces cerebrospinal fluid (CSF), which plays an essential role in protecting the brain from trauma as well as in transporting and regulating molecules essential for neuronal metabolism. [54] The blood-CSF barrier, analogous to the blood-brain barrier, is endemic to the choroid plexus and physically partitions the vascular from the ventricular space. The function of the blood-CSF barrier choroidal epithelial layer, which secretes CSF, is likely disrupted with aberrant choroid plexus perfusion, which has also been implicated in a range of cerebrovascular and neurodegenerative disorders. [55-57] Historically, studying the choroid plexus in humans requires highly invasive surgical procedures or postmortem dissection, neither of which could reliably estimate normal healthy cerebral perfusion. Yet, recent advancements in arterial spin labeling (ASL) MRI have led to growing interest in noninvasively assessing choroid plexus perfusion and the functional status of the blood-CSF barrier. In fact, numerous studies have linked blood-CSF barrier dysfunction that arises from both acute and chronic inflammatory processes with various neurodegenerative and neuropsychiatric disorders such as Alzheimer's Disease and schizophrenia. [58-63] Additionally, ASL MRI may possess advantages over the current gold standard for assessing cerebral perfusion, ^{15}O-water PET, in studying choroid plexus perfusion, as there have been no literature reports on the use of PET to assess choroid perfusion in humans. Thus, establishing a reliable, noninvasive technique to measure choroid plexus perfusion could give researchers and clinicians insight into the health status of the brain and may serve as a prognostic biomarker for some neurological and neuropsychiatric disorders.

The choroid plexus receives its blood supply from the anterior, medial, and lateral choroidal arteries. [9] The anterior choroidal artery arises from the distal internal cerebral artery (ICA), while the medial and lateral posterior choroidal arteries originate from the posterior cerebral artery (PCA). Due to

the organ's high vascularization, choroid plexus perfusion quantification using ASL MRI in normal awake humans has been reported to be comparable, though slightly lower, than that of gray matter perfusion at around 56 ± 21 ml/100g/min with a range as broad as 25-90 ml/100g/min. [9, 57, 64, 65] The wide perfusion range for the choroid plexus may reflect that the choroid is more vascularized than gray matter and is known to respond to acute and chronic inflammatory stimuli that could alter its vasogenic properties and, consequently, its perfusion. [66]

The acetazolamide challenge is a useful clinical and research tool that reliably predicts critically reduced perfusion in patients with chronic steno-occlusive diseases. [67] In healthy individuals, it is a useful technique to assess the normal physiological response to a known vascular stimulus. Acetazolamide penetrates the blood-brain barrier slowly and inhibits carbonic anhydrase to induce acidosis and increased concentration of carbon dioxide, which is assumed to be the stimuli for the increase in flow. [68] Thus, acetazolamide induces an increase in cerebral blood flow like that evoked by carbon dioxide inhalation and can be attributed to vasodilation of arterioles due to a decrease in tissue pH. The vascular effects of acetazolamide on the choroid plexus have not been extensively studied in humans. However, a paper from 1990 using microspheres and a rabbit model found acetazolamide to increase blood flow to the choroid plexus by two-fold. [69]

ASL has been the predominant MRI technique to assess choroid plexus perfusion and has been combined with several methods to isolate the perfusion signal within the organ. Manual segmentation of the choroid plexus on a structural scan and masking the delineations onto an ASL perfusion image is considered the gold standard technique to isolate choroid-specific signals. [70, 71] Other approaches have included registering the ASL scans to a 4mm T_1-weighted Montreal Neurological Institute atlas. [9] More recently, some groups have begun to employ machine learning models to segment the choroid plexus tissue on T_1-structural images as an alternative to the more laborious manual segmentation. [57, 72] Aside from segmentation, Evans et al. took advantage of the CSF's long transverse relaxation time (T2) and employed an ultra-long time to echo (TE) in their ASL sequence to isolate the signal in the ventricles. [73] Importantly, their method captures the signal arising from ASL-tagged water molecules that have

passed through the blood-CSF barrier into the ventricles, thus assessing the functional status of the blood-CSF barrier. This sequence was first developed in rodents but eventually adopted by another group to be applied in healthy humans. [74] However, the major limitation of ultra-long TE ASL is the attenuation of choroid plexus-specific perfusion signal since its tissue has a shorter T2 time than CSF.

Moreover, noninvasive ASL imaging of cerebral blood flow has provided researchers with an invaluable tool to understand normal brain physiology and to identify and manage patients with different neurological disorders. [29] However, due to the methodological complexity of positron emission tomography (PET) imaging with short-lived radiotracers and the relative rarity of hybrid PET-MRI systems, few comparison studies directly juxtapose ASL perfusion measurements with ^{15}O-water PET, the established gold standard for assessing cerebral perfusion. [29, 75, 76] These comparison studies are critical to assess the reliability and accuracy of ASL perfusion measurements.

Thus, our study is a retrospective analysis of twelve healthy participants with ^{15}O-water PET and ASL MRI perfusion scans performed simultaneously on a hybrid PET-MRI system. [77] The purpose is to determine whether multi-post label delay (PLD) ASL MRI scans using a manual segmentation image processing pipeline can measure choroid plexus perfusion at baseline conditions and detect physiological changes associated with an acetazolamide vasodilation challenge. Furthermore, we also assessed the intrasession test-retest repeatability of our baseline ASL choroid plexus perfusion estimates and compared our findings with analogous measures from simultaneously collected ^{15}O-water PET. We hypothesize that ASL will perform as well as ^{15}O-water PET when assessing an organ as small as the choroid plexus.

3.2 Materials and Methods

3.2.1 Multi-Delay Arterial Spin Labeling MRI

We retrospectively investigated multi-PLD ASL scans of twelve healthy adult volunteers (age 22-53, 5 females), representing a subset of a previous study that underwent an acetazolamide challenge. [77] All images were acquired on a time-of-flight enabled 3.0 Tesla simultaneous PET/MRI system (Signa, GE Healthcare, Waukesha, WI), but the scans were not standardized to the same time of day. [78] The

ASL scans used pseudo-continuous labeling, a standard TE of 10.7 milliseconds, and had a 3-dimensional (3D) fast spin echo readout with stack-of-spirals trajectory. Multi-PLD ASL scans were 4 minutes and 46 seconds long with an in-plane resolution of 5.8mm x 5.8mm and a slice thickness of 4.0mm. The labeling duration (LD) was 2 seconds, and five equally spaced PLD times were acquired between 0.7 and 3.0 seconds. Each session consisted of three scans: two at baseline (Baseline 1, Baseline 2) and one 15 minutes after vasodilation (Post 3) with intravenous acetazolamide (15mg/kg dose, up to 1g). A timing diagram of the scan protocol can be found at the end of this chapter in Supplemental Figure 3.3.

All subjects received 3D T_1-weighted MRI with an inversion-prepared, fast spoiled gradient recalled sequence for anatomical registration. For analysis, we used FSLeyes (Analysis Group, Oxford, UK) to manually segment a mask of the choroid plexus on structural T_1 images that consists of a bilateral 3D region of interest of the choroid tissue in the posterior lateral ventricles. This can be seen in Figure 3.1. We chose to segment the choroid tissue only in the posterior lateral ventricles because this is the region where the choroid is most prominent and grossly visible on structural T_1 images. However, it is important to note that the choroid plexus is present in all four ventricles and, thus, that our segmentations do not capture the entirety of the organ. To help guide manual segmentation, the FSL FAST [79] tool was used to automatically differentiate the choroid plexus tissue from surrounding CSF and white matter. Additionally, we used the *recon-all* function in FreeSurfer software [18] to generate segmentations of the cortical gray matter.

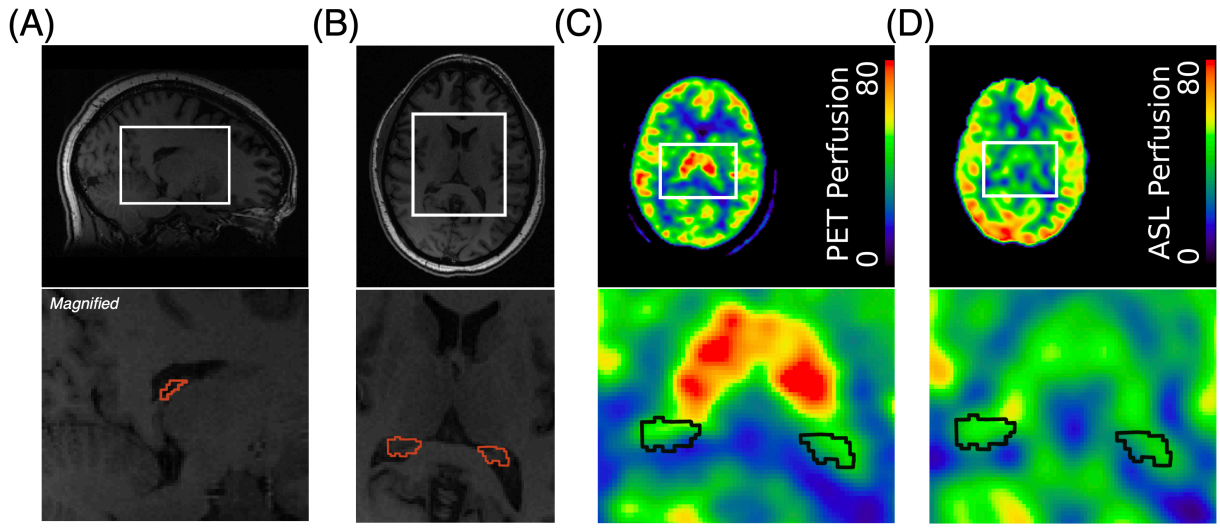

Figure 3.1: Signal extraction using manually segmented mask. Segmentation of the choroid plexus in (A) sagittal and (B) axial view in T_1 structural space for a single participant. Choroid mask segmentation outline in red. (C) PET perfusion map (ml/100g/min). (D) ASL perfusion map (ml/100g/min). Choroid mask segmentation outline in black.

FSL BASIL [80] was used to quantify perfusion and arterial transit time (ATT) maps in the structural T_1 space. Perfusion was calculated using an established two-compartment kinetic model. [81] Calibration was performed with the saturation recovery M_0 images in the voxelwise mode. Initial BASIL parameters were set at the standard values of 1.30 seconds for ATT, 1.30 seconds for T_1 tissue, 1.65 seconds for T_1 blood, and an inversion efficiency of $\alpha = 0.85$. Mean perfusion and mean ATT of the choroid plexus and cortical gray matter were extracted using in-house MATLAB scripts by overlaying the manually segmented choroid masks and Freesurfer-generated gray matter masks onto the BASIL-derived perfusion and ATT maps, respectively.

3.2.2 ^{15}O-water PET

PET scans were performed simultaneously with their corresponding ASL scans. Participants received manual, intravenous injections of ^{15}O-water (490-960Mbq) through an antecubital vein. The bolus duration was around 20 seconds, as estimated from the image-derived input functions. The decay

rate for ^{15}O was corrected for at the scanner before image reconstruction. PET reconstruction was performed with a TOF-OSEM algorithm (time-of-flight ordered subject expectation maximization; 4 iterations and 28 subsets) on a 192 x 192 matrix, 30cm field-of-view, 2.78mm slice thickness, and included correction for scatter, random counts, dead time, and point-spread function. [82] Dynamic PET frames over 4 minutes were reconstructed (30x1s, 10x3s, 12x5s, 12x10s).

To quantify PET perfusion maps, image-derived input functions of the ^{15}O-water tracer were calculated from dynamic PET signals in the carotid arteries. This image-based approach used simultaneous time-of-flight MRI angiograms (repetition time = 22.0 ms; TE = 2.4ms; in-plane spatial resolution = 0.43mm) from the same session to segment cervical arteries and correct for spill-in and spill-out artifacts on the lower-resolution PET images. [83] Parametric maps of CBF were separately modeled for each baseline and post-vasodilation condition, using the scan-specific input function and dynamic brain PET data over 4 minutes with a one-tissue compartment model in PMOD software (version 3.8; PMOD Technologies, Zurich, Switzerland).

3.2.3 Statistical Methods

For ASL, baseline and post-vasodilation choroid plexus and gray matter perfusion and ATT were compared. We used a mixed-effect linear regression model in MATLAB with the perfusion and ATT as dependent variables, baseline or post-vasodilation condition as the fixed effect, and the participant as the random effect. All group difference p-values between baseline and post-vasodilation were quantified using this model. The intraclass correlation coefficient (ICC) was calculated between Baseline 1 and Baseline 2, and a scatterplot and a Bland-Altman plot were generated for ASL perfusion between the two baseline runs.

For PET, K1 rate (perfusion) values for choroid plexus and gray matter were plotted in a boxplot for all three runs, and the ICC between choroid plexus perfusion from the two baseline PET scans was calculated. Similarly, a mixed-effect linear regression model was set up to calculate the group-level effect of acetazolamide, where the choroid plexus K1 rate (perfusion) was set as the dependent variables,

baseline or post-vasodilation condition as the fixed effect, and the participant as the random effect. A scatterplot and a Bland-Altman plot were created to show the intra-session test-retest reproducibility and agreement, respectively, of baseline perfusion values.

Histograms of choroid plexus and gray matter voxelwise perfusion distributions for ASL and PET at Baseline 1 and Post 3 conditions were created. Additionally, correlation analysis was performed with a statistical significance threshold $\alpha = 0.05$ by plotting the PET perfusion against ASL perfusion for all three runs. A mixed-effect linear regression model setting the PET perfusion as the independent variable and ASL perfusion as the dependent variable while holding the participants as the random effect was generated. Finally, a Bland-Altman plot was constructed to quantify the agreement between ASL and PET-measured perfusion. Bland-Altman plots were all created using R (R Core Team, 2021).

3.2.4 Mask Erosion

To investigate the influence of potential partial volume effects, we uniformly eroded our 3D choroid plexus masks across their surfaces using a 2D square structuring element with a width of 3 pixels in MATLAB. This size was equivalent to the resolution of the choroid mask. We then reran the analysis pipeline with the newly eroded masks and evaluated the resulting choroid plexus perfusion compared with perfusion obtained with the uneroded, original masks.

3.3 Results

Table 3.1 shows that the average choroid plexus perfusion between Baseline 1 and Baseline 2 was 38.9 ± 7.4 ml/100g/min for ASL and 37.8 ± 3.8 ml/100g/min for PET. For Post 3, the average choroid plexus perfusion increased to 63.5 ± 9.7 ml/100g/min ($p < 0.001$) for ASL and 45.7 ± 8.2 ml/100g/min ($p < 0.001$) for PET. The average gray matter perfusion between Baseline 1 and Baseline 2 was 46.8 ± 8.7 ml/100g/min for ASL and 45.5 ± 9.0 ml/100g/min for PET. For Post 3, the average gray matter perfusion increased to 66.4 ± 16.8 ml/100g/min ($p < 0.001$) for ASL and 54.9 ± 12.7 ml/100g/min ($p < 0.001$) for PET. The average choroid plexus ATT between Baseline 1 and Baseline 2 was 1.21 ± 0.19 seconds and

decreased to 1.05 ± 0.12 seconds ($p < 0.001$) for Post 3. Similarly, the average gray matter ATT between Baseline 1 and Baseline 2 was 1.25 ± 0.19 seconds and decreased to 1.08 ± 0.17 seconds ($p < 0.001$) for Post 3.

	Baseline 1	Baseline 2	Post 3	Baseline Average
ASL ChP Perfusion (ml/100g/min)	39.5 ± 9.8	38.3 ± 5.6	63.5 ± 9.7**	38.9 ± 7.4
ASL ChP ATT (seconds)	1.22 ± 0.24	1.20 ± 0.16	1.05 ± 0.12**	1.21 ± 0.19
PET ChP Perfusion (ml/100g/min)	38.3 ± 4.9	37.4 ± 4.1	45.7 ± 8.2**	37.8 ± 3.8
ASL GM Perfusion (ml/100g/min)	47.3 ± 8.4	46.3 ± 9.1	66.4 ± 16.8**	46.8 ± 8.7
ASL GM ATT (seconds)	1.23 ± 0.20	1.27 ± 0.20	1.08 ± 0.17**	1.25 ± 0.19
PET GM Perfusion (ml/100g/min)	46.4 ± 8.3	44.6 ± 10.1	54.9 ± 12.7**	45.5 ± 9.0

* $p < 0.05$, ** $p < 0.001$ compared to baseline average

Table 3.1: ASL and PET perfusion and arterial transit time (ATT) for choroid plexus (ChP) and gray matter (GM) for all three runs. The Baseline Average column is the mean perfusion or ATT between Baseline 1 and Baseline 2. (mean ± standard deviation)

Choroid plexus perfusion increased by an average of 24.6 ± 7.0 ml/100g/min ($p < 0.001$) and 7.8 ± 5.8 ml/100g/min ($p < 0.001$) for ASL and PET, respectively, while gray matter perfusion increased by an average of 19.6 ± 9.8 ml/100g/min ($p < 0.001$) for ASL and 9.4 ± 7.7 ml/100g/min ($p < 0.001$) for PET. This corresponds to a choroid plexus cerebrovascular reactivity (CVR) increase of 65 ± 22% and 20 ± 15% for ASL and PET, respectively, and a gray matter CVR increase of 41 ± 17% for ASL and 21 ± 17% for PET. Qualitatively, this trend can be further seen in Figure 3.4, in which the ASL post-vasodilation perfusion distributions for both choroid plexus and gray matter show a noticeable, uniform increase compared to the PET distributions. The mean decrease in choroid plexus ATT with vasodilation was 0.16 ± 0.15 ($p < 0.001$) seconds, which is comparable to the gray matter ATT decrease of 0.17 ± 0.12 seconds ($p < 0.001$).

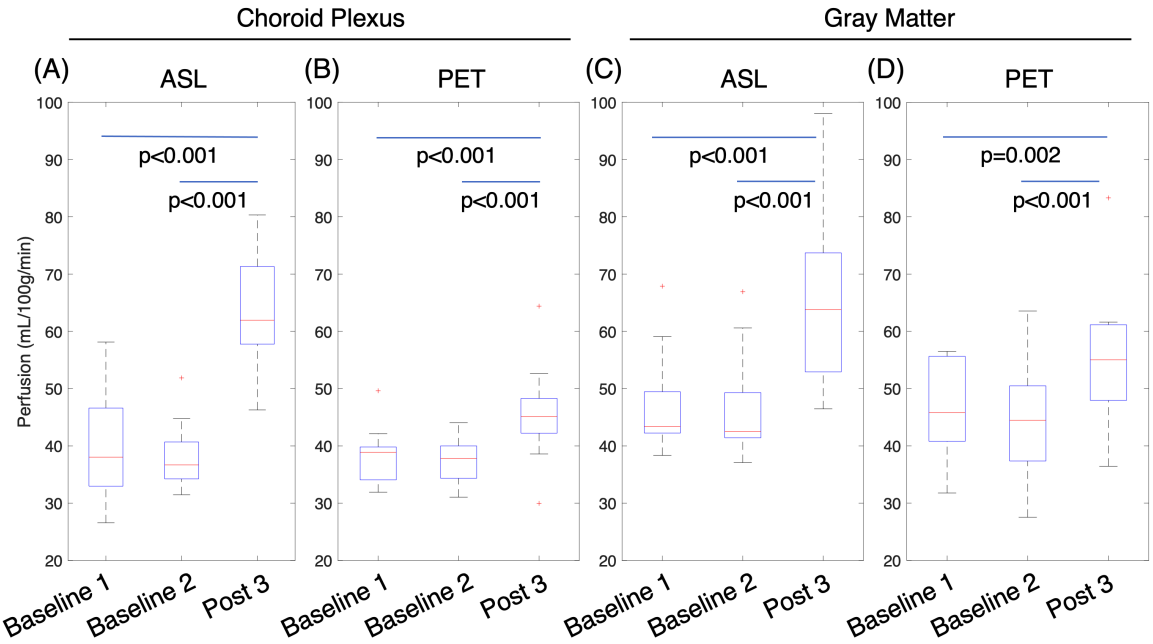

Figure 3.2: Choroid plexus and gray matter perfusion at baseline and post-vasodilation. **(A)**, **(B)** Choroid plexus and **(C)**, **(D)** gray matter perfusion at baseline and post-vasodilation.

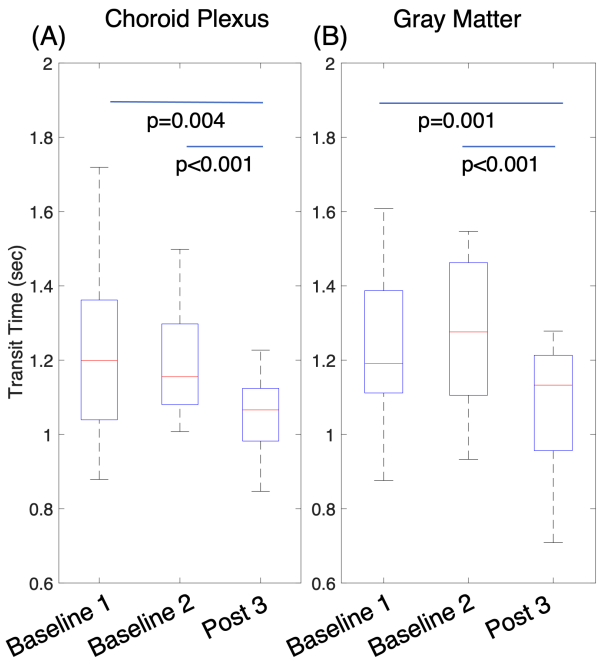

Figure 3.3: Baseline and post-vasodilation transit times for choroid plexus and gray matter. **(A)** Choroid plexus and **(B)** gray matter arterial transit times at baseline and post-vasodilation.

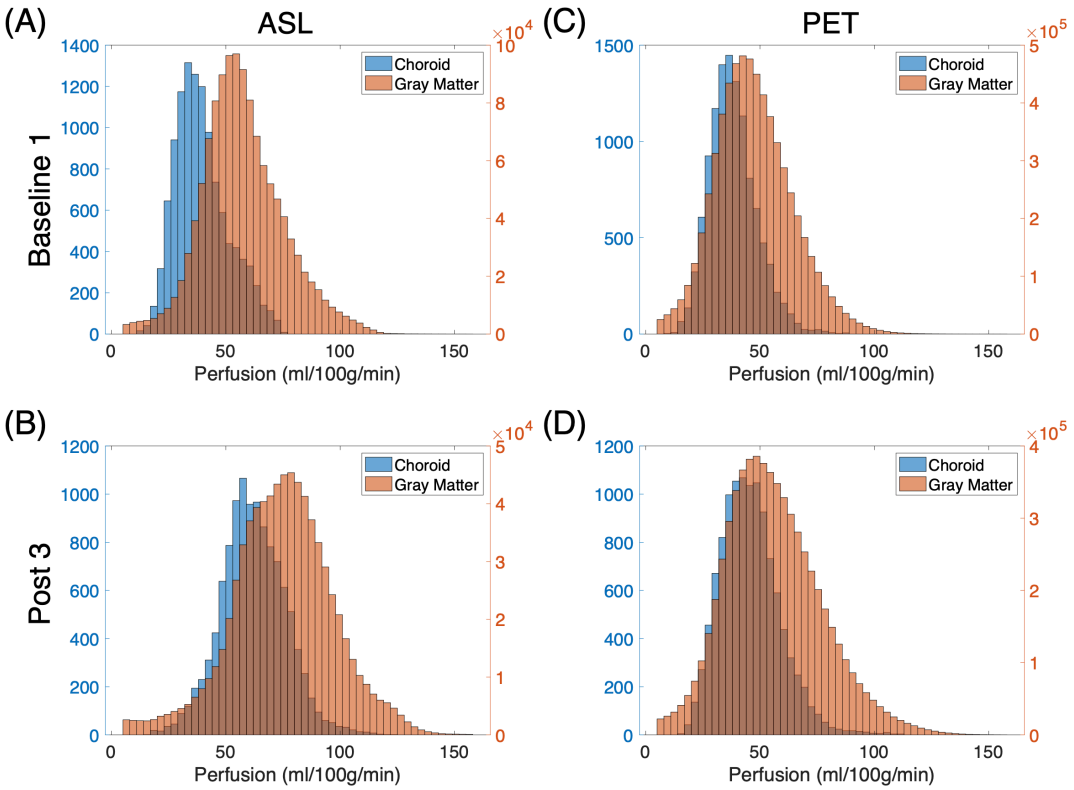

Figure 3.4: Histogram of choroid plexus and gray matter perfusion at baseline and post-vasodilation. **(A)**, **(B)** ASL and **(C)**, **(D)** PET perfusion distributions at baseline and post-vasodilation. Voxels with zero perfusion were excluded.

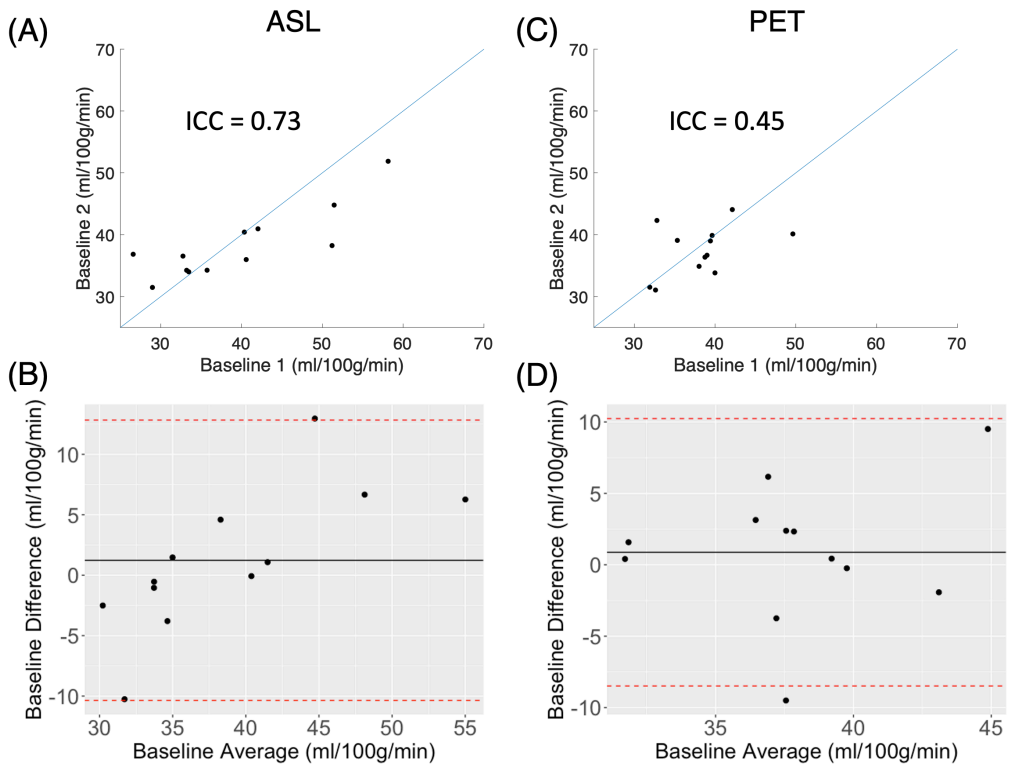

Figure 3.5: Scatterplots and Bland-Alman plots of baseline choroid plexus perfusion measurements for ASL and PET. Scatterplots and Bland-Altman plots for **(A)**, **(B)** ASL and **(C)**, **(D)** PET choroid plexus perfusion measurements at two baseline runs.

Figure 3.5 assessed the repeatability of choroid perfusion via scatterplots comparing Baseline 1 plotted against Baseline 2 for both modalities. The ICCs between ASL and PET baseline perfusion measurements were 0.73 and 0.45, respectively. Furthermore, the ICCs for gray matter ASL and PET baseline perfusion were 0.98 and 0.87 (Supplementary Figure 3.3). Bland-Altman plots show good agreement between the two baseline runs for choroid and gray matter perfusion.

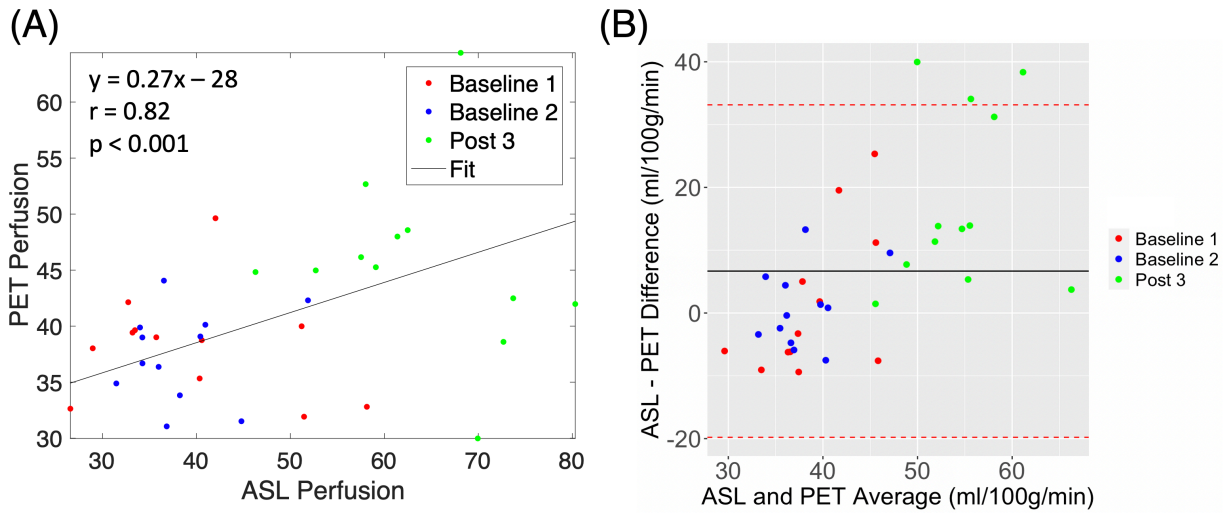

Figure 3.6: Correlation analysis between ASL and PET perfusion measurements for all runs. **(A)** Correlation plot and **(B)** Bland-Altman plot between ASL and PET perfusion measurements for all three runs.

Correlation analysis of PET with ASL for choroid perfusion across all three runs showed significance with a slope of 0.27 ($r = 0.82$, $p < 0.001$). Figure 3.6 shows the mean difference between ASL and PET choroid plexus perfusion in the Bland-Altman plot, suggesting the presence of a mean bias of around 7 ml/100g/min between the two modalities.

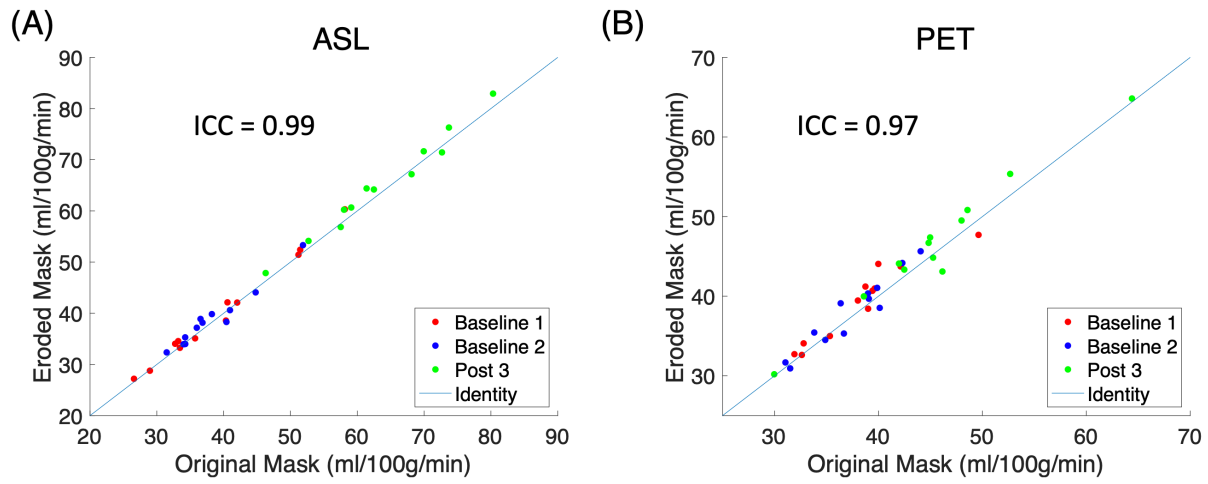

Supplemental Figure 3.1: Scatterplots of choroid plexus perfusion quantified with original and eroded masks. Comparison of choroid plexus perfusion quantified with original choroid masks and eroded choroid masks for **(A)** ASL and **(B)** PET.

Supplementary Figure 3.1 plots the choroid plexus perfusion metrics quantified with the original masks against those quantified with the eroded masks and shows excellent overall agreement for both ASL and PET, with an ICC of 0.99 and 0.97, respectively. Furthermore, Bland Altman plots in Supplementary Figure 3.2 confirm that there is good agreement between the choroid plexus perfusion metrics obtained with the two sets of masks.

3.4 Discussion

In this work, we retrospectively analyzed simultaneously collected multi-PLD ASL MRI and ^{15}O-water PET data and found the two modalities to be concordant in their baseline measurement of choroid plexus perfusion and in their measurement repeatability at baseline conditions. Furthermore, both ASL and PET successfully detected increases in choroid plexus perfusion with acetazolamide vasodilation challenge, though with some discrepancies in the magnitude of that change. Our results suggest that noninvasive and nonionizing multi-PLD ASL could be useful for assessing choroid plexus perfusion

status in human subjects, thereby providing clinicians and scientists with a possible method to study the functional status of a key organ considered the "starting point" of the glymphatic system. [2]

Baseline choroid plexus perfusion was measured to be 38.9 ± 7.4 ml/100g/min for ASL and 37.8 ± 3.8 ml/100g/min for PET. Gray matter perfusion showed similar consistency between the two modalities at 46.8 ± 8.7 ml/100g/min for ASL and 45.5 ± 9.5 ml/100g/min for PET, consistent with a previous ^{15}O-water PET study measuring perfusion in the cortical gray matter. [65] Inter-individual differences in choroid perfusion may reflect different diurnal variations since the time of day was not constant, and CSF flow varies across the day. These are consistent with previously reported literature values of choroid plexus perfusion. [57] When considering that these choroid plexus perfusion values come with partial volume effects, Zhao et al. [70] used the term "apparent" rather than "absolute" to describe their choroid perfusion, and Eisma et al. also measured apparent choroid perfusion without using the adjective in their paper. Additionally, Zhao et al. corrected the apparent blood flow, estimated at 39.5 ± 10.1 ml/100g/min, with the choroid plexus tissue density, assumed to be the same as that of the brain's parenchyma at 1.08 g/ml. Voxelwise partial volume weighting factors yielded a corrected blood flow of 80 ml/100g/min, nearly twice the magnitude of the original value. Because choroid plexus tissue and the CSF intermingle at a microscopic level, it is theoretically impossible to exclude a partial volume of CSF in the choroid plexus voxels at any achievable MRI resolution with a segmentation that has a uniform value across all the regions of interest. Thus, our reported perfusion values can be characterized as apparent choroid plexus blood flow.

ASL and PET measured choroid plexus perfusion between Baseline 1 and Baseline 2 with comparable repeatability. The ICCs for ASL and PET calculated for all 12 participants were 0.73 and 0.45, respectively, which suggests that ASL has higher repeatability than PET for assessing choroid plexus perfusion. Moreover, the ICCs for ASL and PET between Baseline 1 and Baseline 2 for gray matter tissue were 0.98 for ASL and 0.87 for PET, which further suggests ASL repeat measurements to be more consistent than PET's. However, it is important to consider that ICC is not a direct measure of

repeatability but rather a measure of the repeat scan variance relative to the inter-subject variance. This is the reason why potential outliers or high inter-subject variability can make ICC high despite relatively low test-retest variability. [84] Additionally, while the good agreement between the two ASL baseline scans is encouraging, this finding does not speak to the measurement accuracy of the absolute ASL perfusion values, though it is encouraging that they are consistent with the PET gold standard at baseline. Finally, the ICC for gray matter perfusion approached 0.98 with ASL but was only 0.73 for choroid plexus perfusion. While certainly the large difference in ROI size may contribute to this discrepancy, other differences such as the vascular architecture of gray matter tissue versus the choroid plexus may also contribute to the observed difference in ICC.

Both ASL and PET exhibited significant increases in choroid plexus and gray matter perfusion with acetazolamide vasodilation. Figure 3.4 shows that the overall choroid plexus perfusion distribution moves closer to the gray matter distribution with vasodilation, further confirming that the choroid plexus organ has a higher cerebrovascular reactivity than gray matter. Physiologically, the observation of higher perfusion with vasodilation is reasonable as both the choroid plexus and gray matter are highly vascularized tissues. Vasodilation decreases the vascular resistance of arterioles, which ultimately results in an increase in blood flow into the capillary beds of the choroid and gray matter tissue.

Although both ASL and PET detected robust choroid plexus perfusion increase with vasodilation, ASL measured a larger absolute increase than PET (Figure 3.3): 24.6 ± 7.0 ml/100g/min for ASL compared to 7.8 ± 5.8 ml/100g/min for PET. The larger increase in choroid plexus perfusion with vasodilation in ASL versus PET is also seen in gray matter tissue. All in all, this suggests there is an underlying bias between the two modalities. One potential reason for this discrepancy is because of decreased ^{15}O-water tracer uptake at high flow rates, which have been reported in the literature to be greater than or equal to 70 ml/100g/min. [85] The median for our ASL assessment of gray matter perfusion for Post 3 is 66.4 ± 16.8 ml/100g/min, while the median for our PET assessment is 54.9 ± 12.7 ml/100g/min, meaning that decreased ^{15}O-water tracer uptake is a possible explanation for the

discrepancies between ASL and PET measurement of gray matter perfusion post-vasodilation. Additionally, it is the roughly twofold increase in choroid plexus perfusion, as seen in ASL with acetazolamide vasodilation, that is consistent with the findings of a previous 1990 study done in rabbits by Faraci et al. using microspheres. [69] Thus, ASL may possess some advantages over PET in assessing perfusion in both tissue types at higher flow rates.

Furthermore, it is important to contextualize ^{15}O-water PET-acquired noninvasive imaging of absolute choroid plexus perfusion with previously performed invasive methods in animal models. Using injected microspheres, choroid plexus perfusion has been measured to be from 287 ml/100g/min in dogs [86] to 601 ml/100g/min in sheep [87], with both metrics significantly higher than what we and others [57, 70] have reported in humans using the ASL and PET modalities. A probable explanation for this discrepancy is that our neuroimaging studies are underestimating the true choroid plexus perfusion in humans because of the microscopic sharing of space between the choroid tissue and CSF that leads to partial volume effects, which impacts both the ASL and PET scans as identical masks are used to isolate the choroid perfusion signal in quantification. Furthermore, ^{15}O-water PET perfusion measurements are derived from the one-tissue compartment model, the simplest PET model that describes the bidirectional tracer flux between blood and tissue. [88] At the flow rates measured invasively in animals, both the extraction and the residence time of the ^{15}O-water tracer would likely be lower, and, consequently, the measured perfusion, even with the PET gold standard, would be less than the ground truth.

The ATT is an additional measure that is available through ASL but not PET and, for both choroid plexus and gray matter, significantly decreased following vasodilation by 0.16 ± 0.15 seconds and 0.17 ± 0.12, respectively. Physiologically, a decrease in ATT with vasodilation is expected because vasodilation with intravenous acetazolamide has global effects and will decrease the vascular resistance of major neck arteries and smaller arterioles surrounding the choroid plexus. Enlarged vessel diameters mean that the labeled blood water molecules will experience less resistance while traveling to the choroid plexus, thereby contributing to a shorter ATT. [89]

Correlation analysis of ASL and PET choroid plexus perfusion considering Baseline 1, Baseline 2, and Post 3 shows that these two modalities are significantly correlated to each other with a slope of 0.27 ($r = 0.82$, $p < 0.001$) (Figure 3.6A). This suggests that it is the within-subject changes induced by acetazolamide vasodilation that are driving the correlation with all three runs. This limitation of our study should be addressed in future studies, including larger sample sizes with a wider dynamic range of choroid plexus perfusion. Additionally, the Bland-Altman plot suggests a small residual bias of around 7 ml/100g/min between the ASL and PET with ASL consistently overestimating choroid plexus perfusion measurements. This trend is driven mostly by the Post 3 groups (Figure 3.6B).

As previously discussed, partial volume effect is a limitation of our study. The choroid plexus is a relatively small organ with an anatomical thickness of roughly 3mm [90], which is in the same magnitude as the dimensions of a standard ASL voxel (5.8mm x 5.8mm x 4mm) or PET voxel (1.6mm x 1.6mm x 2.8mm). The consequence of having voxels with dimensions in the same order of magnitude as the organ of interest is that there could be a mix of different tissue types within each voxel that overlaps with the choroid plexus ROI. Since white matter and CSF, which are adjacent to the posterior lateral choroid tissue, are associated with low or no perfusion, respectively, our apparent choroid plexus perfusion could be an underestimation of the absolute perfusion. Moreover, partial volume effect influences both the ASL and PET modality in our choroid plexus analysis, meaning that even though ^{15}O-water PET is the current gold standard in assessing cerebral perfusion, it may not be the case for choroid plexus perfusion using the methods employed.

To address partial volume effects in ASL, various partial volume correction (PVC) algorithms exist that recalculate the ASL or PET perfusion maps by considering the proportion of white matter, gray matter, or CSF contained within each ASL or PET voxel using the T_1 structural image and then applying a tissue-specific weight to that voxel's perfusion value. [91] In fact, recent developments in PVC algorithms have shown that the traditional assumption of zero weighting for CSF tissue results in the underestimation of the actual CSF signal contribution to the ASL signal. [92] Nevertheless, as previously

mentioned, complete partial volume correction for the choroid plexus blood flow is complex as CSF is microscopically intertwined within the numerous surface folds of choroid tissue. [70] ‘

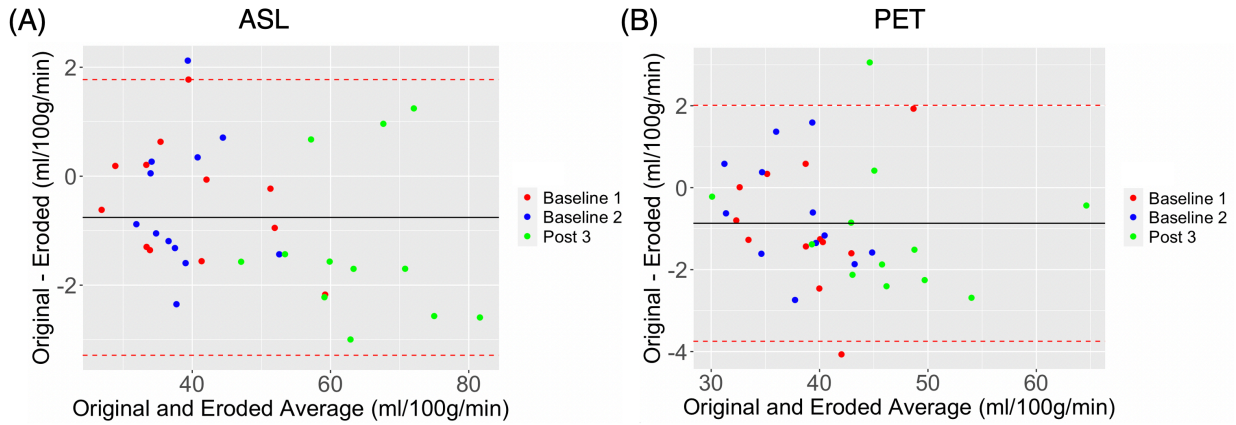

Supplemental Figure 3.2: Bland-Altman plots of choroid plexus perfusion quantified with original eroded masks. Bland-Altman plot for **(A)** ASL and **(B)** PET to assess the agreement of choroid plexus perfusion quantified with original versus eroded masks.

Given the limitations of PVC, we decided to assess the consequence of partial volume effects associated with voxels at the boundaries of our manual segmentations by eroding our masks uniformly across their surfaces. The purpose of erosion is to exclude boundary voxels where choroid plexus tissue may interface with other tissue types, such as white matter or CSF, to ignore potentially confounding ASL signals. Results show high repeatability (Supplemental Figure 3.1) and high agreeability (Supplemental Figure 3.2) between choroid plexus perfusion assessed with and without erosion. Overall, this suggests that the partial volume effect associated with voxels at the boundary of different tissue types is not a significant factor in our analysis.

Another limitation of our study is that our dataset was not equipped to assess total CSF volume, which would have made for a more comprehensive analysis given that acetazolamide is a carbonic anhydrase inhibitor that also decreases CSF production. In rodent models, acetazolamide has been shown to reduce CSF by up to 55% [93], and it is also used therapeutically to reduce CSF in conditions such as idiopathic intracranial hypertension. Decreased CSF production would alter the amount of magnetically

labeled water molecules passing through the blood-CSF barrier into the ventricular space, thereby potentially altering the overall ASL and PET signal in the tissue.

To conclude, the discovery of the glymphatic system [1, 2, 4, 94] has led to growing interest in studying structures associated with the waste clearance system of the brain. The choroid plexus, the primary producer of CSF, is an important structure of the glymphatic system, and its perfusion has been correlated with the functional status of this organ. Thus, establishing a noninvasive method such as multi-PLD ASL to assess choroid plexus perfusion in humans will give researchers and clinicians a new tool for monitoring the organ's status in both healthy and diseased states.

3.5 Conclusion

Noninvasive and nonionizing multi-PLD ASL MRI can robustly assess choroid plexus perfusion at baseline conditions, detect physiological changes in choroid perfusion with acetazolamide challenge, and possess repeatability under baseline conditions comparable to ^{15}O-water PET; however, additional studies are needed to affirm the accuracy of the perfusion values at high flow rates to validate this relatively new technique.

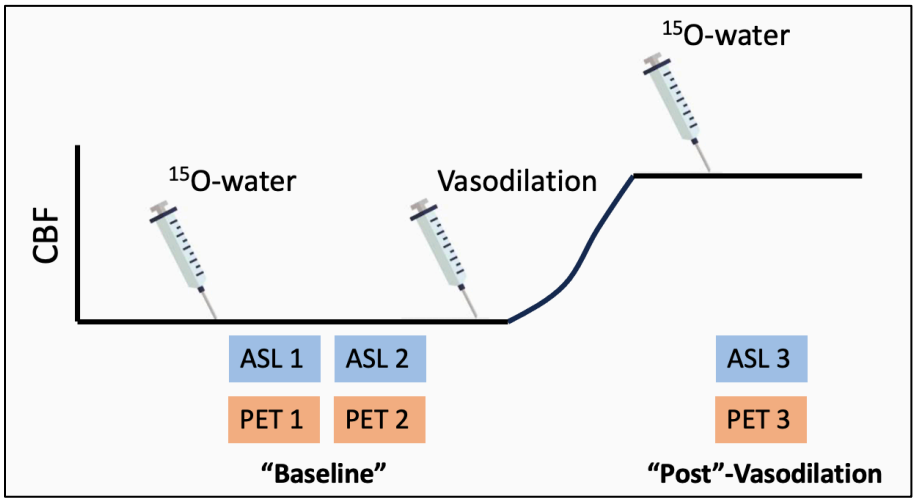

Supplemental Figure 3.3: Timing diagram of the scanning protocol.

Chapter 4 Repeatability of Diffusion Weighted Arterial Spin Labeling MRI for Mapping Blood-Brain Barrier Water Exchange Rate at Different Post-Label Delays

4.1 Introduction

Altered blood-brain barrier (BBB) function and permeability has been shown to be a feature of many common neurological and neuropsychiatric disorders. [95-98] Diffusion-weighted (DW) arterial spin labeling (ASL) MRI is an emerging and promising noninvasive, nonionizing, and contrast-free technique to assess BBB water exchange rate (Kw), a proxy measure of BBB integrity and function. The use of magnetically labeled blood water molecules as endogenous tracer makes applications in young, healthy brains and longitudinal studies possible without having to worry about contrast toxicity or ionization effects. [26, 99-101] Additionally, the relatively small size of water molecules (~ 18 Da) compared to gadolinium-based contrast agents (GBCAs) (Gd-DTPA 550 Da) enables the detection of different and potentially more subtle BBB impairment. Thus, a validated, noninvasive ASL method to measure BBB Kw will give researchers a new and more sensitive tool to study the brain. [102]

In an ASL scan, the post-label delay (PLD) is an important sequence parameter that represents the time after the labeling duration (LD) at which an image of the magnetically labeled bolus in the brain is taken. The labeling plane for pseudo-continuous ASL (PCASL) is positioned at the major neck arteries. [103] Once the blood water molecules are labeled, it takes a certain amount of time for those molecules to reach the brain capillaries and cross the BBB into the brain parenchyma. Depending on this arterial transit time (ATT), a physiological parameter formally defined as the amount of time a magnetically labeled water molecule takes to travel from the labeling plane to the capillary of a given brain voxel, the PLD need to be optimized to allow labeled spins enough time to reach the brain region of interest and maintain sufficient signal-to-noise ratio (SNR). While the optimal PLD has been studied extensively for assessing cerebral blood flow (CBF) with single-delay ASL [33], there is a lack of studies that examine the effect of PLD on the reliability of Kw assessment. Furthermore, ATT has been shown to increase with disease that alters brain vascular health as well as with age. [104-106] Thus, PLD selection is a critical aspect of BBB ASL study design especially when applied in populations with altered ATT.

Water flows freely, though controlled, across the BBB primarily through transmembrane aquaporin (AQP) channels whose aberrant expression contributes to decreased Kw measured in different disease states using the DW ASL method. [45, 107-111] Nevertheless, findings using different BBB imaging techniques [37, 52] and disease-related impact on alternate routes of water exchange have complicated this interpretation and, to date, the field is still uncertain about the direction of Kw change with disease and aging. The theory behind how Kw is estimated in this sequence, called the two-stage single-pass approximation (SPA) model, was first published by St. Lawrence et al. [36, 42] and relies on the ~100 fold difference in pseudo diffusivities (D) of blood and tissue [112] to separate the overall ASL signal into an intravascular (blood) and extravascular (tissue) component from which Kw can then be extracted. The 3D single delay DW ASL sequence was pioneered by Shao et al. [113], whereby a diffusion gradient (*b*-factor) is applied to crush the fast-flowing spins to differentiate the intravascular and extravascular components from the total signal for every voxel. Initial tests were performed on healthy participants before applications in a cohort with small vessel disease. [113] Test-retest MRI scans done approximately 6 weeks apart reported a range of intraclass correlation coefficients (ICC) across regions from 0.17 in the para hippocampal gyrus, a relatively smaller structure, to as high as 0.72 in the frontal lobe.

Additional studies are needed to affirm the reliability of ASL MRI sequences that assess Kw. [112, 113] Thus, the purpose of our work is to assess the intrasession repeatability of DW ASL sequence at different post-label delays (PLDs) to examine the effect of PLD on regional Kw measurements between two intrasession scans. Furthermore, we performed simulation studies by generating simulated ASL signals with the two-compartment model at a range of ATTs and at three different Kw values and PLDs to understand the robustness of the Kw fitting algorithm to added Gaussian noise.

4.2 Theory

4.2.1 Two-Compartment Model

The two-compartment model was founded on the principle that the ASL signal, $\Delta M(t)$, originate from either a vascular (blood), $\Delta M_{bl}(t)$, or extravascular (tissue), $\Delta M_{ex}(t)$, component characterized by the unique relaxation times and diffusion coefficients of the spin labels in those compartments. [37]

$$\Delta M(t) = \Delta M_{bl}(t) + \Delta M_{ex}(t) \quad \text{[E4.1]}$$

The general kinetic model [48] defines the components of the ASL signal as the convolution over the input function, $c(t)$, with a residue functions that generally model signal loss due to different factors such as blood-to-tissue water exchange, r_{exch}, magnetization decay, m, and venous outflow, r_{out}.

$$\Delta M_{bl}(t) = 2 \cdot M_{a,0} \cdot CBF \cdot \int_0^t c(t') \cdot r_{exch}(t-t') \cdot m_{bl}(t-t') \cdot r_{bl,out}(t-t')dt' \quad \text{[E4.2]}$$

$$\Delta M_{ex}(t) = 2 \cdot M_{a,0} \cdot CBF \cdot \int_0^t c(t') \cdot (1 - r_{exch}(t-t')) \cdot m_{ex}(t-t') \cdot r_{ex,out}(t-t')dt' \quad \text{[E4.3]}$$

Where CBF is perfusion in ml/100g/min, $M_{a,0}$ is the arterial longitudinal equilibrium magnetization. The ATT and labeling duration LD represents the limits of integration for $c(t)$ (A4.1). Refer to the Appendix for the full model.

4.2.2 Diffusion-Weighted Arterial Spin Labeling MRI

The blood and tissue components of the signal $\Delta M_{bl}(t)$ and $\Delta M_{ex}(t)$, respectively, can be separated by their different sensitivities to diffusion-encoding gradients so that the ASL signal collected at a given PLD with multiple diffusion-weighting (i.e. *b* values) can be thus modeled by a bi-exponential equation [114]:

$$\frac{\Delta M(t,b)}{\Delta M(t,0)} = A_1(t)e^{-bD_1} + A_2(t)e^{-bD_2} \quad \text{[E4.4]}$$

Where the weighting factors A_1 and A_2 are the fractions of the blood and tissue components, respectively, of the ASL signal curve (Figure 4.1A) and D_1 and D_2 are the corresponding apparent diffusion coefficients. Using the definitions of $\Delta M_{bl}(t)$ and $\Delta M_{ex}(t)$, the weighting factors are given by:

$$A_1(t) = \frac{\Delta M_{bl}(t)}{\Delta M_{bl}(t)+\Delta M_{ex}(t)} \text{ [E4.5] and } A_2(t) = \frac{\Delta M_{ex}(t)}{\Delta M_{bl}(t)+\Delta M_{ex}(t)} \text{ [E4.6]}$$

Here, the expressions for A_1 and A_2 contains two unknown variables (K_w and ATT) if we trace the model back to equations E4.2 and E4.3. In the DW ASL protocol, ATT is measured separately so that, ultimately, the equation for A_1 is solved for the primary imaging measure of interest: K_w, defined as the capillary permeability surface-area product of water (PS_w) divided by distribution volume of water tracer in the capillary space (V_c).

Furthermore, these terms, which are functions of time, will change in magnitude depending on the PLD. In this study, the ΔM data is acquired at two b values: zero (b_0) and a larger value (b_{DW}) at a sufficient strength to suppress the vascular signal, but with minimum effect on the tissue signal. In this case, A_1 and A_2 are defined as:

$$A_1(t) = 1 - \frac{\Delta M(b_{DW})}{\Delta M(b_0)} \text{ [E4.7] and } A_2(t) = \frac{\Delta M(b_{DW})}{\Delta M(b_0)} \text{ [E4.8]}$$

4.3 Materials and Methods

4.3.1 Numerical Simulation

Figure 4.1A is a plot of the simulated ASL kinetic signal showing the total signal (blue) and its intravascular (red) and extravascular (green) components from the two-compartment model. The ATT and the peak of the kinetic curve are both labeled as well as representative schematic of where PLD 1500ms, 1800ms, and 2100ms sample the ASL kinetic signal to calculate the blood signal fraction, $A_1(t)$, from which Kw is extracted. Figure 4.1B shows the theoretical $A_1(t)$ curve as a function of time. Here, it is evident that the A_1 amplitude is dependent on the Kw and PLD in addition to the set ATT of that voxel. Supplemental Figure 4.1 shows the A_1 distributions for each PLD and Kw with added white Gaussian noise, as described below.

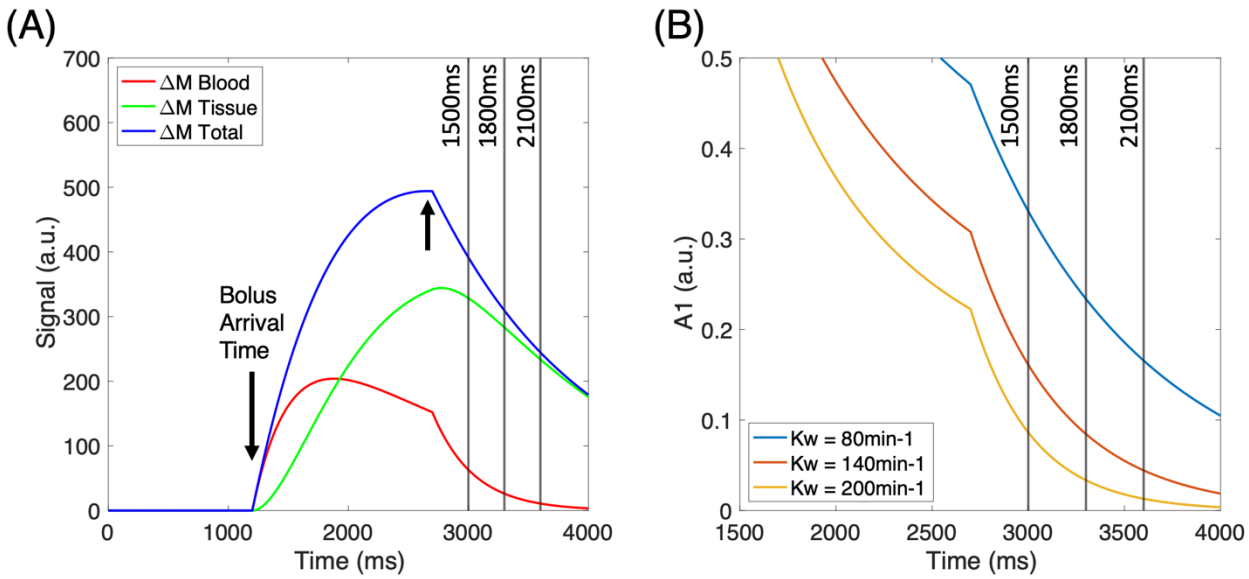

Figure 4.1: ASL kinetic model. **(A)** ASL signal split into the total, blood, and tissue components through the two-compartment model. A downward-facing arrow denotes bolus arrival time at 1.2s, while an upward-facing arrow denotes the kinetic curve peak. The labeling duration (LD) of 1.5s is the distance between the two arrows. Kw was set at 140min^{-1}. Gray vertical lines represent the three post-label delays (PLD). **(B)** A1 signal fraction curve representing the blood signal divided by the total signal.

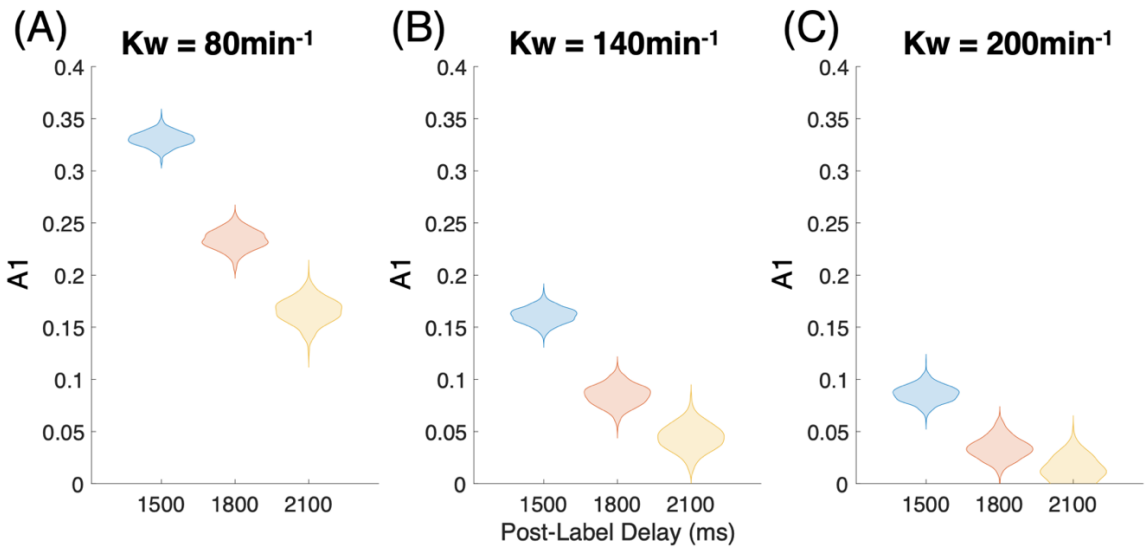

Supplemental Figure 4.1: A1 blood signal fraction at three post-label delays (PLDs) with added random Gaussian white noise for Kw value of (A) 80min^{-1}, (B) 140min^{-1}, and (C) 200min^{-1}.

To investigate the robustness of the Kw fitting protocol to Gaussian noise, simulations in MATLAB were performed at PLD [1500ms 1800ms 2100ms], Kw [80min^{-1} 140min^{-1} 200min^{-1}], and a range of ATTs from 500ms to [3000ms, 3300ms, 3600ms], corresponding to the PLD and spaced by 100ms. These values reflect the *in vivo* acquisition parameters as well as expected and extreme physiological Kw [107, 113] and ATT [115], respectively. Using the two-compartment model theory [37], fractional diffusion-weighted ASL signals (A_1 and A_2), with, $\Delta M(b_{DW})$, and without, $\Delta M(b_0)$, diffusion weighting, which crushes the intravascular blood signal, were simulated for a single voxel. Simulation parameters include: CBF = 60 ml/100g/min, labeling efficiency $\alpha = 0.77$ [113], blood-water partition coefficient $\lambda = 0.9$, labeling duration LD = 1.5s, $R1_{bl} = 0.6s^{-1}$ [116], and $R1_{ex} = 0.77s^{-1}$ [117].

Monte Carlo simulations were performed in which random white Gaussian noise was added to the simulated ASL signal before estimating Kw. We chose Gaussian noise was added because it is assumed that noise in MRI greater than SNR of 2 follows this distribution. [118] $M_{0,bl}$ was first estimated from an *in vivo* brain tissue reference acquired at PLD 2000ms without background suppression. For each combination of underlying Kw, ATT, and PLD, $A_1(t)$ was calculated by simulating $\Delta M(b_{DW})$ and $\Delta M(b_0)$ using the theoretical equations at a specific PLD time. For each iteration, noise was then added to the corresponding A_1 using a standard deviation (SD) of 0.2% of $M_{0,bl} = 1200\ a.u.$ for ASL according to the method described by Woods et al. [119] Noise was added separately to the A_1 numerator and denominator (equation E4.5) at an SNR that varies with the blood and tissue signal strengths, which in turn is dependent on the PLD, ATT, and Kw. Kw was then estimated from simulated noisy A_1 using the *fzero* function in MATLAB, and the percent error from the known ground truth Kw was calculated. This process was repeated 1000 times per ATT at 3 different PLDs and 3 different Kw values.

4.3.2 Imaging Protocol

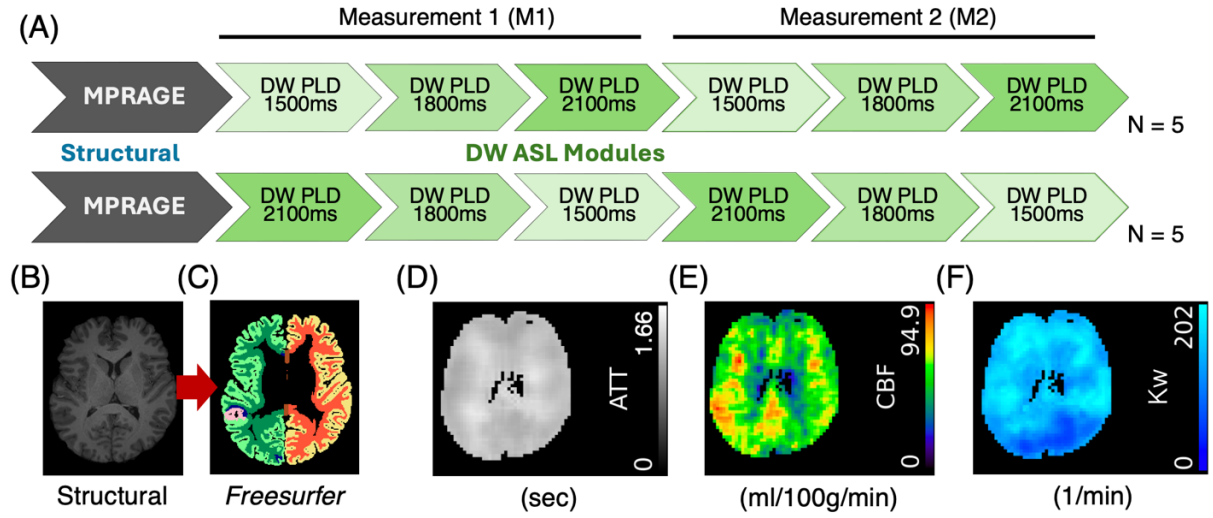

Figure 4.2: Scanning protocol of the ten participants. **(A)** Separate diffusion-weighted (DW) ASL MRI scans were acquired at DW post-label delays (PLDs) of 1500, 1800, and 2100ms. **(B)-(C)** Structural T1 image and *FreeSurfer* gray and white matter masks. **(D)-(F)** Water Exchange Quantification Toolbox generated cerebral blood flow (CBF), arterial transit time (ATT), and water exchange rate (Kw) maps.

10 young, healthy adults (aged 23-30y, 5 females) were scanned on a 3T Magnetom Skyra (Siemens Healthineers, Erlangen, Germany) MRI with a 32-channel head coil (Figure 4.2). All participants gave informed consent under a protocol approved by the Institutional Review Board (IRB). T1-weighted magnetization prepared rapid gradient echo sequence (MPRAGE) structural images [120] were acquired at resolution = 1.0 × 1.0 × 1.0 mm^3, followed by three 3D gradient-and-spin-echo (GRASE) diffusion-weighted (DW) ASL scans, representing measurement 1 (M1), to assess Kw at PLDs of 1500ms, 1800ms, and 2100ms. These three DW ASL scans were then repeated within the same scan session for measurement 2 (M2) to assess the intrasession repeatability at each PLD. In half (or five) of the participants, the PLD order was reversed to minimize ordinal bias. The flow encoding arterial spin tagging (FEAST) [47] acquisition to measure ATT is incorporated into each DW ASL scan and was kept identical (with PLD of 900ms) across all repetitions. In four participants, we also performed a sensitivity study by setting the PLD at an extremely low value of 500ms and an extremely high value of 3000ms.

The DW ASL sequence was acquired at TR = 4s, TE = 36.5ms, FOV = 224mm, matrix size = 64 × 64, 12 slices (10% oversampling), resolution = 3.5 × 3.5 × 8 mm^3, label/control duration = 1500ms, and centric ordering. [110, 113] DW ASL scans included 20 repetitions with diffusion weightings (*b*-value) at 0 and 50s/mm^2 to measure Kw, which lasted 6 minutes. Each DW ASL scan also included a FEAST acquisition with 15 repetitions at a diffusion weighting (*b*-value) of 0 and 14s/mm^2 with a total acquisition time of 4 minutes to estimate ATT. Therefore, the total time for each scan was 10 minutes. The slice prescription was aligned with the top of the brain so that as much of the superior cortical structures could be covered as possible.

4.3.3 Postprocessing

The DW ASL raw scan data was processed with the Water Exchange Quantification (WEQ) Toolbox to generate whole-brain ATT, CBF, and Kw maps, as well as global averages. [121] A two-stage single-pass approximation (SPA) model was used to measure arterial transit time (ATT) and Kw. [36] We used FreeSurfer [18] to segment the structural T_1 into 35 gray matter regions of interest (ROIs) in each hemisphere using the *recon-all* function. The output parametric maps were then linearly registered and resampled to the skull-stripped FreeSurfer structural T_1 images in FSL FLIRT using the nearest neighbor option. In MATLAB, the FreeSurfer masks were overlayed onto the registered ATT, CBF, and Kw maps to extract the average parameter in each gray matter ROI. Furthermore, for each ROI, we calculated the percent voxel coverage and excluded regions with less than 60% coverage. Our *in vivo* analysis was performed by averaging the values within each FreeSurfer ROI across all participants who meet the 60% voxel coverage threshold criterion. Analysis with participant-specific values of gray matter ROIs is provided in Supplemental Figure 4.2.

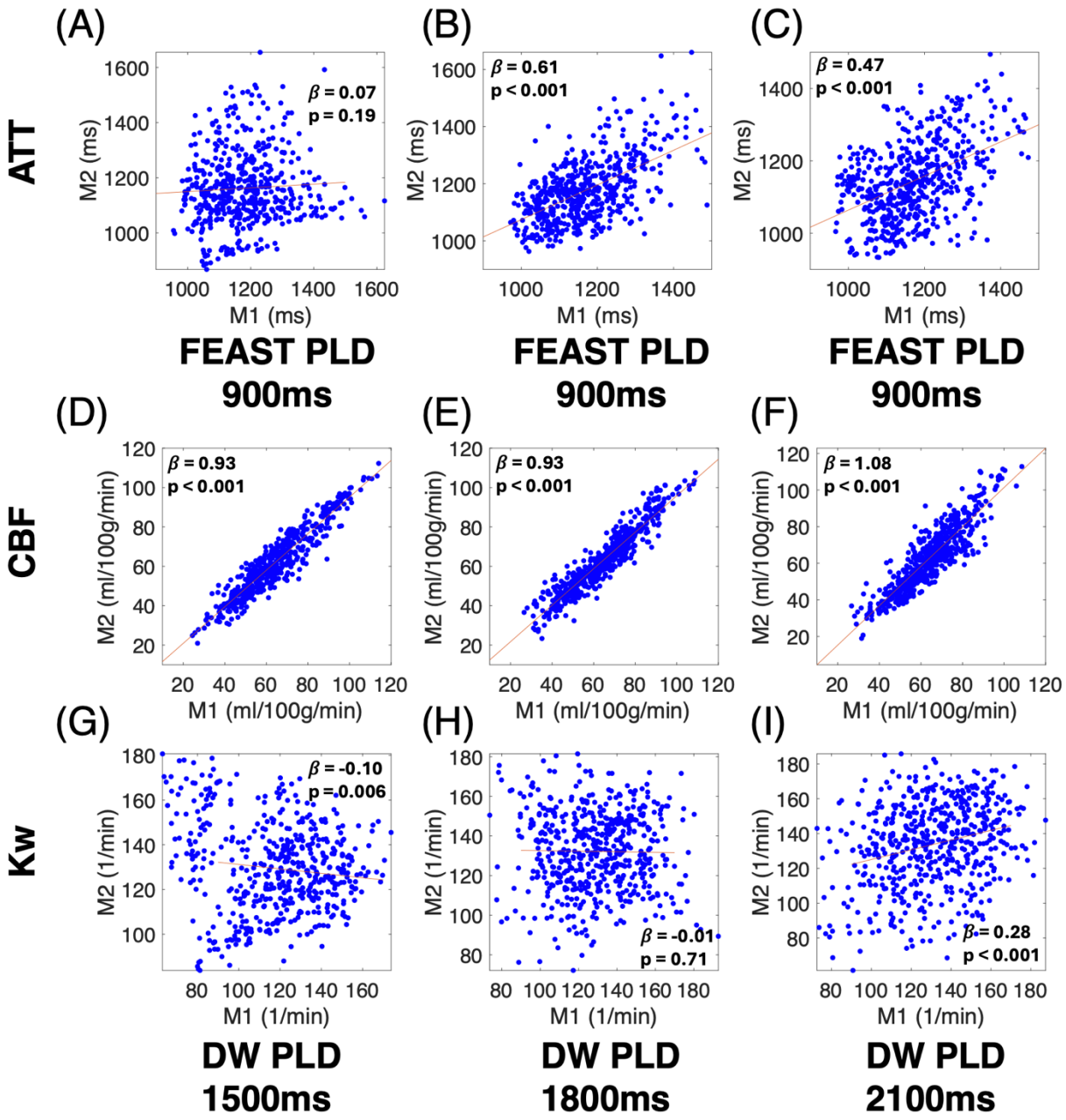

Supplemental Figure 4.2: Individual participant level gray matter Freesurfer region of interest (ROI) analysis of CBF, ATT, and Kw between measurement 1 (M1) and measurement 2 (M2). Only regions with 60% or greater voxel coverage were included. Mixed effect linear regression was performed with the participant as the random effect. Each point represents an ROI in the right or left hemisphere of the brain.

Furthermore, 3D cortical maps showing Kw averaged across the 10 participants were created by overlaying the 35 Freesurfer ROIs onto a structural brain image in MNI space as seen in Figure 4.4. We also included individual Kw maps in MNI space for three participants at DW PLDs 1500ms, 1800ms, and 2100ms, which is presented in Supplemental Figures 4.3-4.5. All cortical renderings were performed using MRIcroGL. [122]

4.3.4 Statistical Methods

Mixed effect linear regression with Freesurfer ROIs set as the random effect was used to assess the repeatability of M1 and M2 ATT, CBF, and Kw measurements. The average within-subject coefficient of variation (CV) between M1 and M2 was calculated for the four major brain lobes and reported to assess the variability of the measurements between scans. The intraclass correlation coefficient (ICC) was also calculated between intrasession Kw measurements. The slope (β) and p-value was reported along with the line of best fit. An F-test and T-test to compare the variances and mean, respectively, of two samples was performed to assess the difference between the FreeSurfer gray matter Kw distribution between M1 and M2. Normal distribution was assumed.

4.4 Results

4.4.1 Numerical Simulation

Figure 4.3 shows the simulation results that test the accuracy of the model fits in the presence of white Gaussian noise at three different Kw and PLD values, and at a range of physiologic and extreme ATTs. Panels A-F show the two-compartment model's fitting performance at Kw of $80min^{-1}$ and $140min^{-1}$, values reflective of typical physiological states, and suggests that the fitting protocol had sufficient performance (error <10%) at ATT range of around 1000ms to 2000ms in healthy adults. [123] Panels G-I extend the simulation to examine fitting protocol at a faster Kw of $200min^{-1}$. Here, the error rates increased beyond 10% at extremely long ATTs and there was prominent bias at lower ATTs at a PLD of 2100ms.

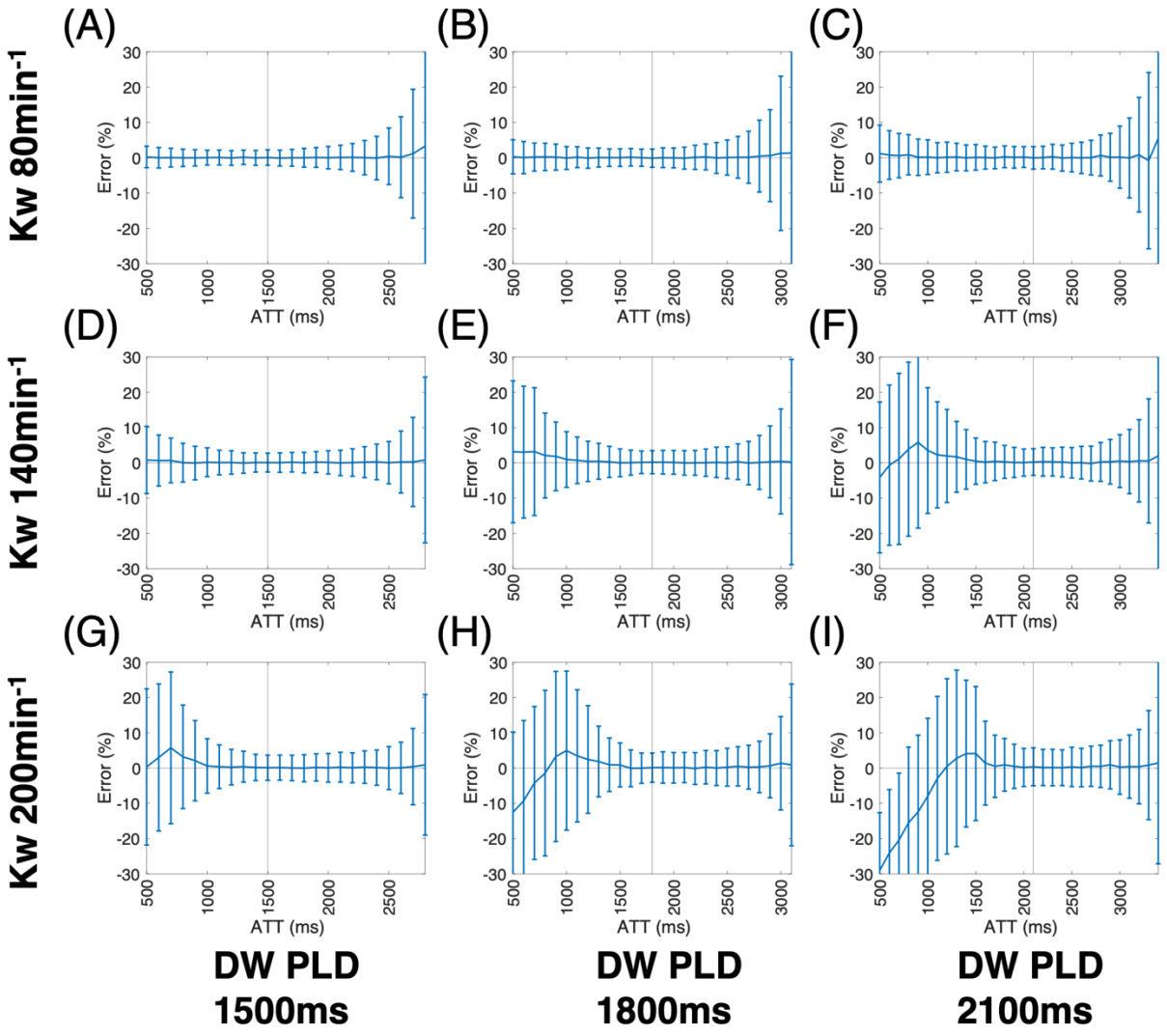

Figure 4.3: Single voxel Monte Carlo simulation showing percent error of fit at a range of arterial transit times (ATT). The vertical line depicts the post-label delay time (PLD) and separates sampling at the descending (left) and ascending portions (right) of the kinetic curve.

4.4.2 *In Vivo* Analysis

FEAST PLD	**900msec**		**900msec**		**900msec**	
ATT (sec)	**M1**	1.20 ± 0.10	**M1**	1.19 ± 0.07	**M1**	1.18 ± 0.06
	M2	1.18 ± 0.11	**M2**	1.20 ± 0.09	**M2**	1.16 ± 0.08
DW PLD	**1500msec**		**1800msec**		**2100msec**	
CBF (ml/100g/min)	**M1**	58.2 ± 13	**M1**	59.9 ± 13	**M1**	59.9 ± 10
	M2	55.7 ± 12	**M2**	57.8 ± 12	**M2**	58.1 ± 14
Kw (min^{-1})	**M1**	115 ± 24	**M1**	128 ± 17	**M1**	127 ± 13
	M2	129 ± 19	**M2**	133 ± 11	**M2**	132 ± 17

Table 4.1: Whole-brain averages of ATT, CBF, and Kw measurements across ten young, healthy participants.

Table 4.1 shows the whole brain average value for ATT, CBF, and Kw. For whole brain Kw, the PLDs of 1800ms and 2100ms showed the most consistent measurement at M1:128 ± 17min^{-1} versus M2: 133 ± 11min^{-1} and M1: 127 ± 13min^{-1} versus M2: 132 ± 17min^{-1}, respectively. Table 4.2 shows the within-subject coefficient of variation (CV) between Kw M1 and M2 where DW PLD of 1500ms exhibited the highest CV = 0.15 as compared to DW PLDs of 1800ms and 2100ms that had CV = 0.10 and CV = 0.08, respectively, across the four major brain lobes.

	Frontal	Parietal	Temporal	Occipital
1500msec	0.14	0.15	0.16	0.15
1800msec	0.07	0.09	0.10	0.13
2100msec	0.06	0.09	0.08	0.09

Table 4.2: Within-subject coefficient of variation (CV) between Kw measurements 1 (M1) and 2 (M2) for the four major lobes of the brain averaged across ten participants.

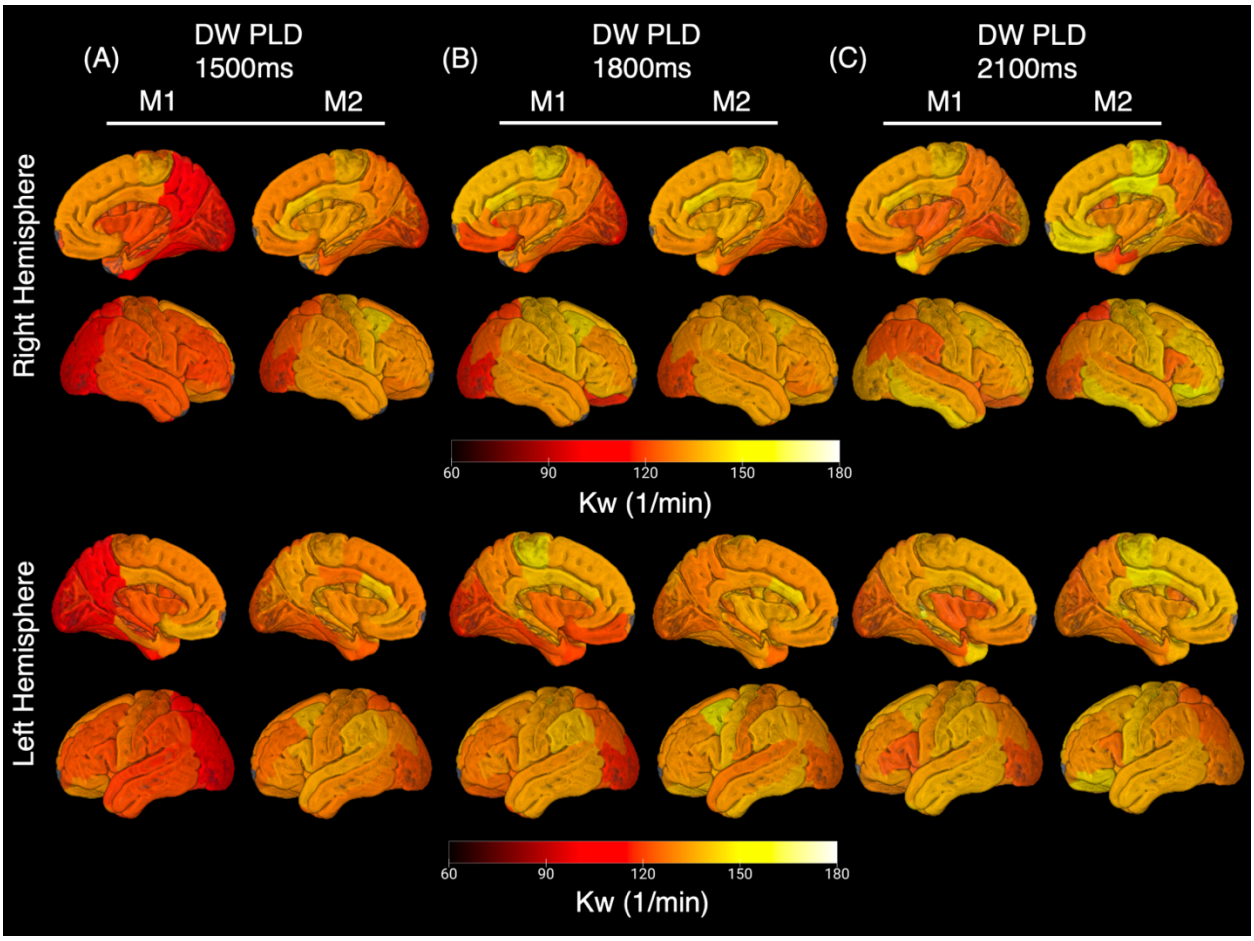

Figure 4.4: Cortical Kw representation at a post-label delay (PLD) of **(A)** 1500ms, **(B)** 1800ms, and **(C)** 2100ms between measurements 1 (M1) and 2 (M2). Each Freesurfer brain region represents the average across all participants with at least 60% voxel coverage. The underlying structural image is in MNI space.

Figure 4.4 shows cortical representations of FreeSurfer regional gray matter Kw values. Each region contains the mean Kw across all participants for regions that meet the 60% or greater voxel coverage criterion. Across PLDs, a consistent pattern of Kw distribution was apparent, with consistently low Kw values at the posterior end of the brain and the occipital lobe showing the lowest Kw at all PLDs. Specifically, at a PLD of 1800ms, voxels associated with the right and left frontal, parietal, and temporal lobes had average Kw values of $133.4 \pm 14.2 min^{-1}$, $128.1 \pm 16.2 min^{-1}$, and $130.4 \pm 18.5 min^{-1}$, respectively, compared to an average Kw of $115.4 \pm 18.5 min^{-1}$ ($p < 0.001$) in voxels of the occipital lobe. Visual consistency between intrasession measurements (M1 and M2) was strongest at PLD 1800ms and

the Kw maps appeared most similar between 1800ms and 2100ms across PLDs. Averaged Kw values for each Freesurfer region between M1 and M2 are provided in Supplemental Table 4.1.

Region	1500ms (min^{-1})		1800ms (min^{-1})		2100ms (min^{-1})	
	LH	RH	LH	RH	LH	RH
Banks of the superior temporal sulcus (1)(T)	126.2	126.0	138.9	139.9	150.2	137.5
Caudal anterior cingulate gyrus (2)(F)	135.6	136.3	141.6	144.4	141.1	140.7
Caudal middle frontal gyrus (3)(F)	128.7	131.7	139.9	142.9	138.0	137.7
Cuneus (5)(O)	122.5	120.5	121.7	121.6	123.1	122.3
Entorhinal cortex (6)(T)	127.2	123.2	127.0	128.2	124.8	124.2
Fusiform gyrus (7)(T)	116.2	114.8	125.6	120.1	128.5	131.3
Inferior parietal lobule (8)(P)	118.5	116.0	127.2	126.1	125.1	124.3
Inferior temporal gyrus (9)(T)	122.1	125.2	136.1	132.7	136.4	143.1
Isthmus of the cingulate gyrus (10)(T)	119.3	120.2	131.8	130.6	136.1	131.0
Lateral occipital cortex (11)(O)	112.4	111.1	117.7	114.2	122.7	127.8
Lateral orbitofrontal cortex (12)(F)	129.3	127.2	130.0	123.9	136.0	130.9
Lingual gyrus (13)(O)	116.4	116.2	121.9	121.3	126.0	122.5
Medial orbitofrontal cortex (14)(F)	132.6	128.3	124.2	123.8	131.3	136.6
Middle temporal gyrus (15)(T)	123.5	125.6	133.0	133.8	136.8	135.8
Parahippocampal gyrus (16)(T)	123.6	120.4	123.6	125.4	121.3	129.4
Paracentral lobule (17)(F/P)	129.1	136.7	138.3	142.8	140.5	146.0
Opercular part of inferior frontal gyrus (18)(F)	126.4	126.3	130.9	135.1	122.2	126.9
Pars orbitalis (19)(F)	128.7	124.4	128.6	131.5	138.3	138.7
Pars triangularis (20)(F)	124.4	122.9	130.6	132.3	125.2	130.5
Pericalcarine cortex (21)(O)	118.6	113.3	122.7	117.2	123.5	123.6
Postcentral gyrus (22)(P)	124.8	125.5	130.5	136.0	136.5	136.4
Posterior cingulate cortex (23)(P)	128.0	132.6	136.2	138.5	142.3	143.7
Precentral gyrus (24)(F)	127.3	128.7	136.2	136.0	134.7	137.8
Precuneus (25)(P)	120.6	115.9	127.8	130.5	130.4	124.1
Rostral anterior cingulate cortex (26)(F)	131.3	133.8	132.0	132.8	135.1	137.2
Rostral middle frontal cortex (27)(F)	121.0	123.3	128.6	131.8	129.6	138.8
Superior frontal gyrus (28)(F)	127.0	129.6	132.2	136.2	137.3	135.2
Superior parietal lobule (29)(P)	114.5	115.1	128.3	124.7	123.7	118.8
Superior temporal gyrus (30)(T)	124.4	125.9	128.6	131.1	134.2	127.6
Supra marginal gyrus (31)(P)	127.0	124.5	137.8	135.9	134.2	126.4
Frontal pole (32)(F)	NaN	NaN	NaN	NaN	NaN	NaN
Temporal pole (33)(T)	123.2	NaN	120.1	NaN	139.9	132.6
Transverse temporal gyrus (34)(T)	123.9	125.8	130.0	134.7	138.1	133.2
Insula (35)(n/a)	124.8	125.4	129.3	132.0	126.4	124.9

Supplemental Table 4.1: Average Kw values between measurement 1 (M1) and measurement 2 (M2) for left hemisphere (LH) and right hemisphere (RH) in 35 Freesurfer gray matter regions. (T), (F), (O), and (P) signifies the temporal, frontal, occipital, and parietal lobes of the brain. Not a number (NaN) values result from insufficient coverage, and that the corpus callosum region (4) was omitted because it is white matter.

Figure 4.5 depicts scatterplots of mixed effect linear regression between M1 and M2 with each point representing the average Kw within a FreeSurfer ROI across all participants that meet 60% threshold coverage. Panels A-C show three runs of ATT measurements that were all acquired at a FEAST PLD of 900ms. As expected, all three FEAST ATT measurements showed intrasession consistency with $\beta = 0.68$ ($p < 0.001$), $\beta = 0.84$ ($p < 0.001$) and $\beta = 0.71$ ($p < 0.001$). CBF also showed very high intrasession repeatability at PLD 1500ms, 1800ms, and 2100ms with $\beta = 0.89$ ($p < 0.001$), $\beta = 0.94$ ($p < 0.001$) and $\beta = 0.90$ ($p < 0.001$), respectively, while Kw only showed significant strong positive correlation at PLD of 1800ms with $\beta = 0.33$ ($p < 0.001$).

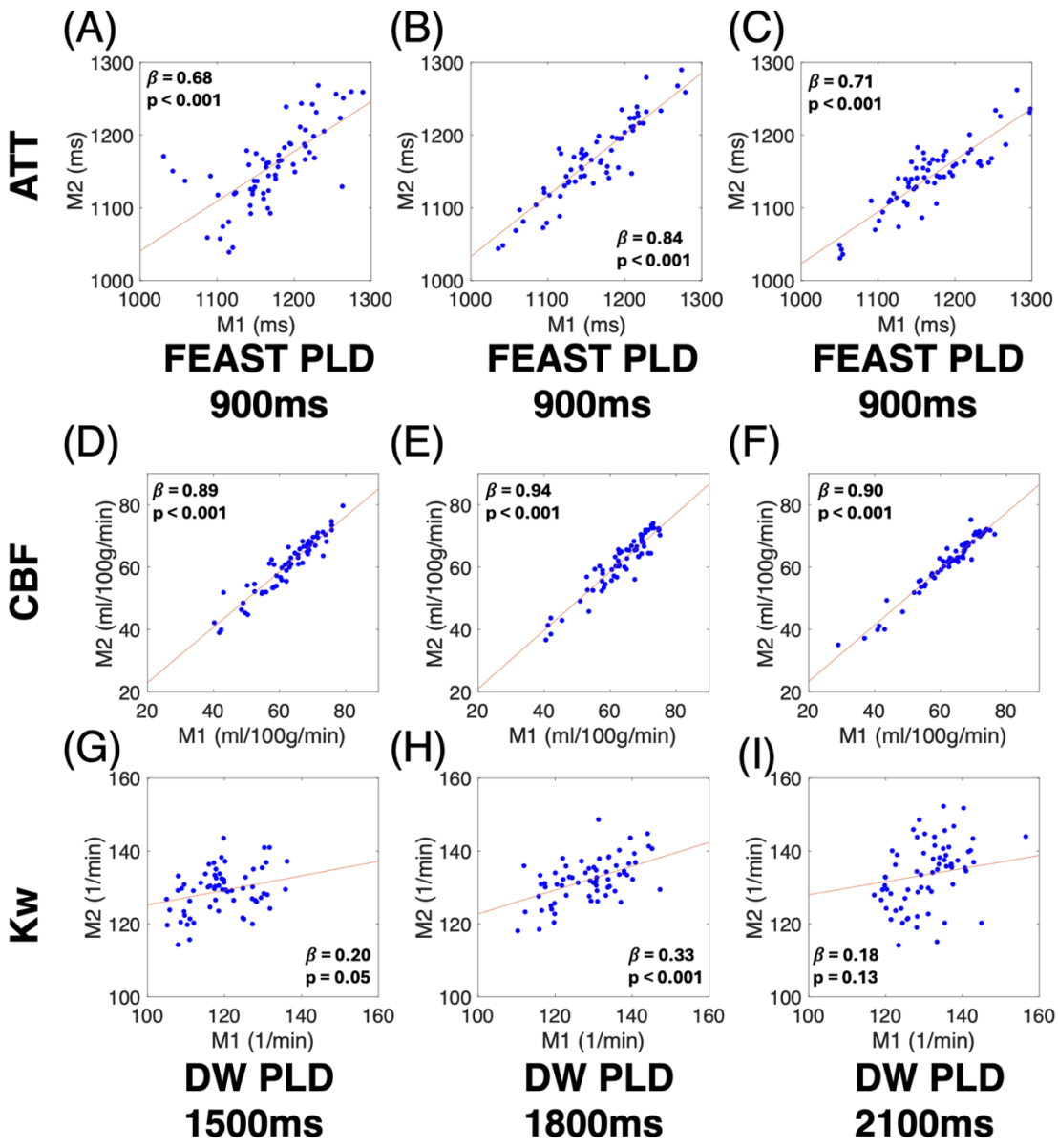

Figure 4.5: Gray matter Freesurfer region of interest (ROI) analysis of CBF, ATT, and Kw between measurement 1 (M1) and measurement 2 (M2). Only regions with 60% or greater voxel coverage were included. Mixed effect linear regression was performed with the participant as the random effect. Each point represents an ROI in the right or left hemisphere of the brain averaged across all ten participants. Coefficient of variation (CV) is reported as the within-subject CV (between the two repeat scans), averaged across participants and regions.

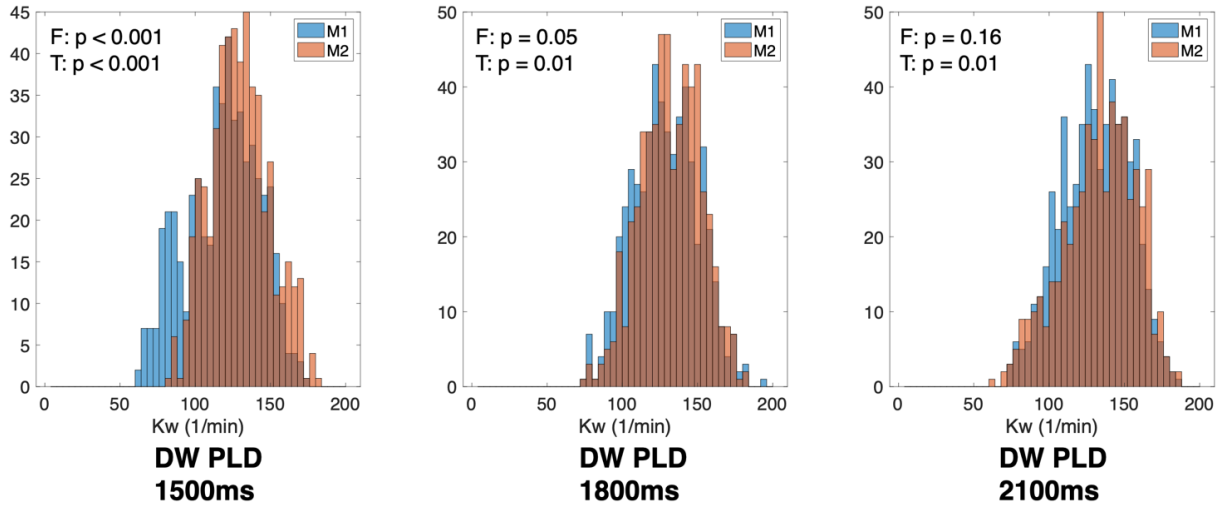

Figure 4.6: Gray matter Kw distribution for measurements 1 (M1) and 2 (M2) for ten individuals. Each count represents a gray matter region of interest (ROI). Only regions with 60% or greater voxel coverage were included.

Figure 4.6 shows the histograms of average Kw of all bilateral 35 FreeSurfer gray matter ROIs averaged across participants that meet the 60% voxel coverage threshold. F- and T-tests to assess differences in standard deviation and mean of the distributions, respectively, showed PLD 1800ms (F-test: $p = 0.09$, T-test: $p = 0.49$) and 2100ms (F-test: $p = 0.16$, T-test: $p = 0.01$) to produce the most similar Kw distribution between M1 and M2.

Figure 4.7 contains scatterplots of M2 results displaying Kw against (A)-(C) ATT and (D)-(F) CBF with each point representing a FreeSurfer gray matter ROI in the right or left hemisphere. For PLD 1500ms and 2100ms, a significant positive correlation was observed when a mixed effect linear regression model taking each FreeSurfer ROI as a random effect is fitted between Kw and CBF: ($\beta = 0.26$, $p = 0.005$) and ($\beta = 0.39$, $p < 0.006$), respectively. Additionally, a significant negative correlation was observed between Kw and ATT in PLDs 1500ms ($\beta = -0.04$, $p = 0.006$) and 2100ms ($\beta = -0.05$, $p = 0.006$).

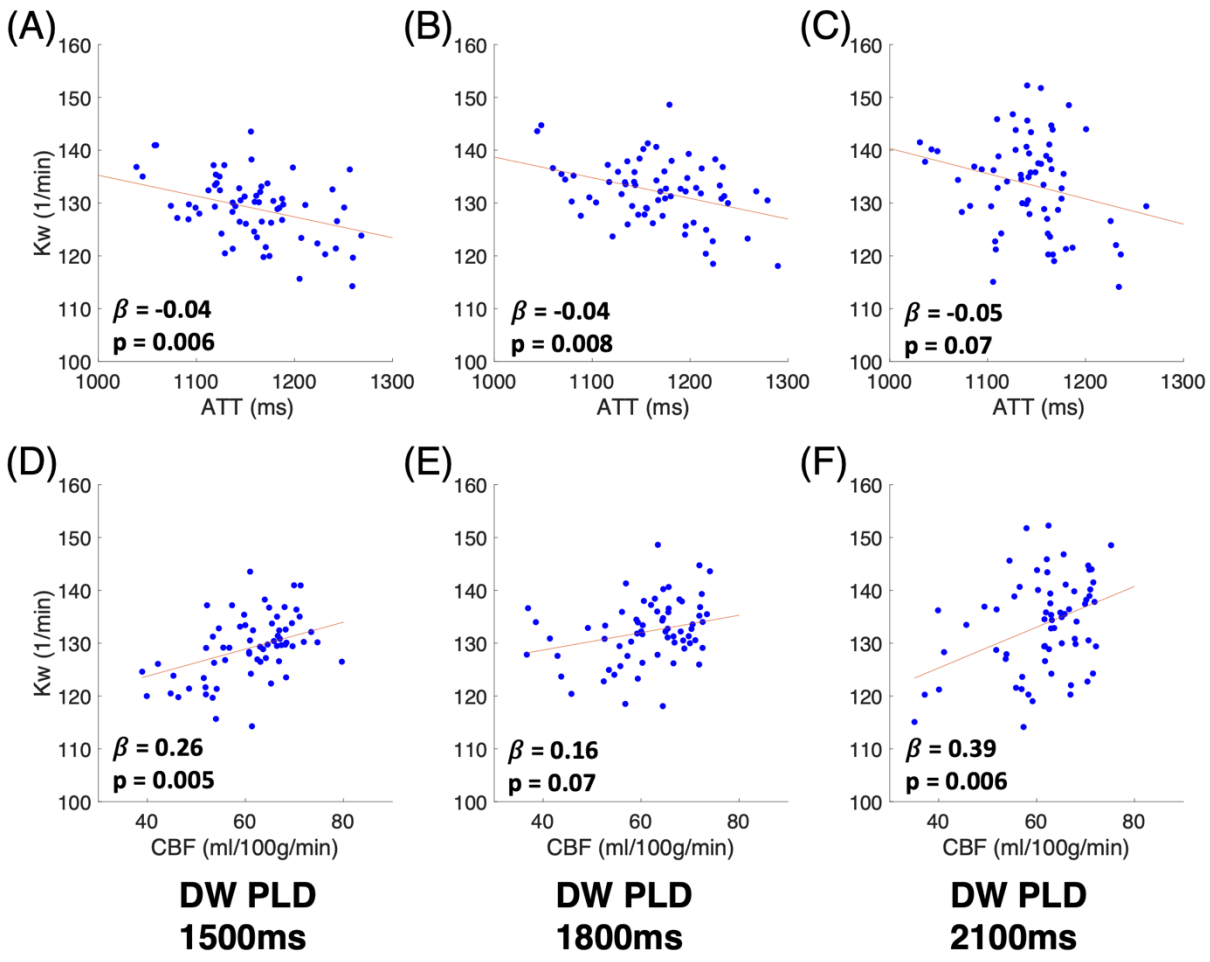

Figure 4.7: Correlation between water exchange rate (Kw) and arterial transit time (ATT) and cerebral blood flow (CBF) for all Freesurfer regions of interest (ROIs) in both brain hemispheres averaged across all participants for measurement 2 (M2). A mixed-effect linear regression model was performed between Kw and **(A)-(C)** ATT and **(D)-(F)** CBF with the participant as the random effect. Only regions with 60% or greater voxel coverage were included.

Supplemental Table 4.2 shows the result of the sensitivity study in four participants. At PLD of 500ms, the CBF was measured at an unphysiologically low value of 25.4 $\pm$ 5.5ml/100g/min while the Kw fitting failed in three participants (i.e. resulting in the default a maximum global Kw value of 200.min^{-1}) with one fitted at a particularly low average whole brain Kw value of 33.4min^{-1}. At a DW PLD of 3000ms, the average whole brain CBF and Kw values were fitted at 51.6 $\pm$ 4.3ml/100g/min and 129.9

± 13.6min^{-1}, respectively, which is consistent with the averages reported in the primary analysis (at 1500, 1800, and 2100ms DW PLDs).

	CBF (ml/100g/min)				
Post-Label Delay	**500msec**	**1500msec**	**1800msec**	**2100msec**	**3000msec**
Subject 1	27.9	57.6	59.9	58.7	55.3
Subject 2	22.1	51.7	54.3	54.1	46.6
Subject 3	31.8	62.3	69.2	65.6	55.0
Subject 4	19.6	51.7	58.9	62.1	49.3
Summary	25.4 ± 5.5	55.8 ± 5.1	60.6 ± 6.2	60.1 ± 4.9	51.6 ± 4.3
	Kw (min^{-1})				
Post-Label Delay	**500msec**	**1500msec**	**1800msec**	**2100msec**	**3000msec**
Subject 1	200.0	113.7	102.8	122.0	124.5
Subject 2	33.4	121.4	122.8	141.4	150.0
Subject 3	200.0	139.9	125.8	127.1	120.0
Subject 4	200.0	95.7	139.0	101.5	125.0
Summary	158.4 ± 83	117.7 ± 18	122.6 ± 15	123.0 ± 17	129.9 ± 13.6

Supplemental Table 4.2: Sensitivity analysis performed on four subjects at two extreme post-label delays (PLDs) of 500msec and 3000msec along with the original three PLDs of 1500msec, 1800msec, and 2100msec analyzed at a single measurement.

4.5 Discussion

Our findings confirmed that Kw was most stable between intrasession measurements at a DW PLD of 1800ms (Figure 4.5H). Further, there exists a significant positive correlation between CBF and Kw at DW PLDs of 1500ms (Figure 4.7D) and 1800ms (Figure 4.7F). Finally, regional Kw distribution

(Figure 4.4) showed the occipital lobe having the lowest Kw at 115.4min^{-1} compared to the other three major brain lobes, which collectively has an average Kw value of 130.6min^{-1}.

4.5.1 Numerical Simulation

In this work, we used simulations with Gaussian noise to investigate the effect different PLDs has on Kw fitting error within a single voxel at a range of ATTs. Simulation results (Figure 4.3) showed that there is reasonable fitting error (<10%) under physiological ATTs (1000-2000ms) at a Kw of 80min^{-1} and 140min^{-1} and PLD of 1500ms and 1800ms. Kw of 200min^{-1} at PLD 1500ms also fell within the normal error range. However, as the PLD and Kw increased to 2100ms and 200min^{-1}, respectively, the error increased beyond 10% at ATTs outside the physiological range. As a reference, Shao et al [20] reported normal whole brain average Kw in males to be 120.7 ± 17.4 min^{-1} in young, healthy male participants (age 8-35) and 97.9 ± 31.4 min^{-1} in an elderly male cohort (age 62-92). These results affirmed the robustness of the two-compartment model to estimate Kw under normal physiologic conditions but suggested that changes to the sequence parameters may be necessary for extreme cases where ATT is prolonged, such as in the elderly or certain patient populations. [104, 115]

In Figure 4.3, the Kw error was highest at an ATT of 500ms and then gradually decreased with increasing ATT. At shorter ATTs, sampling occurs along the descending portion of the ASL kinetic curve, and more time has passed before the prescribed PLD, leading to signal relaxation decay and lower SNR of the Kw measures (Figure 4.1A). This signal decay was exacerbated at high underlying Kw values (such as our simulations for Kw = 200min^{-1}) due to fast exchange, which results in low blood signal fraction (A_1) values. For high Kw rates, adding noise also causes A_1 to become negative (Supplemental Figure 4.1) in some instances, leading to poor or unreasonable model fits.

For ATTs longer than the PLD, the sampling occurs at the ascending portion of the kinetic curve, such that the sampled signal was lower and the simulated corresponding error also increases dramatically. In these scenarios, Kw estimates may face challenges, considering that the diffusion weighting gradient will not necessarily crush all the blood signal at a given PLD. [112, 113] A previous optimization study

showed that a sufficient fraction of the labeled spins needs to travel across the BBB into the tissue compartment so that, ideally, only roughly 15% of the signal originates from the blood component, ΔM_{bl}.

In participants with prolonged ATTs, such as the elderly or those with vascular abnormalities, it may be beneficial to choose a longer PLD more consistent with the lengthened ATTs, even though the overall signal amplitude would have decayed more when assessing BBB Kw. Previous work showed that long-delay ASL produces more accurate CBF measurements in a patient population with moyamoya disease whose vascular pathology lengthens the brain ATT values. [82] Similarly, in the elderly population, a PLD of 2-2.3 seconds was recommended to assess perfusion in the absence of ATT mapping. [115] Longer PLDs would maintain sampling at the descending portion of the kinetic curve when a substantial portion of the labeled spins has sufficient time to travel into the extravascular compartment.

4.5.2 *In Vivo* Findings

In our *in vivo* analysis between M1 and M2 of the average Kw in FreeSurfer gray matter ROIs, the PLD of 1800ms generated the most repeatable and consistent Kw measurements in young, healthy individuals compared to PLDs of 1500ms or 2100ms. Linear regression results (Figure 4.5) showed that Kw measurements at PLD 1800ms had the best overall consistency between M1 and M2 ($\beta = 0.33$, $p < 0.001$), though at PLD 1500ms ($\beta = 0.20$, $p = 0.05$) and 2100ms ($\beta = 0.18$, $p = 0.13$), the correlation was also positive, yet not significant. It should be noted that M1 of PLD 1500ms seems to be particularly low compared to M2, the latter of which is more consistent with the Kw cortical maps of the other PLDs. This may be due to an inherent limitation of selecting such a short PLD relative to estimated ATT of 1.3-1.4s in our cohort, such that some labeled water molecules may have remained in the large arteries, thereby violating the assumption of pseudo-random orientation of spins flowing in the capillary space. It should also be noted that the lower M1 distribution at PLD 1500ms is largely driven by 2 participants in the study who had unusually low Kw values throughout the brain, although these same 2 participants did not show the same discrepancies between M1 and M2 at longer PLDs.

Our results are an extension of the initial test-retest repeatability study performed by Shao et al. [113] in which 19 subjects were scanned approximately 6 weeks apart. There, the authors assessed the intraclass correlation coefficient (ICC) of whole brain measurements to be 0.74 as well as in eight different brain ROIs of varying sizes with ICC as high as 0.72 in the frontal lobe to ICC as low as 0.17 in smaller structures such as the parahippocampal gyrus. Unfortunately, our ICC calculations were not as consistent due to inherent variability between M1 and M2 average Kw values. Though we do see ICCs as high as 0.73 and 0.74 in the parietal lobes at DW PLDs of 1500ms and 2100ms, respectively, and an ICC of 0.76 in the occipital lobe at a DW PLD of 1500ms, these higher values are not replicable at a PLD of 1800ms or seen consistently across all other brain lobes of comparable size due to variations in average Kw values measured between M1 and M2. Moreover, these higher ICCs were calculated with the omission of two participants who showed extreme variability between M1 and M2 Kw values. These two participants, who were included in the CV calculations, contributed to the higher CV at PLD 1500ms (CV = 0.15) compared with PLD 1800ms (CV = 0.10) and 2100ms (CV = 0.08).

In cortical map representations (Figure 4.4), PLDs 1800ms and 2100ms also showed the most consistent intrasession Kw measurements as well as the most consistency between the PLD measurements. These Kw values are mostly consistent with the healthy participants of a recent study that found that Kw declines diffusely across the brain with age in the lateral and medial prefrontal cortices, anterior cingulate cortex, posterior cingulate cortex, temporal lobe, parietal lobe, occipital lobe, and insula. [20] However, we saw a relatively low Kw average in the occipital lobe in both the right and left hemisphere representations compared to the global brain average. At an average value of 115.4min^{-1}, this corresponds more to Kw values seen in typical older, middle age cohorts [107, 109] and, thus, may be the result of other contributions such as relatively longer transit time of the occipital lobe, which is supplied primarily by the relatively thin cortical branches of the posterior cerebral artery. [124] Additionally, we show in Figure 4.7 that Kw and ATT are negatively correlated to each other (i.e. longer ATT lower Kw). This is reasonable because perfusion has been shown to decrease with increased transit time. [115] Thus, regions with longer transit times are less perfused and do not possess the high enough systolic pressure to

drive water out across the BBB. The 130.6min^{-1} average Kw value of the frontal, parietal, and temporal lobes is slightly higher than the 120.7min^{-1} and 121. 7min^{-1} whole brain Kw averages reported in males and females, respectively by Shao et al. [20] This slight discrepancy could be due to a number of factors including the different tissue types begin compared, scanner variability, and sample size differences.

Moreover, in PLD 1500ms, we see that that M1 Kw appears to be diffusely low across all regions compared to M2, which is more consistent with measurements associated with PLD 1800ms but still lower in regions such as the left frontal cortex and the right parietal lobe. This abnormally low Kw is also apparent bilaterally in the parietal lobe of M2 at a PLD of 2100ms. Overall, these results suggest that a PLD of 1500ms may not be long enough to obtain consistent Kw measurements across individuals. As previously mentioned, two participants in the M1 PLD 1500ms group showed diffusely low Kw values throughout the brain. To summarize, distribution of bilateral FreeSurfer ROIs (Figure 4.6) exhibited the highest reproducibility at PLDs of 1800ms and 2100ms, which is consistent with the PLD used by the primary developer of the sequence [107, 113], though two studies [95, 108], one in participants with obstructive sleep apnea (OSA) and the other with schizophrenia, chose 1500ms as their PLD for studies performed on relatively younger subjects. In future studies, it may be valuable to apply this repeatability study on a group of elderly participants and assess the performance of this sequence at a PLD of 2100ms.

The sensitivity analysis performed in four participants evaluated DW-ASL maps at two extreme DW PLDs of 500ms and 3000ms. For the short PLD of 500ms, which is significantly lower than the average ATT in all 10 participants, there was insufficient amount of signal in the brain to adequately fit CBF and Kw in most individuals. The uniformity of the Kw maps and the low corresponding perfusion estimates suggest that inadequate fraction of arterial labeled spins reached and exchanged with the capillary bed. However, in the other extreme, a PLD of 3000ms produced reliable CBF and Kw metrics that are consistent with those fitted at DW PLDs of 1500ms, 1800ms, and 2100ms. This observation suggests despite the reduced vascular signal contribution that is expected at very long PLD, the two-compartment model is suitable to measure a consistent “equilibrium” Kw. This is an important finding because it suggests that the use of longer PLDs to account for longer ATTs, such as those exhibited in

elderly participants or those with vascular abnormalities, is a practical option with this DW ASL sequence.

A significant positive relationship exists between CBF and Kw at a DW PLD of 1500ms (β = 0.26, p = 0.005) (Figure 4.7D) and 2100ms (β = 0.39, p = 0.006) (Figure 4.7F). This observation is physiologically reasonable because CBF is positively correlated with cerebral perfusion pressure (CPP), which is the difference between mean arterial blood pressure and intracranial pressure. [125] In other words, brain regions with high CBF also possess high systolic pressure that forms the pressure gradient which is responsible for increased blood flow. This high systolic pressure, also referred to as hydrostatic pressure in the Starling principle, is the driving force that pushes water and solutes out of the capillary into the interstitial fluid of the brain tissue. [126, 127] We were not able to find any studies looking at the relationship between CBF and Kw measured by DW ASL in the published literature for comparison. However, a recent 2025 study by Padrela et al. [21] did apply a general linear model (GLM) on time of exchange (Tex), as measured with multi-echo (ME) ASL, and CBF and also found a significant positive correlation. Recall that Tex is the multiplicative inverse of Kw. Given that the direction of change in water exchange rate with age is opposite between DW and ME ASL [111], it may not be surprising that the relationship between water exchange rate and CBF is also opposite. This discrepancy may warrant further investigation with both methods in the same individuals. Additionally, in our young cohort, there was a significant negative relationship between Kw and ATT at DW PLDs of 1500ms (β = -0.04, p = 0.006) and 1800ms (β = -0.04, p = 0.008). This is reasonable because it makes sense physiologically that longer ATTs correspond to lower CBF measurements, which further corresponds with lower Kw values.

In addition, multi-echo (ME) ASL is another noninvasive MRI method that takes advantage of the different transverse relaxation times (T2) between the blood and tissue to separate the overall signal into a blood and tissue component from which Kw can be estimated using the two-compartment model. [37, 52] Currently, there are few comparison studies in the literature that characterize the differences between these methods. Morgan et al. [111] recently compared DW- and ME-ASL water exchange

measures in two cohorts of participants: one greater than age 55 years and another between 45 and 65 years. In this study, the authors found a nearly 3-fold discrepancy between Kw values for DW and ME ASL at $106.6 \pm 19.7 min^{-1}$ and $306.8 \pm 71.7 min^{-1}$, respectively. These averages are consistent with what has been reported thus far in the separate literature for each sequence. We note that the DW-ASL estimate of $106.6 \pm 19.7 min^{-1}$ from Morgan et al. derives from a cohort of 30 participants (63.8 ± 10.4 years) and is much lower than the average value of $122.6 \pm 15 min^{-1}$ we observed in our younger cohort of 10 participants (26.2 ± 2.3 years). This Kw difference between our studies may reflect age-related decrease in Kw, especially after age of 62 years. [107] Moreover, a significant negative correlation was observed between the Kw measured with DW and ME ASL across participants, which points out an opposing direction of water exchange in aging. This is surprising given that these two methods are purportedly measuring the same physiological metric of Kw across the BBB. This discrepancy between the ASL techniques may reflect differences in modeling approach, such as how T2 relaxation effects (and potential oxygenation-related changes in aging that alter T2) and inter-compartment exchange are considered in each method. [111] For DW-ASL, the efficacy of vascular crushers (which are not used in the current ME ASL sequence) may also change with lower perfusion and aging, also contributing to discrepancy between the two approaches. Future comparison studies are warranted to study the performance of these two BBB ASL sequences in the same participants.

It is important to mention that our regional analysis was performed on a group level for each FreeSurfer gray matter ROI that has 60% or greater voxel coverage. This means that each point in Figure 4.5 and Figure 4.7 represents an average Kw for that ROI across multiple individuals. Analysis done on an individual basis are presented in Supplemental Figure 4.2. We did this to minimize noise and to focus on regional distribution of gray matter Kw values as well as to understand the relationship of those regional Kw values to local CBF and ATT. Our analysis thus highlights group-level regional Kw reliability for different brain regions for the first time. A group level ROI Kw average supports the type of

group comparisons being performed with BBB DW ASL sequence currently published in the literature. [95, 108]

4.5.3 Limitations

Our study has several limitations. First, given the difference in resolution between the FreeSurfer masks ($1 \times 1 \times 1$ mm^3) and the BBB Kw maps ($3.5 \times 3.5 \times 8$ mm^3), there is significant partial volume effect contributing to each ROI. This makes individual exploration, especially of small regions, unreliable. Second, our simulation did not apply the total generalized variation (TGV) regularization to Kw map fitting. This means that our voxel-level Kw fitting simulation does not fully reflect how the *in vivo* Kw maps were calculated through the Water Exchange Quantification Toolbox, which likely improved SNR of *in vivo* fits through shared ASL signal information from adjacent voxels but also may indirectly smooth the Kw maps. Third, our pilot study to test out this sequence involved a small sample size of ten young healthy adults within the same session, with a Kw range from ~100 to 150 min^{-1}. In future studies, it may be impactful to investigate the performance of DW ASL in a cohort with longer ATTs and across a more prolonged time to see if the repeatability of this sequence still holds at PLD 1800ms. Fourth, the DW ASL scan field-of-view fails to capture the entirety of the brain. In this study, we aligned the top of the prescription window with the superior part of the brain, meaning that inferior structures such as parts of the temporal lobe may have been excluded in larger brains. Finally, the two-compartment model may not be sufficient in estimating Kw as the bipolar gradients used to crush the intravascular signal is velocity-sensitive and blood within the micro-vessels move at such a slow speed that their signal may not be entirely crushed. This would affect the tissue fraction (A_1), thereby skewing the estimated Kw.

4.6 Conclusion

To conclude, diffusion weighted (DW) ASL MRI showed good intrasession repeatability in assessing blood-brain barrier (BBB) water exchange rate (Kw) across different brain regions in young

healthy adults at a post-label delay (PLD) of 1800ms compared to 1500ms and 2100ms. Further, our study suggests that there could be a positive correlation between CBF and Kw and a negative relationship between ATT and Kw. Cortical representations of different brain regions showed consistent, reproducible Kw measurements in major lobes of the brain between intrasession measurements with the occipital lobe having significantly lower Kw compared to the frontal, temporal, and parietal lobes. Simulation analysis demonstrated that the Kw fitting algorithm is robust to Gaussian noise at physiologic arterial transit times (ATTs) and Kw values. Future studies would explore the effects of different PLDs in cohorts with prolonged ATTs to examine this sequence's performance in elderly and diseased population.

4.7 Appendix

If we assume labeled blood arrive in a voxel at time ATT and that that bolus is saturated for a labeling duration of LD, the inflow function c, can be defined by:

$$c(t) = \begin{cases} 0 \\ \alpha \cdot e^{-tR1_{bl}} \\ 0 \end{cases} for \begin{cases} t < ATT \\ ATT < t < ATT + LD \\ t > ATT + LD \end{cases} \qquad [A4.1]$$

Where α is the labeling efficiency, $R1_{bl}$ is the longitudinal blood relaxation rate. The residue function governing the water exchange can be modeled as:

$$r_{exch}(t) = e^{-tK_w} \qquad [A4.2]$$

Where K_w is the water exchange rate. The magnetization relaxation functions are defined as:

$$m_{bl}(t) = e^{-t \cdot R1_{bl}} \qquad [A4.3]$$

$$m_{ex}(t) = e^{-t \cdot R1_{ex}} \qquad [A4.4]$$

With $R1_{ex}$ representing the longitudinal relaxation rate of the tissue. In this model, we can neglect outflow based on the assumptions that the extracellular compartment is much larger than the blood compartment and that the image acquisition time is on an order that is much shorter than the vascular transit time. Therefore:

$$r_{bl,out}(t) \equiv r_{ex,out}(t) \equiv 1 \qquad [A4.5]$$

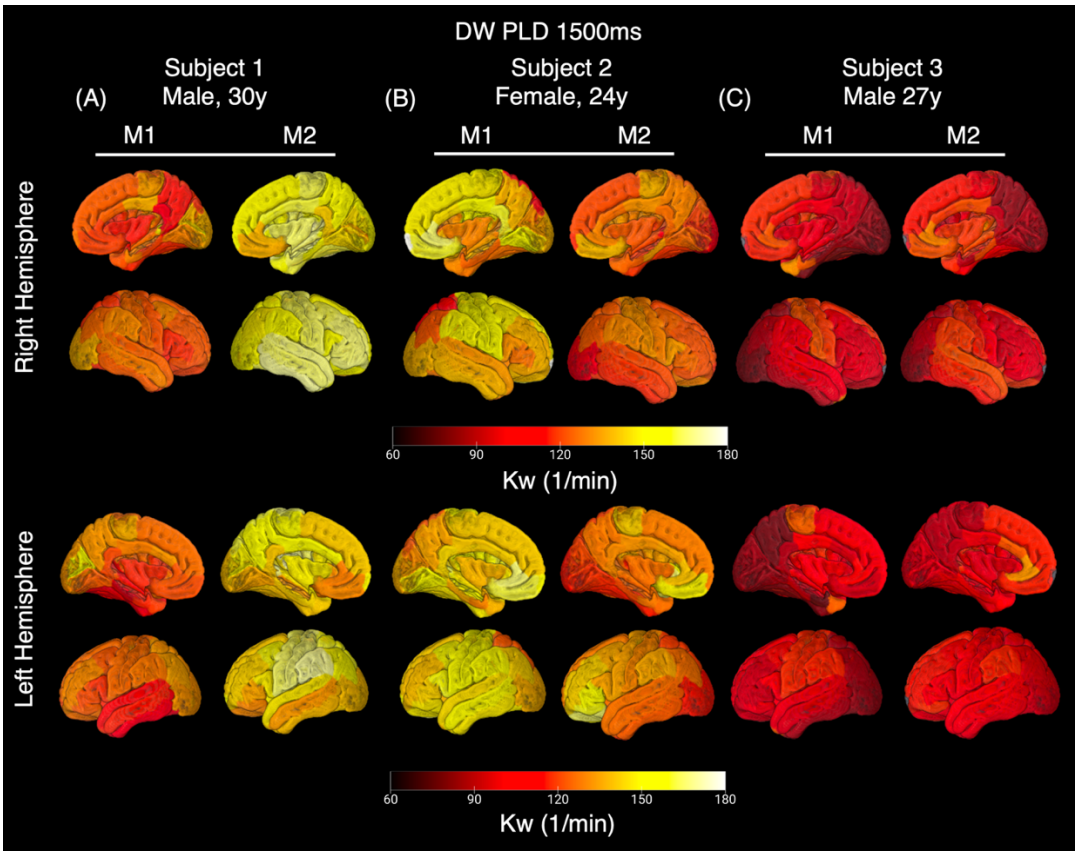

Supplemental Figure 4.3: Cortical Kw representation at a post-label delay (PLD) of 1500ms between measurements 1 (M1) and 2 (M2) for 3 individuals. The underlying structural image is in MNI space.

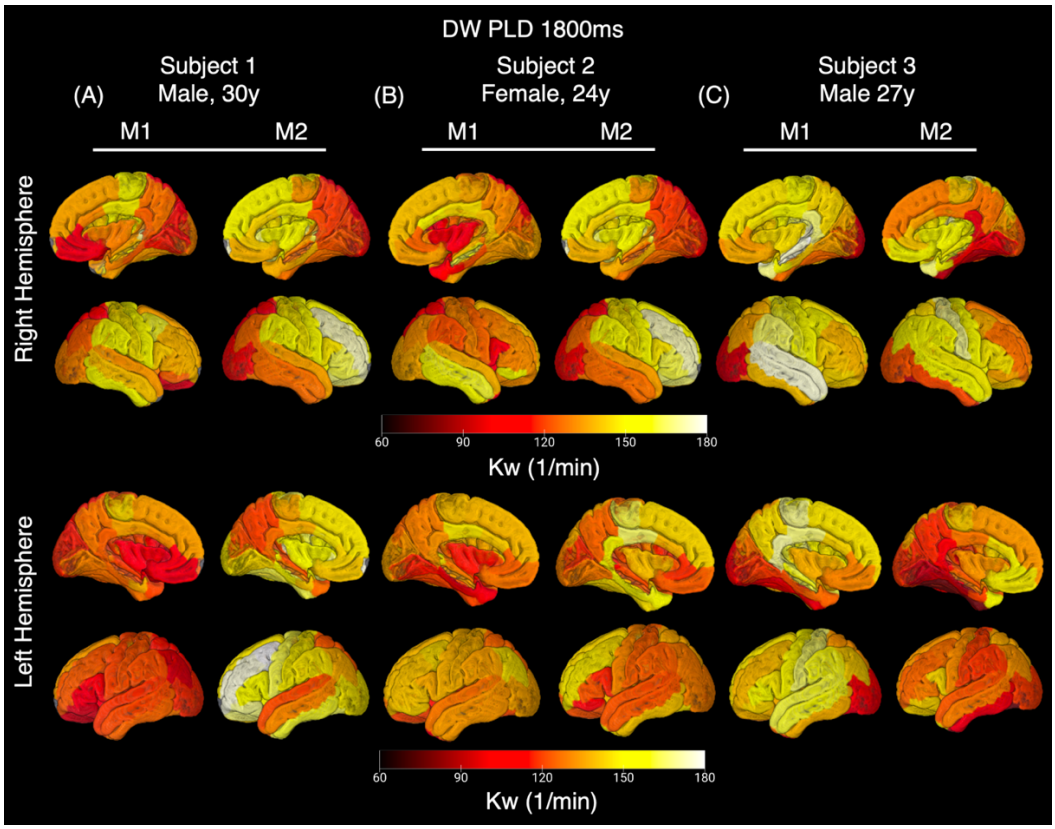

Supplemental Figure 4.4: Cortical Kw representation at a post-label delay (PLD) of 1800ms between measurements 1 (M1) and 2 (M2) for 3 individuals. The underlying structural image is in MNI space.

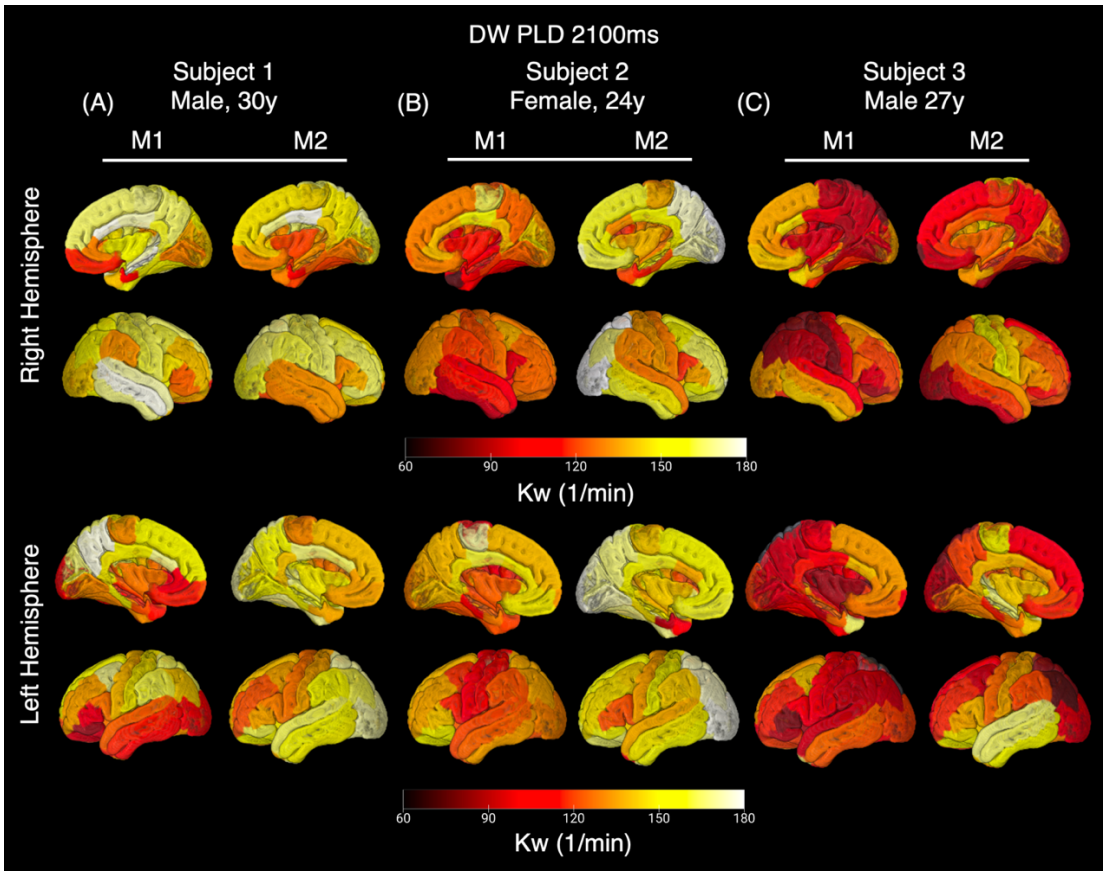

Supplemental Figure 4.5: Cortical Kw representation at a post-label delay (PLD) of 2100ms between measurements 1 (M1) and 2 (M2) for 3 individuals. The underlying structural image is in MNI space.

Chapter 5 Comparison of Water Exchange Rate in Young and Elderly Adults with Diffusion Weighted and Multi-Echo Arterial Spin Labeling MRI

5.1 Introduction

The blood-brain barrier (BBB) is a cellular structure that tightly controls the passage of water and molecules between the blood and tissue. [13, 128, 129] At the capillary level where exchange occurs, the BBB is comprised of vessels a single endothelial cell thick which are connected adjacently by tight junction proteins. [130] Pericyte cells reside in the perivascular space on the outer periphery of the capillary vessels and maintains the structural integrity of the BBB, regulates cerebral blood flow (CBF), and mediates immune responses while astrocytic endfeet further encases these structures and serves a critical role in the exchange of ions, metabolites, and energy substrates through the expression of transmembrane transporters. [131] Expression of transmembrane aquaporin (AQP) channels on endothelial cells and astrocytic endfeet serves to regulate the rate of water exchange across the BBB.

Altered BBB integrity and function, as assessed by the water exchange rate (Kw) using arterial spin labeling (ASL) MRI, has emerged as a potential biomarker for processes associated with aging and in diseases where the structural integrity of the neurovascular unit has been shown to deteriorate. [21, 95, 107, 132] The advantage of ASL is that this noninvasive, nonionizing, and contrast-free technique uses magnetically labeled water molecules as tracers to estimate Kw, a proxy measure for BBB integrity. [39, 40] These attributes make this method suitable for longitudinal studies that require repeat measurements as well as for scans involving younger participants where radiation exposure or contrast agent toxicity is a major concern. Kw is calculated through the theoretical two-compartment model, which mathematically splits the overall ASL kinetic curve into a vascular and extravascular component. [36, 37, 81] Kw is estimated voxel wise by fitting the two-compartment model to ASL scans acquired *in vivo* that employ different mechanisms to isolate the vascular and extravascular components of the signal.

Currently, two major ASL BBB sequences have promise in mapping Kw across the brain are the multi-echo (ME) and the diffusion-weighted (DW) ASL. [52, 112, 133, 134] ME ASL was first introduced by Gregori et al. [37] and models the different transverse relaxation times (T2) of the blood

and tissue across multiple echo times to split the overall ASL kinetic signal into an intravascular and extravascular component from which water exchange time (Tex)—the multiplicative inverse of Kw—can be estimated. DW ASL, on the other hand, takes advantage of the ~100-fold difference in pseudo diffusivity (D) between the two compartments and applies a bipolar diffusion gradient to crush the fast-flowing spins in the vasculature. While these techniques rely on different physical mechanisms to separate the intravascular and extravascular components of the overall ASL signal, both rely on the same two-compartment model theory to describe the exchange of labeled blood spins across the BBB and estimate Kw.

Interestingly, the effect of aging on water exchange rate between blood and tissue measured by ME ASL is in the opposite direction to that measure by DW ASL (i.e. ME detects increase while DW detects decrease). While the reason for this discrepancy remains unclear, it is hypothesized that the sequences may have differential sensitivity to various mechanisms through which water crosses the BBB. Investigations using DW ASL have shown that, Kw decreases across all brain regions except perhaps the occipital lobe because of both reduced and nonpolarized (i.e. away from the astrocytic endfeet) expression of AQP water channels. [4, 95, 108, 135] For studies using ME ASL, Kw has been found to increase with age across all the lobes, which may be attributed to breakdown of tight junction proteins that result in loss of BBB integrity and the more intense efflux of water from the vascular to the tissue space. [19, 132] While the aging-related changes in water exchange identified by ME ASL are more consistent with established, contrast-based methods of assessing BBB integrity, a recent study [136] using dynamic contrast enhanced (DCE) MRI and a three-compartment model showed reduced water exchange in patients with Alzheimer's Disease (AD) compared to healthy controls—more consistent with DW ASL. Thus, the debate regarding Kw directionality with age is ongoing.

Given this existing controversy in age-related Kw changes, there is a need for comparison studies that applies multiple techniques within the same set of participants to better understand this discrepancy. One recent comparison study by Morgan et al. showed an inverse relationship between water exchange measured by ME ASL versus DW ASL in the same older participants aged 45 to 82. [111] Here we

extend this work by directly comparing ME and DW ASL in two distinct age groups: a healthy young adult and a healthy elderly adult group. We also comprehensively compare regional Kw values across the two distinct age groups to better characterize how the spatial distribution changes with age between the ME and DW ASL BBB sequences.

5.2 Materials and Methods

5.2.1 Participants

12 young, healthy (aged 21-30, 8 female) and 18 elderly participants (aged 66-84, 13 female) underwent MRI scans on a 3T Magnetom Prisma (Siemens Healthineers, Erlangen, Germany). Young healthy participants were recruited from an institutional registry of study volunteers. Healthy elderly participants scans were recruited from the Alzheimer's Disease Research Center (ADRC) study registry at our institution. All elderly participants were evaluated to be cognitively normal within 12 months of the MRI through clinical evaluation by experienced neurologists and consensus case conference. All scans for this study were performed on a single scanner. This study was approved by the institutional review board and ethics committee at the University California, Davis and written informed consent was obtained from all participants.

5.2.2 Imaging Protocol

Structural scans, along with DW and ME ASL, were acquired from each participant (Figure 5.1). The order of the DW and ME ASL sequences was reversed in half the participants to account for ordinal bias. T1-weighted magnetization prepared rapid gradient echo sequence (MPRAGE) structural images [120] were acquired at resolution = $1.0 \times 1.0 \times 1.0$ mm^3 (scan time ~ 5min). Time of repetition (TR) was 2300ms, time to echo (TE) was 2.98ms and inversion time (TI) was 900ms.

(A)

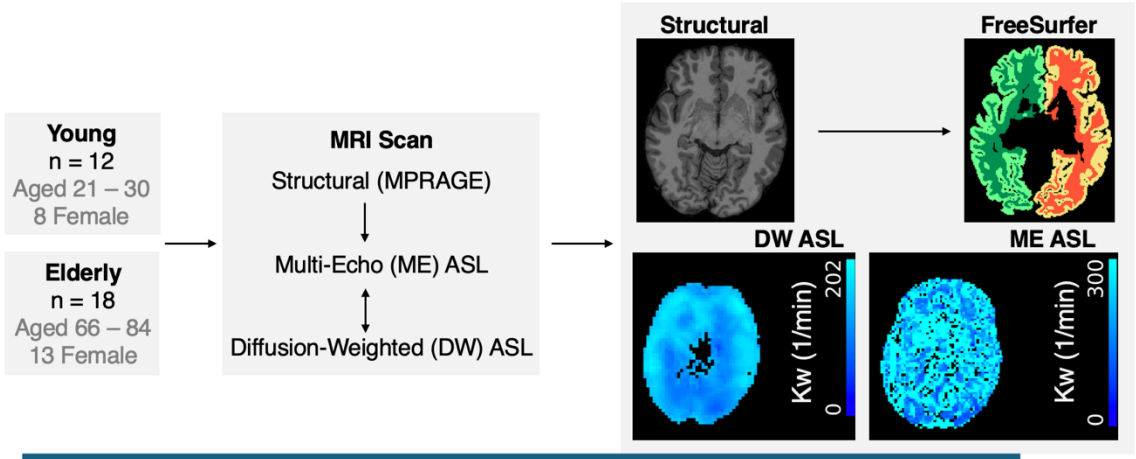

(B)

	Diffusion Weighted ASL	Multi-Echo ASL
Post-Label Delay	1800ms	Hadamard 4: [1600:1000:3600]ms Hadamard 8: [600:400:3000]ms
Labeling Duration	1500ms	Hadamard 4: 1000ms Hadamard 8: 400ms
Spatial Resolution	3.5mm x 3.5mm x 8mm	5mm x 5mm x 5mm
Readout	3D GRASE	Echo Planar Imaging (EPI) with CAIPIRINHA
Sequence Specific	FEAST: b = 14 s/mm^2 b = 50 s/mm^2	[14 42 70 98 126 154 182 210]ms

Figure 5.1: Scanning protocol. **(A)** Two cohorts of different age and sequence order where the multi-echo (ME) and diffusion-weighted (DW) sequences order is reversed in half the participants to account for ordinal bias. **(B)** important sequence parameters.

Diffusion-weighted (DW) ASL scans with 3D gradient-and-spin-echo (GRASE) readout were acquired to assess Kw with a DW post-label delay (PLD) of 1800ms. Furthermore, the DW ASL sequence was acquired at TR = 4s, TE = 36.5ms, FOV = 224mm, matrix size = 64 × 64, 12 slices (10% oversampling), resolution = 3.5 × 3.5 × 8 mm^3, label/control duration = 1500ms, and centric ordering. [110, 113] DW ASL scans included 20 repetitions with diffusion weightings (*b*-value) at 0 and 50s/mm^2 to measure Kw, which lasted ~6min. A flow encoding arterial spin tagging (FEAST) [47] acquisition to measure ATT was also incorporated into each DW ASL scan and was kept identical at a PLD of 900ms across all repetitions. The FEAST acquisition consisted of 15 repetitions at a diffusion weighting (*b*-value) of 0 and 14s/mm^2 with a total acquisition time of ~4min to estimate ATT. Therefore, the total time

for each DW ASL scan was ~10min. The center of the slice prescription was aligned with the center of the ventricles close to the pineal gland in the sagittal view so that as much of the brain could be covered as possible.

For the ME acquisition, a combination of single-TE and multi-TE Hadamard pseudo-continuous arterial spin labeling (PCASL) sequence with 3D GRASE readout was used. First, an M0 scan with TR = 5000ms, TE = 13.36ms, and scan time ~30sec was acquired for ASL signal calibration. This was repeated with reverse phase encoding direction for distortion correction. Next, a single TE, multi-TI Hadamard-8 encoded scan was acquired with a sub-bolus duration (SBD) of 1000ms and a PLD of 600ms (TE = 13.36, TR = 4190ms, turbo factor = 12, scan time ~ 2min30sec). The resulting two sets of seven inflow times (TI, where TI = SBD + PLD) ranged from 1600ms to 3000ms with increment of 200ms. Finally, a multi-TI, multi-TE scan was acquired using Hadamard-4 encoding with SBD = 1000ms and PLD = 500ms. These 3 TIs were 1500ms, 1700ms, and 1900ms collected at 200ms increments (TR = 4670ms, turbo factor = 2, scan time ~2min). Additionally, each TI was acquired at eight different echo times ranging from 14ms to 210ms with 20ms increments. All PCASL measurements were acquired with the in-plane field of view (FOV) = 320 × 160 mm^3, matrix size = 64 × 32 × 32, spatial resolution = 5 × 5 × 5 mm^3, EPI factor = 16, bandwidth = 2442Hz/Px, slice partial Fourier = 6/8, one pre-scan and an acceleration of 2 × 2 with CAIPIRINHA. [137]

5.2.3 Post-processing

We used the Water Exchange Quantification Toolbox (WEQT) for the DW ASL and the ExploreASL [138] for the ME ASL acquisitions to generate Kw and Tex maps, respectively. Regional Tex values were converted to Kw values to facilitate direct comparison. Raw ME ASL scans were Gaussian smoothed with an isotropic 10mm × 10mm × 10mm kernel before processing in ExploreASL. The smoothing sought to reduce the number of negative Tex values.

FSL was used to align the Kw maps for each of the ASL methods onto the structural image. FreeSurfer [18] was used to segment the structural image into 35 cortical gray matter regions bilaterally

for region of interest (ROI) analysis. Only gray matter ROIs with 70% voxel coverage in the ASL maps or greater for each individual. Right and left hemisphere gray matter Kw were averaged for each cortical region before statistical analysis. Cortical representations are of the average regional Kw in the young and elderly groups overlayed onto an MNI template. [139]

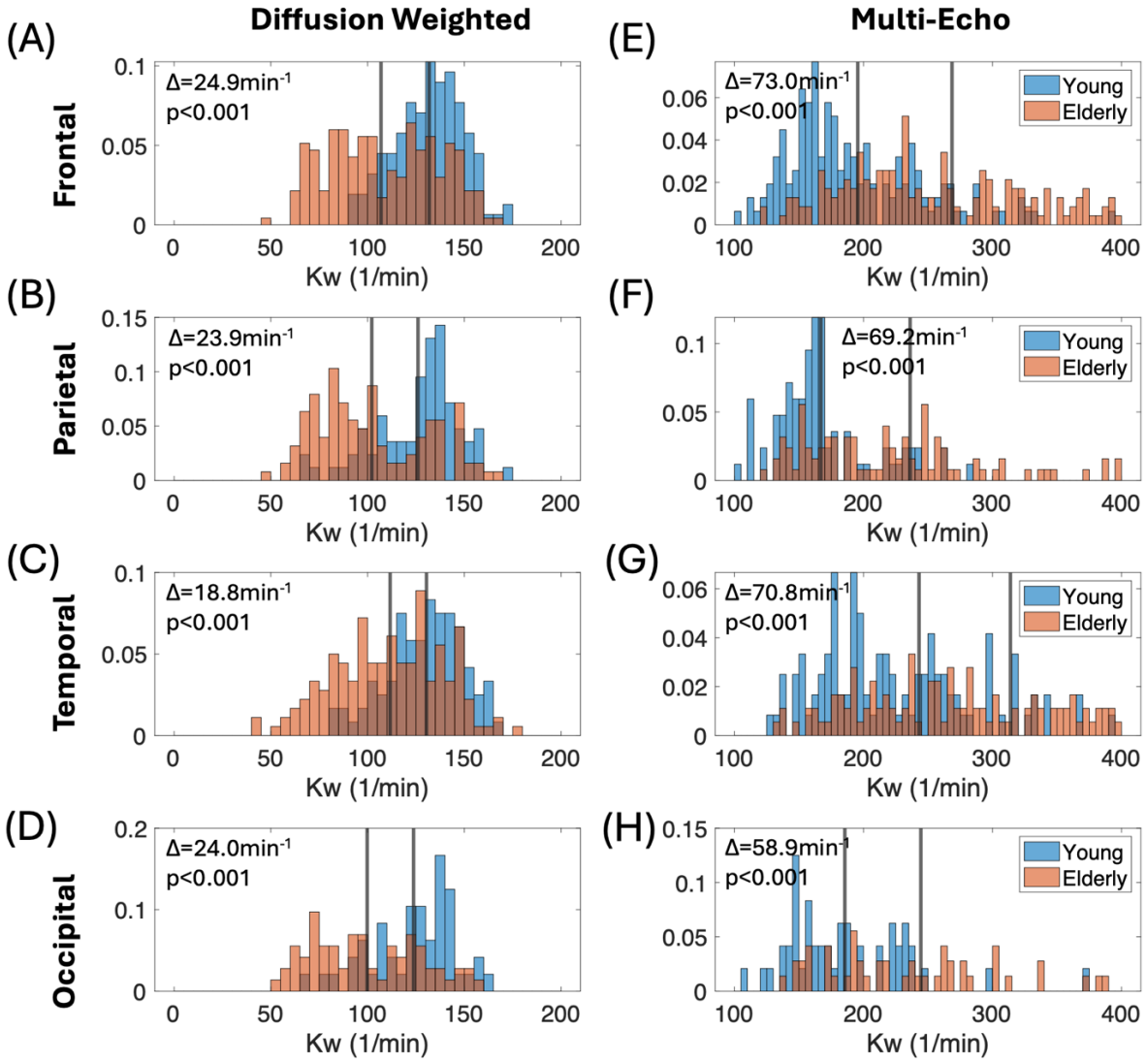

Figure 5.2: Kw differences between young and elderly. **(A)-(D)** Normalized distributions of 35 FreeSurfer cortical gray matter ROIs between old and young organized into the four major brain lobes for diffusion-weighted (DW) ASL. **(E)-(F)** The same normalized distributions for multi-echo (ME) ASL. P-value is that of the mixed effect linear regression model taking Kw as the dependent variable and the two

categorial groups (i.e. young and elderly) as the independent variable while setting participant as a random effect.

5.2.4 Statistics

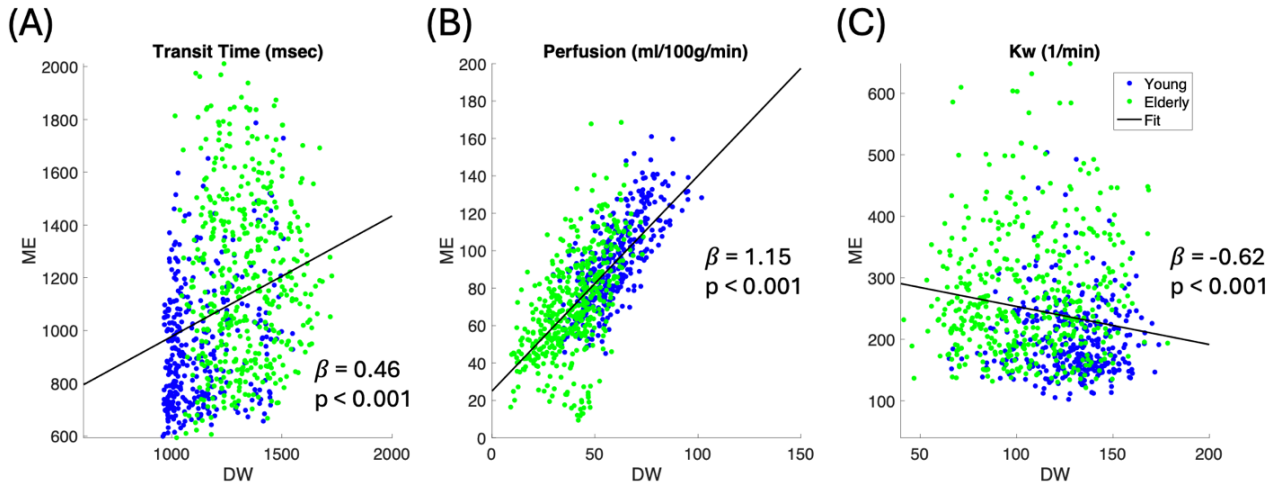

Figure 5.3: Mixed-effect linear regression between diffusion-weighted (DW) and multi-echo (ME) ASL sequences taking participant as the random effect for **(A)** arterial transit time, **(B)** cerebral perfusion, and **(C)** Kw.

To compare Kw values in younger and elderly groups, we used a separate mixed effect linear regression model for each of the four major brain lobes. In each model, Kw averaged across the lobe was the dependent variable and categorical group (i.e. young and elderly) was the independent variable, while setting participant as a random effect. Mixed effect linear regression was also used to plot transit time, perfusion and Kw measurements across the FreeSurfer gray matter regions taking the participants as a random effect in Figure 5.3. The slope, β, and p-value were reported. Additionally, average Kw values for each of the FreeSurfer cortical ROIs were projected onto a 3D cortical map in MNI space. A two-sample t-test between young and elderly average Kw was performed for each of the regions and a Benjamini Hochberg correction was performed to control the false discovery rate (FDR) for performing multiple tests.

5.3 Results

Figure 5.2 shows the normalized histogram representations of young and elderly average Kw values associated with FreeSurfer parcellation regions organized into the four major brain lobes. The vertical lines represent the mean of each distribution and the Δ represents the difference between the means of the two groups. Mixed effect linear regression accounting for the participants as the random effect showed the mean distributions were statistically different between young and elderly ($p < 0.001$) in all four lobes. Overall, DW ASL showed a Kw change of decreasing $\Delta = 22.9 min^{-1}$ with age while ME ASL had an increasing $\Delta = 68.0 min^{-1}$ across all lobes.

Figure 5.3 shows the mixed-effect linear regression models in the young and elderly cohorts directly comparing between the DW and ME ASL sequences for arterial transit time (ATT), cerebral blood flow (CBF) and Kw. Each datapoint represents a FreeSurfer parcellated cortical gray matter region in one individual for all participants. ATT measurements between the two sequences showed a significant positive correlation ($\beta = 0.46$, $p < 0.001$) and CBF, also showed a strong positive correlation in ($\beta = 1.15$, $p < 0.001$) between the two sequences. For Kw, however, there was a negative correlation between DW and ME ASL ($\beta = -0.62$, $p < 0.001$).

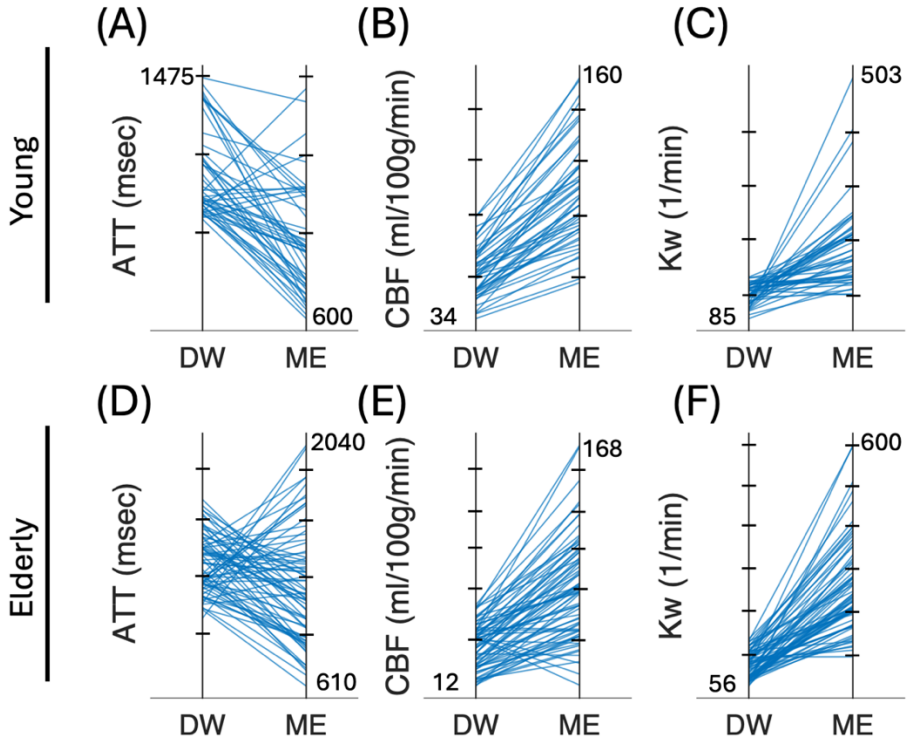

Figure 5.4: Parallel plots of arterial transit time (ATT), cerebral blood flow (CBF), and Kw values between diffusion-weighted (DW) and multi-echo (ME) ASL. Note that the data is displayed on coordinate rulers that have the same minimum and maximum limits.

Figure 5.4 shows parallel plots for arterial transit time (ATT), cerebral blood flow (CBF), and Kw measurements between the DW and ME ASL sequences. Each datapoint corresponds to an average value in one of the four major lobes of the brain (i.e. frontal, parietal, temporal, occipital) from one participant. Overall, results show ME ASL estimated higher CBF and Kw values compared to DW ASL, and an ATT range for ME ASL that was wider than that for DW ASL.

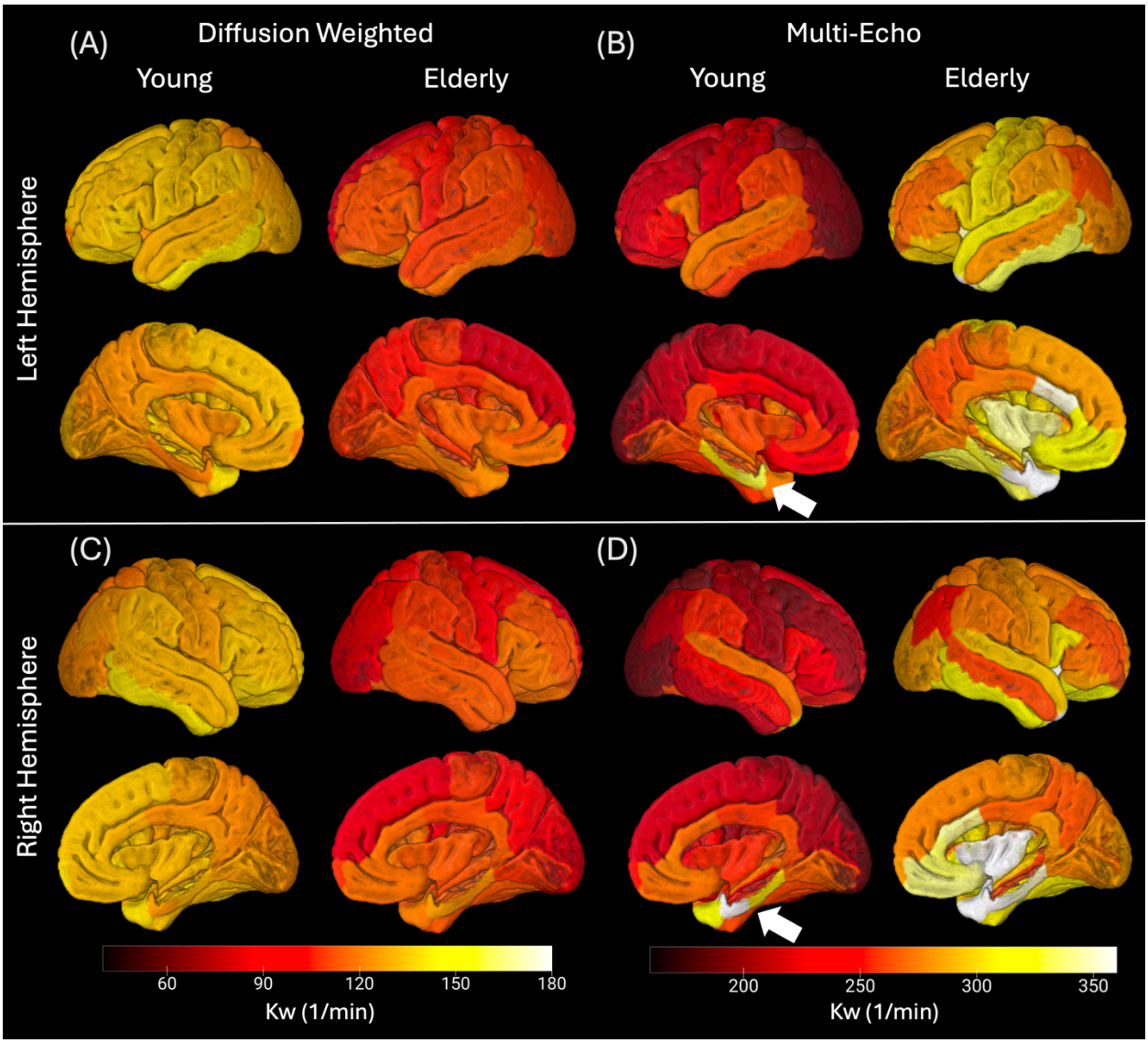

Figure 5.5: Cortical representations in MNI space of average Kw across all participants in each cohort for each of the 35 cortical gray matter FreeSurfer regions between diffusion-weighted **(A)-(B)** (DW) and **(C)-(D)** multi-echo (ME) ASL. Notice that the entorhinal cortex (white arrow) is higher for the ME ASL technique in the young group.

Figure 5.5 shows the 3D cortical map representation of the Kw values averaged across all participants projected onto a standard brain map in MNI space. It is important to recognize that the Kw color bar Kw range for DW and ME are distinct so that direct comparison between cortical maps associated with each sequence is not possible. However, it is observable that the ME ASL Kw change

between elderly and young was more localized to the temporal lobe and with structures associated with aging and neurodegeneration. In contrast, the Kw change with DW ASL appeared more homogenous across all FreeSurfer brain regions. Supplemental Figure 5.5 depict similar cortical maps with the regional t-statistics comparing between young and old are plotted onto a 3D brain map in MNI space. Here we can better appreciate the regions that are changing most with age.

	DW		**ME**	
	Young	**Elderly**	**Young**	**Elderly**
ATT (sec)	1.14 ± 0.16	1.34 ± 0.15***	0.95 ± 0.23	1.20 ± 0.32***
CBF (ml/100g/min)	59.2 ± 13.6	38.0 ± 13.5***	92.0 ± 23.5	70.0 ± 27.5***
Kw (min^{-1})	128.8 ± 19.8	107.2 ± 28.5***	203.7 ± 68.7	274.7 ± 101.4***

*** $p < 0.001$

Table 5.1: Whole-brain average of arterial transit time (ATT), cerebral blood flow (CBF) and Kw for young and elderly cohorts with the diffusion-weighted (DW) and multi-echo (ME) ASL sequences. All elderly groups were statistically different from young groups.

Table 5.1 shows the whole brain average for ATT, CBF, and Kw calculated by averaging the average values for each parameter in all the FreeSurfer gray matter cortical regions. Both DW and ME ASL exhibited increased ATT and decreased CBF with age. Noncorrected t-statistics and associated p-values are presented in supplemental tables 1-2 for FreeSurfer ROIs in the right and left hemispheres.

To identify FreeSurfer regions that showed significant differences in Kw, Table 2 shows p-values for two sample t-tests between average Kw values in each of the FreeSurfer cortical gray matter regions for right (RH) and left hemispheres (LH). These p-values have been adjusted with the Benjamini Hochberg method to mitigate false discovery rates (FDR) associated with multiple tests. None of the regions for DW ASL survived FDR correction while for the ME ASL method, seven regions in the frontal lobe, four regions in the parietal and temporal lobe and two regions in the occipital lobe were statistically significant between young and old. The uncorrected t-statistics and p-values are reported in supplemental tables 1-2 for left and right hemispheres, respectively.

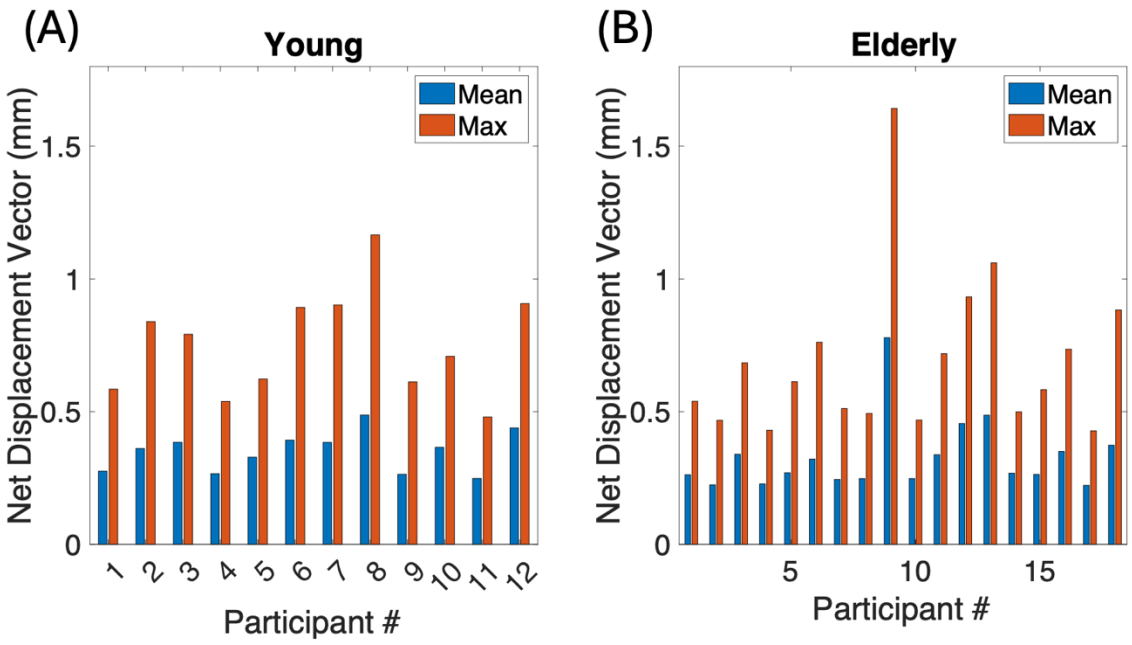

Supplemental Figure 5.1: Motion plots for individual multi-echo (ME) ASL scans as assessed with mean and max net displacement vector (NVD) that considers movement and rotation.

Supplemental Figure 5.1 is a summary assessment of how much each participant moved during the ME ASL sequence acquisition measured in net displacement vector (NDV), which has the units of millimeters (mm). NDV is a sequence measurement that considers the total movement and rotation of each frame relative to the first acquisition.

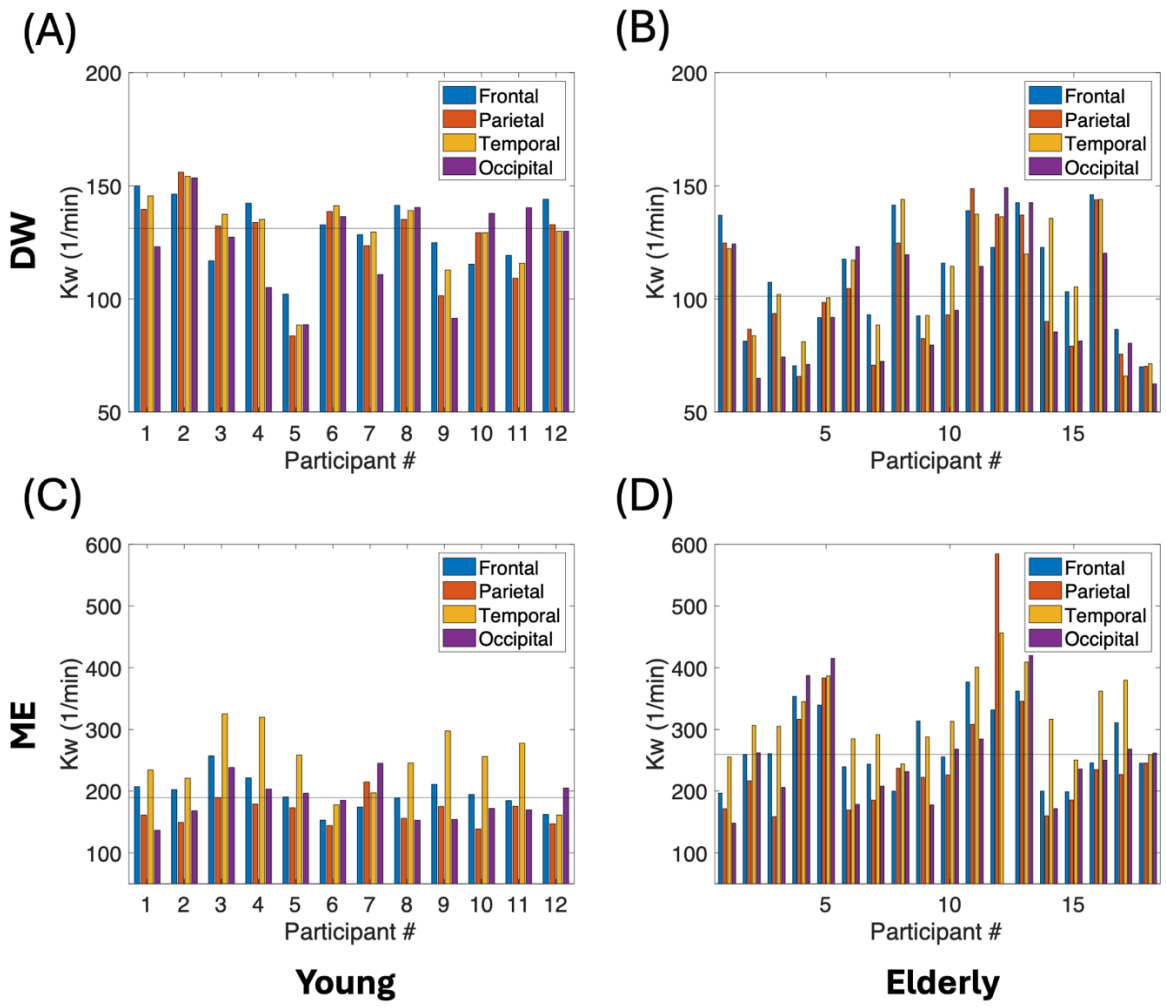

Supplemental Figure 5.2: Kw values within each lobe for each participant. **(A)-(B)** Individual average Kw values in the four major brain lobes for diffusion-weighted (DW) ASL between young and elderly participants. **(C)-(D)** The same individual average Kw values for multi-echo (ME) ASL.

Supplemental Figure 5.2 shows the average Kw value in each of the four major brain lobes for all the individual participants. The horizontal lines in these plots represent the median Kw for each cohort and sequence. For the young cohort, the median line for DW ASL is located at 131.2min^{-1} while for ME ASL, it is located at 189.3min^{-1}. For the elderly cohort, the median line for DW ASL is located at 101.2min^{-1} while for ME ASL, it is located at 259.3min^{-1}.

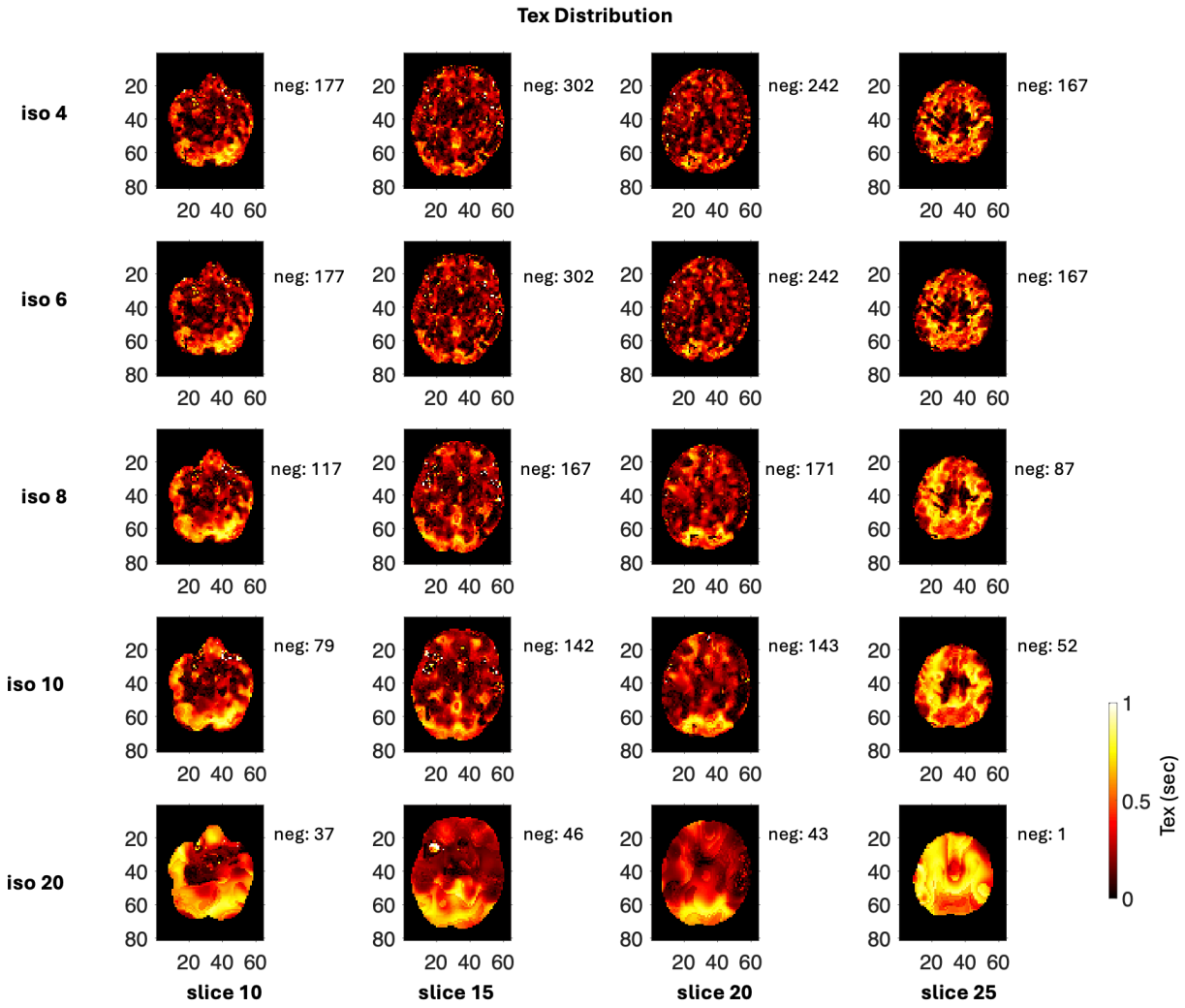

Supplemental Figure 5.3: Gaussian smoothing analysis. Axial view at four different slices of time of exchange (Tex) maps with Gaussian smoothing at five different isotropic kernel sizes for one healthy young participant. Also reported at the number of negative Tex (neg) values for each of the slices.

Supplemental Figures 5.3-5.4 show the analysis of the implementing an isotropic Gaussian smoothing kernel of different sizes (mm) to the ME ASL raw images. The number of negative (neg) time of exchange (Tex) values within each slide is reported alongside the corresponding image. Ultimately, a smoothing kernel of 10mm × 10mm × 10mm was used to mitigate the negative Tex values without overly disrupting the integrity of the nonsmoothed Tex distribution.

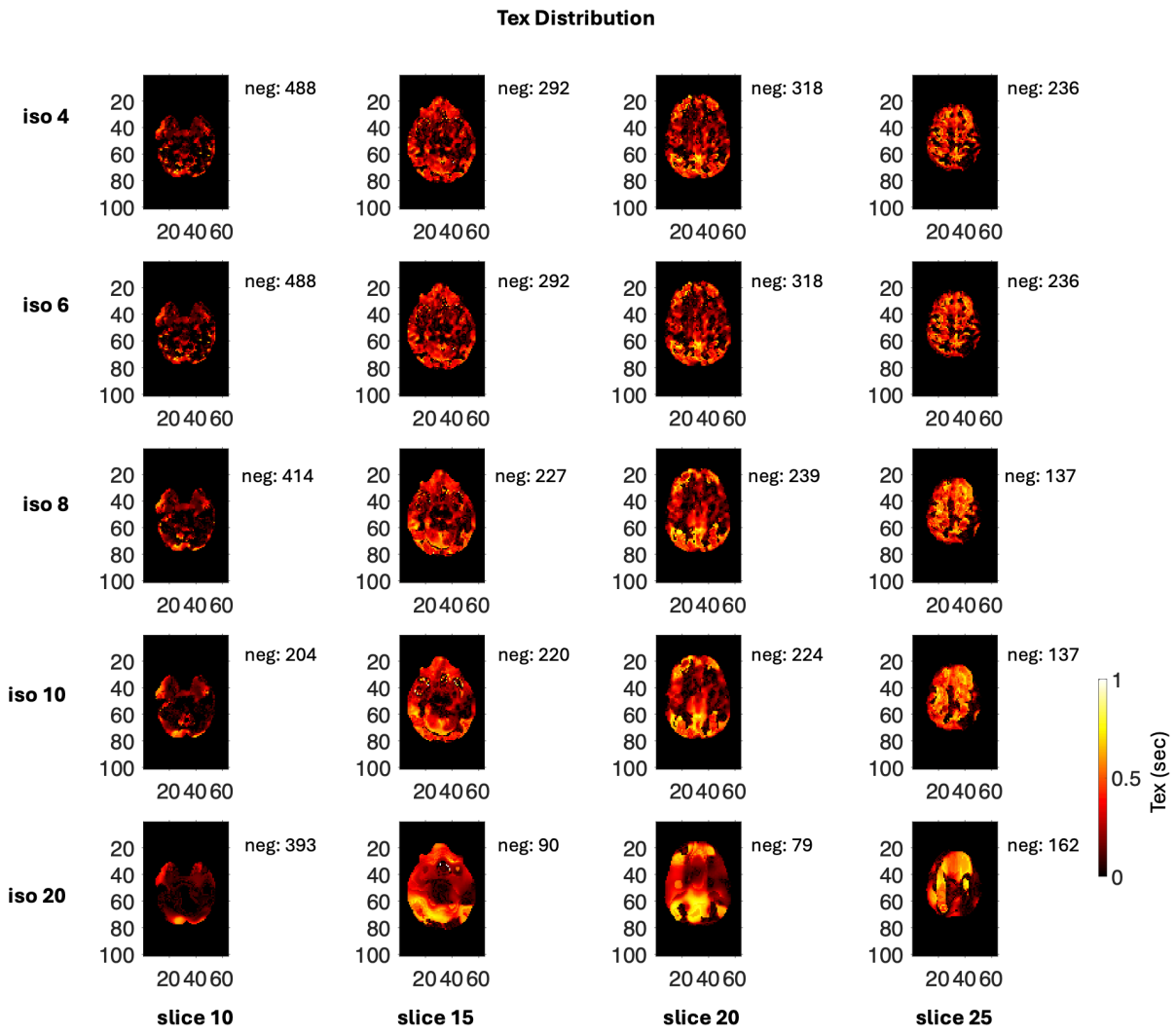

Supplemental Figure 5.4: Gaussian smoothing analysis. Axial view at four different slices of time of exchange (Tex) maps with Gaussian smoothing at five different isotropic kernel sizes for one healthy elderly participant. Also reported at the number of negative Tex (neg) values for each of the slices.

Supplemental Figure 5.3 is an extension of Figure 5.3 showing the mixed-effect linear regression plotted separately for young and elderly. Results show that linear regression between the two sequences for arterial transit time in the elderly and Kw in young and old all failed to reach statistical significance. This indicated that some of the trends observed in Figure 5.3 is driven by the age difference between the two cohorts.

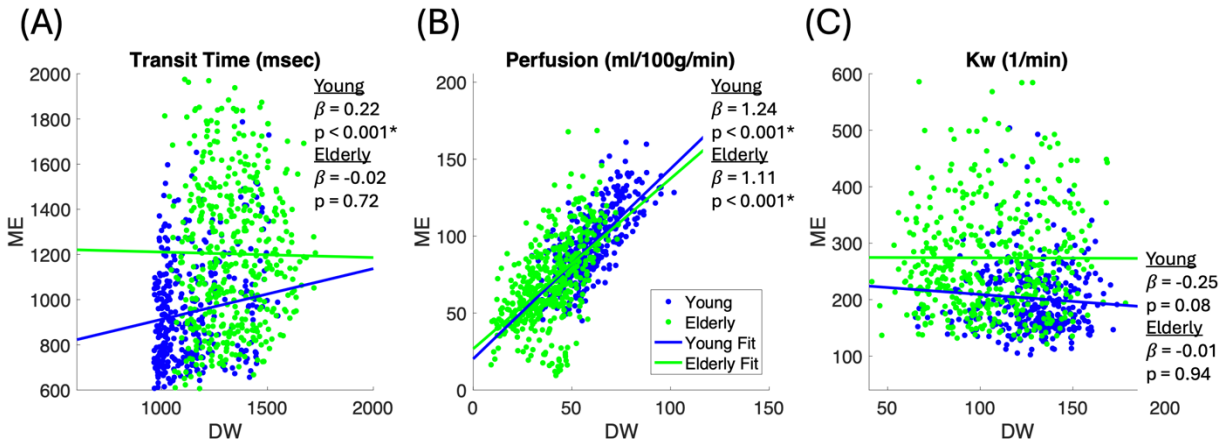

Supplemental Figure 5.5: Separate young and elderly mixed-effect linear regression between diffusion-weighted (DW) and multi-echo (ME) ASL sequences taking participant as the random effect for **(A)** arterial transit time, **(B)** cerebral perfusion, and **(C)** Kw.

5.4 Discussion

In this work, we applied the DW and ME ASL sequences in two distinct healthy cohorts: one young and another elderly. Our study is one of the first to directly compare these two BBB sequences and contributes to the current understanding of how these two techniques differ. Our results indicate a significant change in Kw within different regions of the brain associated with aging with the direction of Kw change opposite between the two BBB ASL sequences. Furthermore, ME ASL detected more extreme Kw changes with advanced age in regions, specifically around the temporal lobe, that are more associated with normal aging.

Our first major finding was that Kw showed differences between our young (aged 21-30) and elderly (aged 66-84) cohorts for both BBB sequences with DW ASL overall Kw values decreasing with age while ME ASL showing increase with age. For DW ASL, our young and elderly groups had average whole brain Kw of 128.8 $\pm$ 19.8min^{-1} and 107.2 $\pm$ 28.5min^{-1} ($p < 0.001$), respectively (Table 1). These values are consistent with those reported by Shao et al. [107] who found an average Kw in two young (aged 8-35) cohorts—male and female—to be 120.7 $\pm$ 19.8min^{-1} and 121.7 $\pm$ 18.2min^{-1}, respectively. In their elderly (aged 62-92) cohort, the Kw for male and female was 97.9 $\pm$ 31.4min^{-1} and 114.8 $\pm$

23.87min^{-1}, respectively. Interestingly, our average whole brain ATT values of 1.14 $\pm$ 0.16sec for young and 1.34 $\pm$ 0.15sec for elderly ($p < 0.001$) was a bit shorter than those reported by Shao et al in their study: 1.32 $\pm$ 0.16sec for young, male; 1.22 $\pm$ 0.13sec for young, female; 1.53 $\pm$ 0.12sec for elderly, male; and 1.47 $\pm$ 0.17sec for elderly, female. Since ATT is a prerequisite to Kw fitting, these difference, which is likely attributed to the scanner and site differences, could be responsible for the slight Kw difference reported in the two studies. [36]

Moreover, we investigated Kw within each of the four major brain lobes (i.e. frontal, parietal, temporal, and occipital) and based on parcellated FreeSurfer regions in each of these four lobes, we can observe that the DW ASL sequence shows a relatively homogenous change between the young and elderly Kw distributions with an average mean decrease of $\Delta = 22.95$min^{-1} with age (Figure 5.2A-D). This is consistent with what is seen visually on the cortical map representations in Figure 5.5A-B as well where it appears that the change in average Kw between our young and elderly cohort is more diffuse and homogenous across the entire brain. However, if we perform a two-sample t-test between the average young and old Kw for each FreeSurfer region, none of the DW p-values survive a Benjamini Hochberg false discovery rate (FDR) correction. This is not the case of ME ASL, which exhibited more extreme Kw change between the two cohorts.

For ME ASL, we reported an average global Kw of 203.7 $\pm$ 68.7min^{-1} for our young cohort and 274.7 $\pm$ 101.4min^{-1} for our elderly cohort. These values are consistent with those reported in a similar comparison study by Morgan et al. [111] in an elderly cohort (aged 46-82) which saw an average Kw of 301.5 $\pm$ 72.8min^{-1}. On a lobar level, the average Kw change for ME ASL was an increase of $\Delta = 68.0$min^{-1} (Figure 5.2E-H) . Similarly, the whole brain ATT for ME ASL for the young and elderly cohorts assessed at 0.95 $\pm$ 0.23sec and 1.20 $\pm$ 0.32sec, respectively, was lower than that reported my Morgan et al. for their elderly cohort (aged 46-82) at 1.30 $\pm$ 0.11sec. The inconsistencies in measured ATT could be one of the factors driving the discrepancies in Kw between the two studies. Moreover, in Supplemental Figure 5.2, we can observe that the change in Kw for both sequences is not uniformly observed in all

participants, with some older participants exhibiting greater changes in Kw that make reflect individual heterogeneity in underlying BBB physiology in the aging process.

Aside from ATT and Kw, it is also noteworthy that the two sequences assessed vastly different whole brain CBF values with DW measuring 59.2 ± 13.6ml/100g/min in young and 38.0 ± 13.5ml/100g/min in elderly ($p < 0.001$) and ME measuring 92.0 ± 23.5ml/100g/min in young and 70.0 ± 27.5ml/100g/min in elderly ($p < 0.001$). From a mechanistic perspective, the way in which CBF is quantified is different between DW and ME ASL with DW being a single-delay CBF calculation using a background suppressed image at PLD 2000ms [113] and ME ASL being a multi-delay acquisition using a combination of the Hadamard 4 and 8 matrices with CBF being just one of the parameters that is extracted. Overall, it is the DW ASL assessment of CBF that is consistent with previously published ASL measurements in healthy adults. [140] Nevertheless, despite the discrepancy between their whole brain averages, CBF measurements between DW and ME ASL within individual FreeSurfer cortical gray matter region are strongly positively correlated to each other ($\beta = 1.15$, $p < 0.001$) as seen in Figure 5.3B, and there appears to be a noticeable decrease in CBF in the elderly participants, which is consistent with normal aging physiology. [115]

Nevertheless, ATT and Kw were not as consistent between DW and ME ASL. In Figure 5.3, we see that the ATT between the two sequences were positively correlated ($\beta = 0.46$, $p < 0.001$) while the Kw was negatively correlated ($\beta = -0.62$, $p < 0.001$). This comparatively weaker β value for ATT corresponds to the inconsistencies in ATT measurements mentioned previously, suggesting that regional ATT values between the two sequences (Figure 5.3A) do not correspond to each other as strongly as regional CBF (Figure 5.3C). The same can be said about regional Kw and the negative correlation that exists between DW and ME ASL measurements. This negative β for average regional Kw is driven largely by the two different age groups (Figure 5.3C) and corresponds to the opposing direction of Kw change with age. These discrepancies between ATT, CBF, and Kw measured with the two BBB sequences are further analyzed with parallel plots in Figure 5.4 where each datapoint represents the

average parameter value in one of the four major brain lobes (i.e. frontal, parietal, temporal, or occipital). Here, we can see that the ME ASL detects a larger range of ATT values in both the young and elderly cohorts compared to DW ASL. This was not observed in the comparison study by Morgan et al. where the ATT values assessed with the two sequences were much more agreeable. [111] Additionally, CBF and Kw measurements are skewed higher in magnitude for ME ASL compared to DW ASL. Overall, these results point to a lack of consistence between these two techniques.

Region	Diffusion Weighted		Multi-Echo	
	LH	RH	LH	RH
Banks of the superior temporal sulcus (1)(T)	0.07	0.13	0.85	0.91
Caudal anterior cingulate gyrus (2)(F)	0.14	0.14	0.0078*	0.0038*
Caudal middle frontal gyrus (3)(F)	0.07	0.062	0.088	0.02*
Cuneus (5)(O)	0.13	0.07	0.013*	0.026*
Entorhinal cortex (6)(T)	0.95	0.98	0.0003*	0.02*
Fusiform gyrus (7)(T)	0.33	0.14	0.011*	0.01*
Inferior parietal lobule (8)(P)	0.07	0.07	0.22	0.47
Inferior temporal gyrus (9)(T)	0.07	0.14	0.041*	0.0022*
Isthmus of the cingulate gyrus (10)(T)	0.32	0.40	0.55	0.48
Lateral occipital cortex (11)(O)	0.07	0.07	0.096	0.036*
Lateral orbitofrontal cortex (12)(F)	0.32	0.07	0.053	0.053
Lingual gyrus (13)(O)	0.11	0.07	0.14	0.56
Medial orbitofrontal cortex (14)(F)	0.30	0.15	0.0039*	0.042*
Middle temporal gyrus (15)(O)	0.07	0.14	1.0	0.56
Parahippocampal gyrus (16)(F)	0.93	0.62	0.14	0.68
Paracentral lobule (17)(F/P)	0.11	0.072	0.083	0.042*
Opercular part of inferior frontal gyrus (18)(F)	0.078	0.12	0.14	0.0048*
Pars orbitalis (19)(F)	0.11	0.11	0.37	0.63
Pars triangularis (20)(F)	0.07	0.16	0.25	0.086
Pericalcarine cortex (21)(O)	0.08	0.07	0.15	0.54
Postcentral gyrus (22)(P)	0.07	0.07	0.024*	0.0061*
Posterior cingulate cortex (23)(P)	0.29	0.31	0.2	0.053
Precentral gyrus (24)(F)	0.064	0.064	0.015*	0.0035*
Precuneus (25)(P)	0.071	0.08	0.088	0.041*
Rostral anterior cingulate cortex (26)(F)	0.17	0.15	0.028*	0.35
Rostral middle frontal cortex (27)(F)	0.07	0.07	0.85	0.17
Superior frontal gyrus (28)(F)	0.07	0.07	0.12	0.02*
Superior parietal lobule (29)(P)	0.14	0.14	0.024*	0.048*
Superior temporal gyrus (30)(T)	0.07	0.10	0.52	0.086
Supra marginal gyrus (31)(P)	0.07	0.078	0.67	0.088
Frontal pole (32)(F)	0.15	0.07	0.33	0.85
Temporal pole (33)(T)	0.30	0.13	0.092	0.14
Transverse temporal gyrus (34)(T)	0.07	0.14	0.024*	0.0078*
Insula (35)(n/a)	0.40	0.08	0.016*	0.0008*

* $p < 0.05$

Table 5.2: Benjamini Hochberg corrected p-values between young and elderly average Kw in each of the 35 FreeSurfer cortical gray matter regions for diffusion-weighted (DW) and multi-echo (ME) ASL for left

hemisphere (LH) and right hemisphere (RH). Each FreeSurfer region is also categorized into one of the four major brain lobes: (F), parietal (P), temporal (T), and occipital (O).

The second major key finding of our work is shown in Figure 5.5, which overlays average regional Kw values onto 3D cortical maps in MNI space for young and elderly cohorts across the two sequences. Supplement Figure 5.5 is an extension of this analysis that overlays the t-statistics between young and elderly on 3D cortical maps in MNI space. Here, we can appreciate that Kw becomes more extreme in regions associated with aging in the ME ASL elderly maps (Figure 5.5C-D) as compared to the younger Kw cohort. Additionally, the magnitude of Kw change between young and old is roughly three times greater for ME ASL compared with DW ASL, and in opposing directions. This is consistent with what is currently reported in the literature. [21, 107, 111] The advantage of this greater change for ME ASL is that the two sample t-tests for average regional Kw between young and elderly remain statistically significant for many regions even after the Benjamini Hochberg FDR correction (Table 2). On the other hand, none of p-values between young and elderly for DW ASL survived FDR correction.

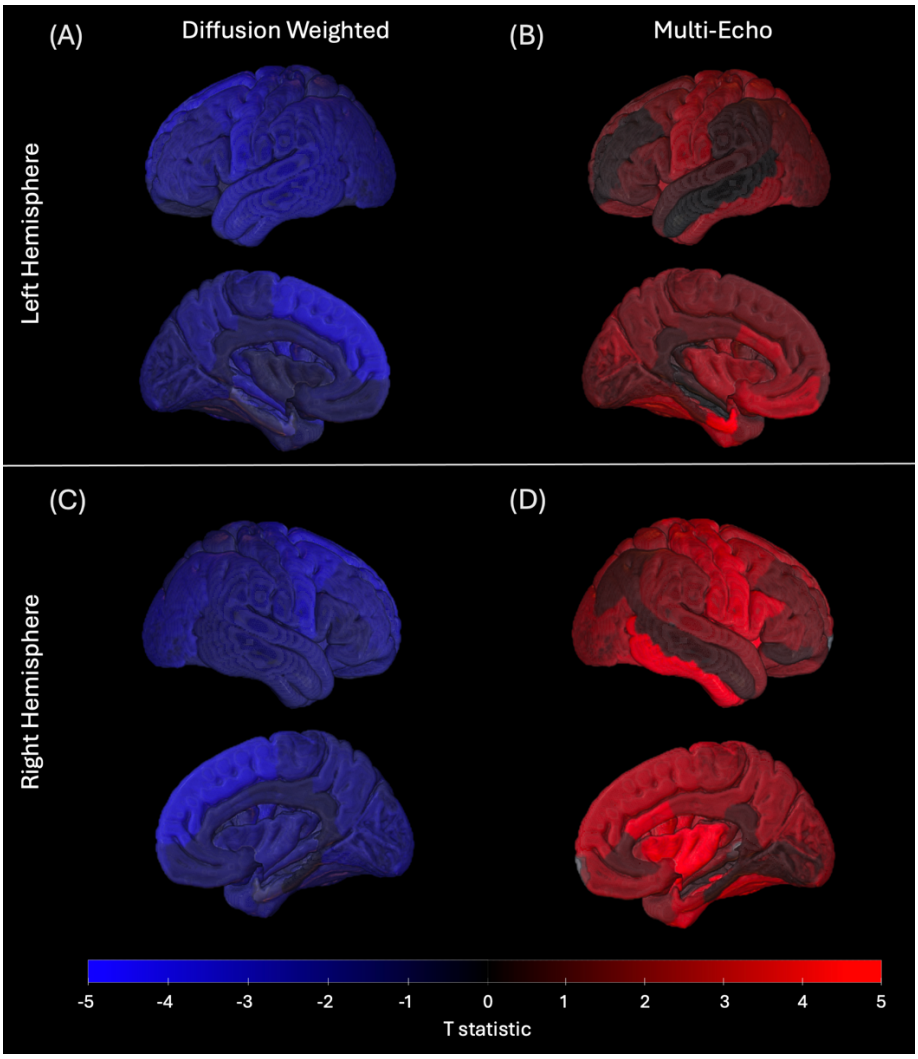

Supplemental Figure 5.6: Regional t-statistics between young and elderly Kw cortical maps for diffusion-weighted (DW) and multi-echo (ME) ASL. The direction of change between young and old is opposite between the two sequences.

Moreover, our statistical analysis in Table 2 shows significant differences between young and elderly cohorts for ME ASL in regions of the brain previously reported to be associated with aging. We identified significant age group differences in areas associated with the frontal lobe, including the anterior cingulate gyrus, the middle frontal gyrus, the orbitofrontal gyrus, and the superior frontal gyrus. Additionally, both the precentral and postcentral gyrus associated with motor and sensory function, respectively, were also significantly different. Further, regions in the temporal lobe that were significant

include the entorhinal cortex, the insula, the fusiform gyrus, and the inferior and transverse temporal gyrus. The cuneus and the lateral occipital cortex of the occipital lobe were also significantly different between the young and elderly groups. Overall, these changes in regional Kw values as detected by ME ASL corresponds to cortical gray matter regions that have been shown to deteriorate with age. It has been established through volumetric and morphometric neuroimaging studies that there exists a consistent age-dependent decrease in regional gray matter volume in the temporal lobe, cingulate cortex, and prefrontal cortex. [141, 142] In addition, the size of regions associated with the sensorimotor network has been shown to be negatively correlated with age. [143] These regions include the motor, sensory and auditory cortex located in the superior temporal gyrus along with the visual cortex of the occipital lobe. [144] Moreover, the observation that many of these changes in regional Kw (11 out of 17) were bilaterally significant in both hemispheres further strengthens the validity of our findings.

In addition, changes in Kw between young and elderly were largely consistent with two recent studies investigating at Kw across the lifespan. In a recent ME ASL study, Padrela et al. [21] found Tex, the multiplicative inverse of Kw, to change in all gray matter brain regions except the occipital lobe. In another recent DW ASL study by Shao et al. [20], the authors highlighted the hippocampus, as well as specific regions in the frontal, parietal, and temporal lobes to exhibit age-dependent changes. While these are largely consistent with our ME ASL findings, it is important to note that none of our DW ASL regions passed FDR correction, probably due to our relatively small sample size (n = 30) compared to that of Shao et al. (n = 186). Thus, ME ASL appear to be more sensitive in detecting Kw changes associated with aging in different regions of the brain. This could be because the overall change in Kw from baseline (i.e. young) is much larger for ME ASL due to yet unknown physical differences between the two sequences.

Our study is unique from others utilizing the BBB DW and ME ASL sequences in that we introduce a new experimental approach of having two distinct age groups. Previous work in this area have only looked at large sample sizes setting age a continuous variable. [20, 21, 49] By applying both the DW and ME ASL sequences in two distinct age groups, we contribute a novel perspective to the debate on how Kw changes with age. Further, through characterizing how these two BBB sequences change with

healthy aging, we will be more prepared in the future to understand to study different neurological disease states where the vasculature is impacted.

Furthermore, it is important to introduce the biological mechanisms behind why Kw changes in opposite direction with age. For the DW ASL sequence, it is thought that Kw decreases with age because of the nonpolarized expression of aquaporin water channels away from the astrocytic end feet. This contributes to an overall slowing down of transcellular water exchange from the blood to the brain parenchyma. On the other hand, for ME ASL, it is thought that Kw increases with age because of breakdown of the tight junction proteins that connect adjacent endothelial cells. This breakdown allows for the paracellular passage of water from the blood to the brain tissue and is more consistent with DCE MRI, the current clinically used method of assessing BBB permeability in humans.

While it is not yet known exactly why these two methods detect opposing changes in Kw, we hypothesize that it may be because of the physical mechanism each of these sequences use to split the overall ASL signal into an intravascular and extravascular component. In other words, the bipolar gradients used in DW ASL and the multiple 180 degrees pulse trains generated in ME ASL likely contribute to the yet unresolved difference between the two sequences that result in opposing change in Kw with age and with disease. Future work in this area could apply a multimodal approach to resolve this discrepancy by applying these sequences in an animal model that has genetically altered the BBB structure at either the aquaporin or tight junction genes. Further, it would be helpful to link MRI scans to histology data to confirm on a tissue level what regional changes in Kw corresponds to on a biological scale.

With regards to susceptibility effects and the ability of DW and ME sequences to account for these, we can speculate that it is perhaps the DW ASL sequence that are more resistant to susceptibility artifacts generated by signal distortions that occur at the boundaries of tissues with different magnetic properties, such as air-tissue interfaces in the sinus and bone-tissue interfaces throughout the brain. The reason behind this assertion is that the DW ASL sequence used in for dissertation work applies a heavy postprocessing regularization protocol that blurs the image there by dulling bright spots that may occur

because of these signal distortions. ME ASL scans, on the other hand, are smoothed at the raw imaging stage. Susceptibility signal distortion artifact could be responsible for the relatively high Kw seen in the ME ASL young group as indicated by the white arrows in Figure 5.5. It would be interesting to see in the future how the developers of the ME ASL sequence rectify this important issue.

Our study has several limitations. Though we designed our analysis to have very different age groups to maximize detection of age-related Kw, the sample size is still relatively small. This impacts our ability to apply more advanced mixed-effect linear regression models that could potentially take the age groups as an interaction term to more adequately model the relationship between measurements taken with DW and ME ASL. Second, the resolutions of the DW and ME ASL BBB sequences are different: 3.5mm × 3.5mm × 8mm for DW compared to 5mm × 5mm × 5mm for ME ASL. This difference could impact regional Kw extraction with the FreeSurfer cortical masks, especially for smaller brain structures. Furthermore, the DW ASL BBB Kw maps are smoothed and blurred before they are analyzed through total generalized variation (TGV) [113] that ultimately makes the effective resolution of the resulting DW ASL Kw maps challenging to measure. Third, there exhibited differences in the ATT measured between the two techniques that may be mitigated with more developed methods such as multi-delay DW ASL. Finally, there are differences in the readout technique between both sequences.

5.5 Conclusion

In this study, we applied the diffusion-weighted (DW) and multi-echo (ME) ASL sequences in two healthy, adult cohorts of distinct age groups. We found that both sequences detected significant changes in whole brain Kw and within the four major brain lobes, though in opposite directions, but that ME ASL was more sensitive in detecting Kw changes in specific regions, particularly those associated with aging. Given these differences, DW ASL requires a larger number of participants to detect meaningful changes in Kw within difference regions of the brain. ME ASL, on the other hand, may possess advantages in studies with smaller sample sizes or in clinical usage. Nevertheless, it's important to remember that this conclusion is based on the two sequences as they were used in our study, and, thus,

could change with future generations and modifications to both sequence parameters and post-processing steps.

Left Hemisphere	Diffusion Weighted		Multi-Echo	
	T Statistics	P Value	T Statistics	P Value
Banks of the superior temporal sulcus (1)	2.5	0.017*	0.26	0.80
Caudal anterior cingulate gyrus (2)	1.7	0.099	3.8	0.0011*
Caudal middle frontal gyrus (3)	3.3	0.0043*	2.1	0.047*
Cuneus (5)	1.8	0.078	3.5	0.0025*
Entorhinal cortex (6)	-0.11	0.91	6.1	<0.0001
Fusiform gyrus (7)	1.1	0.29	3.7	0.0018*
Inferior parietal lobule (8)	2.4	0.024*	1.5	0.16
Inferior temporal gyrus (9)	2.6	0.016*	2.8	0.015*
Isthmus of the cingulate gyrus (10)	1.1	0.28	0.75	0.46
Lateral occipital cortex (11)	2.5	0.019*	2.0	0.055
Lateral orbitofrontal cortex (12)	1.1	0.28	2.4	0.024*
Lingual gyrus (13)	2.0	0.057	1.8	0.093
Medial orbitofrontal cortex (14)	1.2	0.24	4.1	0.0003*
Middle temporal gyrus (15)	2.7	0.011*	-0.022	0.98
Parahippocampal gyrus (16)	-0.16	0.87	1.8	0.092
Paracentral lobule (17)	2.0	0.061	2.2	0.0390*
Opercular part of inferior frontal gyrus (18)	2.3	0.032*	1.8	0.09
Pars orbitalis (19)	2.0	0.054	1.1	0.28
Pars triangularis (20)	2.4	0.026*	1.4	0.18
Pericalcarine cortex (21)	2.2	0.036*	1.7	0.099
Postcentral gyrus (22)	2.7	0.013*	3.0	0.007*
Posterior cingulate cortex (23)	1.2	0.24	1.5	0.14
Precentral gyrus (24)	3.5	0.0027*	3.3	0.0029*
Precuneus (25)	2.3	0.027*	2.1	0.048*
Rostral anterior cingulate cortex (26)	1.5	0.13	2.8	0.0091*
Rostral middle frontal cortex (27)	2.4	0.024*	0.27	0.79
Superior frontal gyrus (28)	3.7	0.014*	1.9	0.07
Superior parietal lobule (29)	1.8	0.086	3.0	0.0066*
Superior temporal gyrus (30)	2.8	0.0094	0.82	0.42
Supra marginal gyrus (31)	2.5	0.020*	0.54	0.60
Frontal pole (32)	1.7	0.11	1.2	0.24
Temporal pole (33)	1.2	0.25	2.1	0.051
Transverse temporal gyrus (34)	2.7	0.013*	2.9	0.0073*
Insula (35)	0.92	0.37	3.2	0.0033*

* $p < 0.05$

Supplemental Table 5.1: Left hemisphere uncorrected t-test of average Kw values between elderly and young participants in 35 FreeSurfer gray matter cortical regions.

Right Hemisphere	Diffusion Weighted		Multi-Echo	
	T Statistics	P Value	T Statistics	P Value
Banks of the superior temporal sulcus (1)	1.9	0.073	-0.17	0.87
Caudal anterior cingulate gyrus (2)	1.7	0.10	4.3	0.0003*
Caudal middle frontal gyrus (3)	3.9	0.0009*	3.1	0.005*
Cuneus (5)	2.7	0.013*	2.9	0.0081*
Entorhinal cortex (6)	-0.063	0.95	3.3	0.0046*
Fusiform gyrus (7)	1.8	0.089	3.8	0.0016*
Inferior parietal lobule (8)	2.7	0.01*	0.93	0.36
Inferior temporal gyrus (9)	1.7	0.10	4.9	0.0001*
Isthmus of the cingulate gyrus (10)	0.94	0.36	0.90	0.38
Lateral occipital cortex (11)	2.9	0.0083*	2.8	0.012*
Lateral orbitofrontal cortex (12)	2.4	0.026*	2.4	0.024*
Lingual gyrus (13)	2.4	0.026*	0.72	0.48
Medial orbitofrontal cortex (14)	1.6	0.12	2.6	0.017*
Middle temporal gyrus (15)	1.8	0.087	0.72	0.48
Parahippocampal gyrus (16)	0.57	0.58	0.51	0.61
Paracentral lobule (17)	2.4	0.029*	2.6	0.017*
Opercular part of inferior frontal gyrus (18)	1.9	0.069	4.0	0.0005*
Pars orbitalis (19)	2.0	0.06	0.61	0.54
Pars triangularis (20)	1.6	0.13	2.1	0.043*
Pericalcarine cortex (21)	2.4	0.025*	0.79	0.44
Postcentral gyrus (22)	2.4	0.024*	3.9	0.0007*
Posterior cingulate cortex (23)	1.1	0.26	2.4	0.023*
Precentral gyrus (24)	3.5	0.0024*	4.3	0.0002*
Precuneus (25)	2.2	0.038*	2.6	0.015*
Rostral anterior cingulate cortex (26)	1.6	0.12	1.1	0.26
Rostral middle frontal cortex (27)	2.6	0.015*	1.6	0.11
Superior frontal gyrus (28)	3.8	0.0071*	3.1	0.0051*
Superior parietal lobule (29)	1.7	0.093	2.5	0.02*
Superior temporal gyrus (30)	2.1	0.049*	2.1	0.042*
Supra marginal gyrus (31)	2.2	0.033*	2.1	0.046*
Frontal pole (32)	2.6	0.020*	-0.28	0.78
Temporal pole (33)	1.9	0.078	1.8	0.084
Transverse temporal gyrus (34)	1.7	0.098	3.7	0.001*
Insula (35)	2.2	0.038*	5.2	<0.0001*

* $p < 0.05$

Supplemental Table 5.2: Right hemisphere uncorrected t-test of average Kw values between elderly and young participants in 35 FreeSurfer gray matter cortical regions for the right hemisphere.

Chapter 6 Linking Water Exchange Rate to Markers of Inflammation in Schizophrenia

6.1 Introduction

6.1.1 Biology

Schizophrenia is among the most disabling and economically catastrophic medical disorders, ranked by the World Health Organization in their 1996 comprehensive report as one of the top 10 illnesses contributing to the global disease burden. [145] Since then, a 2016 repeat study found that that burden has only increased due to population growth. [146] Schizophrenia is characterized dichotomously by positive symptoms, which include hallucinations or delusions, and disorganized speech; and negative symptoms, such as flat affect or poverty of speech, and impairments in cognition. However, perhaps what makes this disorder so devastating is the age of onset from adolescence to young adulthood. Schizophrenia strikes patients when many are just achieving independence in the world.

Unlike many other medical disorders, the biological underpinnings of schizophrenia remain unclear. [147] The condition is often characterized as a syndrome comprising of multiple distinct processes, each with its own etiology. [148] Schizophrenia is currently diagnosed according to the guidelines outlined in the Diagnostic and Statistical Manual of Mental Disorders (DSM). If an individual's presenting symptoms meet or exceed the minimum number from a list of symptoms for a specific time period, then he is given the diagnosis. This symptom-based—rather than a biology-based—way of diagnosing disease is unique to psychiatry and exists because it is widely accepted that the brains of psychiatric patients are indistinguishable from their healthy counterparts. However, advancements in brain imaging technology have led many to challenge this dogma, starting with a seminal publication in the 1970s [149] that showed enlargement of the ventricles in schizophrenic brains. Since then, a flurry of neuroimaging studies has been undertaken to better understand the biological and neurological causes of psychiatric disorders. [147, 150]

The most established theory for schizophrenia is the dopamine hypothesis, which postulates that overactivity of the dopamine circuitry in the subcortical striatum and concomitant hypoactivity in the

cortex is responsible for the positive symptoms of the disorder. [151] The dopamine hypothesis was discovered serendipitously when, in the 1950s, the sedative chlorpromazine, a dopamine D2 receptor antagonist, was found to have therapeutic effects in schizophrenic patients. To this day, antipsychotics targeting the dopamine pathway remain the primary treatment method for schizophrenia, though newer drugs have also begun targeting serotonergic and noradrenergic neurotransmission. [152] Nevertheless, given the heterogeneity of the disorder, it is not surprising that up to 34% of patients with schizophrenia are not responsive to antipsychotic treatment that targets the dopamine pathway. [153]

Recently, there has been increased focus on the role inflammation plays in the pathogenesis of schizophrenia as a complement to the dopamine hypothesis. Increased peripheral inflammatory markers, for instance, have been associated with worse cognitive performance and related cortical thickness reduction. [154] Additionally, animal models of schizophrenia show that under certain conditions, an immune disturbance in early life, such as an infection-triggered immune activation, might trigger lifelong immune reactivity. [155-157] Chronic stress has also been shown to induce increased levels of cytokines and contribute to a lasting pro-inflammatory state. [158] Taken together, immune alterations can influence the dopaminergic, serotonergic, noradrenergic, and glutamatergic neurotransmission and manifest as psychiatric symptoms. In fact, recent studies where anti-inflammatory drugs are administered as adjuvants to antipsychotic treatments in schizophrenic patients have shown to be promising in reducing symptoms. [159, 160]

Moreover, the blood-brain barrier (BBB) and the blood-cerebrospinal fluid barrier (BCSFB) are interfaces where peripheral blood circulation meets the tissue and ventricles, respectively. Both the BBB and the BCSFB provide an entry point for immune cells during an acute inflammatory response when the ensuing milieu can lead to the disruption of the tight junction function, resulting in increased leakiness across the barrier. [161] Contrastingly, with chronic inflammation and ensuing fibrosis, the barrier can become even more difficult to traverse, as exhibited by decreased permeability of the BCSFB in patients with Alzheimer's disease. [63] Generally, while these barriers have been recognized as central factors in

the development of many neurological disorders, such as neurodegeneration, [113, 162-164] much less is known about the role of the BBB and BCSFB in psychiatric disorders like schizophrenia.

6.1.2 Imaging of Schizophrenia

The major objective of this chapter is to optimize noninvasive tools to assess the permeability of the BBB as a proxy for its integrity in patients with schizophrenia and to show that these metrics are different from those of healthy controls. The long-term goals of this project are 1) the development of neuroimaging biomarkers for schizophrenia that could facilitate its early diagnosis and 2) the contribution to the understanding of the link between the BBB breakdown to neuroinflammation.

ASL has emerged as a sensitive way to assess BBB integrity. The small molecular size of water, as compared to GBCA, makes ASL more appropriate to study disease processes where BBB breakdown is more subtle since water can traverse the barrier at a much lesser severity of damage. With the proposal of the two-compartment model by Parkes et al. [35] to more accurately quantify perfusion, MRI physicists began to incorporate a water exchange rate (Kw) into the model to estimate the rate at which tagged water molecules move from the vascular space to the tissue space of the two-compartment model. This Kw term can be thought of as a proxy measure for BBB integrity. [37, 52] In this chapter, we will apply diffusion-weighted (DW)-ASL, which utilizes the different diffusivity constants (D) of the blood and brain tissue to split the overall ASL kinetic signal into an intravascular and extravascular component, to study regional Kw differences between schizophrenic patients and healthy controls. [36, 113]

From a historical perspective, there has been much controversy surrounding the diagnosis and management of psychiatric disorders much of which is centered on the checklist-based nature of the DSM and the heavy influence of the pharmaceutical companies on academic clinical leaders who set these diagnostic criterion. [165] With the ushering in of the biochemical theories of psychiatric disorders, there is a perceived trend that the current US healthcare system is moving away from a psychoanalytic approach and treating these pharmacological agents, which have heavy side effects, as a cure-all. This

approach has been met with heavy skepticism with many critics believing that US mental health field is in deep crisis. [166, 167]

Experts in the field believe that the future of psychiatry lies in a more biological and, thus, precise approach to diagnosing psychiatric disorders. This is where neuroimaging is applicable. For instance, a group at Stanford University led by Williams et al. is developing a brain-based taxonomy for mental disease based on the functional connectivity of different brain circuits using functional MRI (fMRI). [168] Their efforts to develop clinical tools to diagnose mental illness represent the frontier of neuroimaging applications in psychiatry. Nevertheless, challenges remain as the current checklist-based diagnostic criterion themselves lends to a very heterogenous grouping of biological subjects within each diagnostic category. [169] Challenges associated with the biological heterogeneity of DSM diagnosis are further seen in the lack of a singular animal model for schizophrenia. [170] If efforts on this front are fruitful, we could witness the development of a new set of biomarker-based diagnostic criteria for mental illness.

Our aim of imaging Kw across the BBB as a proxy measure for its integrity is another step toward studying ASL's potential to detect underlying changes within the tissue that give clue to its inflammatory state. The overarching purpose is toward the development of a new method to study the mechanistic causes leading up to the development of schizophrenia.

6.2 Materials and Methods

6.2.1 Participants

13 young, healthy participants (aged 18-32, 10 female) and 20 young participants with the diagnosis of schizophrenia (aged 14-37, 10 female) underwent MRI scans on a 3T Magnetom Prisma (Siemens Healthineers, Erlangen, Germany). Young healthy participants were recruited both from an institutional registry of study volunteers and through emailing the student body at the University of California, Davis. Patients were recruited through an institutional registry of an ongoing clinical trial at UC Davis. The inclusion criteria for this study are the following: 16-40 years of age, DSM-5 diagnosis of

schizophrenia or schizoaffective disorder, onset of psychosis within the last 5 years, and clinically stable for at least 3 months. The exclusion criteria include the following: substance abuse disorder within the last 6 months or positive urine drug test, IQ less than 70, history of neurological illness or significant head trauma, corrected visual acuity below 20/30, and any contraindication to MRI. All scans for this study were performed on a single scanner. This study was approved by the institutional review board and ethics committee at the University of California, Davis and written informed consent was obtained from all participants.

6.2.2 Imaging Protocol

T1-weighted magnetization prepared rapid gradient echo sequence (MPRAGE) structural images [120] were acquired at resolution = 1.0 × 1.0 × 1.0 mm^3 (scan time ~ 5min). 3D gradient-and-spin-echo (GRASE) diffusion-weighted (DW) ASL scans to assess Kw was set at a DW PLDs of 1800ms. The flow encoding arterial spin tagging (FEAST) [47] acquisition to measure ATT is incorporated into each DW ASL scan and was kept identical at a PLD of 900ms across all repetitions.

Furthermore, DW ASL sequence was acquired at TR = 4s, TE = 36.5ms, FOV = 224mm, matrix size = 64 × 64, 12 slices (10% oversampling), resolution = 3.5 × 3.5 × 8 mm^3, label/control duration = 1500ms, and centric ordering. [110, 113] DW ASL scans included 20 repetitions with diffusion weightings (*b*-value) at 0 and 50s/mm^2 to measure Kw, which lasted ~6min. The FEAST acquisition consists of 15 repetitions at a diffusion weighting (*b*-value) of 0 and 14s/mm^2 with a total acquisition time of ~4min to estimate ATT. Therefore, the total time for each scan ~10min. The center of the slice prescription was aligned with the center of the ventricles (close to the pineal gland in the sagittal view) so that as much of the brain could be covered as possible.

6.2.3 Post-processing

FreeSurfer [18] was used to segment the structural image into 35 cortical gray matter regions bilaterally for region of interest (ROI) analysis. We used the Water Exchange Quantification Toolbox (WEQT) to generate Kw maps. Only gray matter ROIs with 70% voxel coverage or greater were

included. Right and left hemisphere gray matter Kw were averaged before statistical analysis. Cortical representations are of the average regional Kw in the healthy and schizophrenic groups overlayed onto an MNI template.

6.2.4 Statistical Methods

Mixed effect linear regression models were set up taking participants as a random effect to determine statistical differences between the control and patient distributions. This was done for global arterial transit time (ATT), cerebral blood flow (CBF), and Kw values as well as for Kw distributions within each of the four major lobes of the brain (Figure 6.3).

6.3 Results

Figure 6.1 shows the average Kw distributions for 35 FreeSurfer cortical gray matter overlayed onto 3D cortical maps in MNI space. Visually, the Kw distribution does appear to be lower in the patient group.

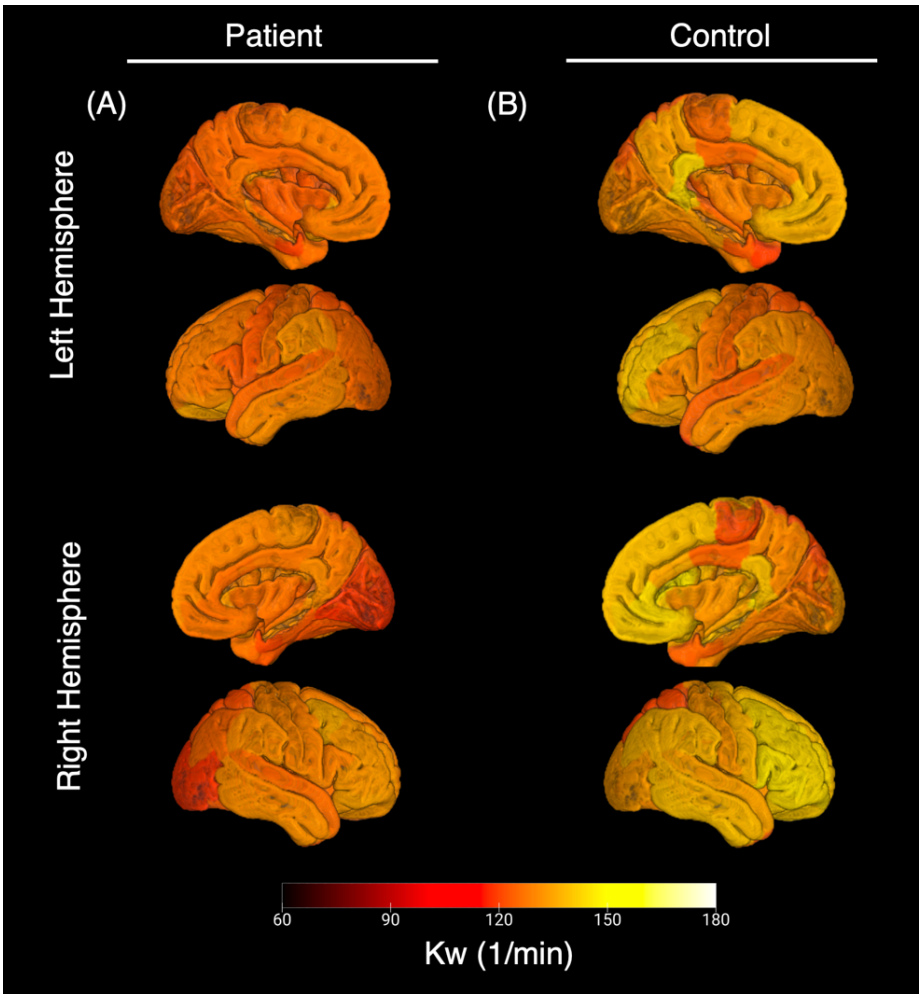

Figure 6.1: Kw cortical map representations in MNI space for **(A)** patients and **(B)** controls.

Figure 6.2 shows the t-statistics between Kw values within each FreeSurfer region between control and patient overlayed onto a 3D cortical map in MNI space. Only one of the regions, the medial orbitofrontal cortex, was statistically significant ($p = 0.03$) between the two groups. However, none of the regions survived false discovery rate (FDR) correction with the Benjamini Hochberg adjustment.

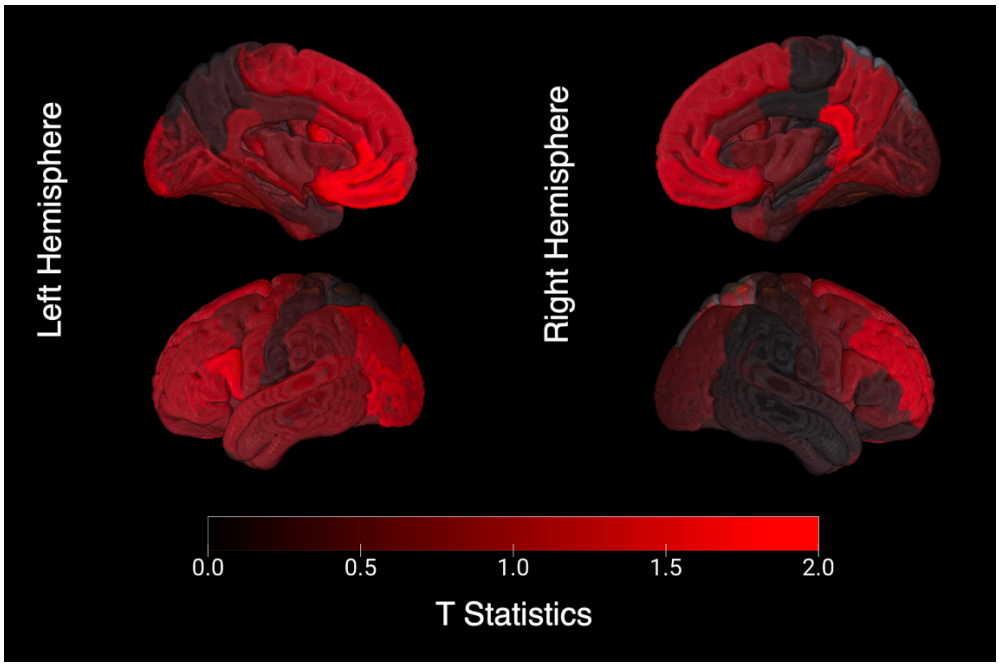

Figure 6.2: T statistics cortical maps between patient and control.

Figure 6.3 shows the FreeSurfer regional average Kw distribution with each of the FreeSurfer region organized into one of the four major lobes of the brain. Here, we see that the frontal, temporal, and occipital lobes were all statistically significantly different between control and patient.

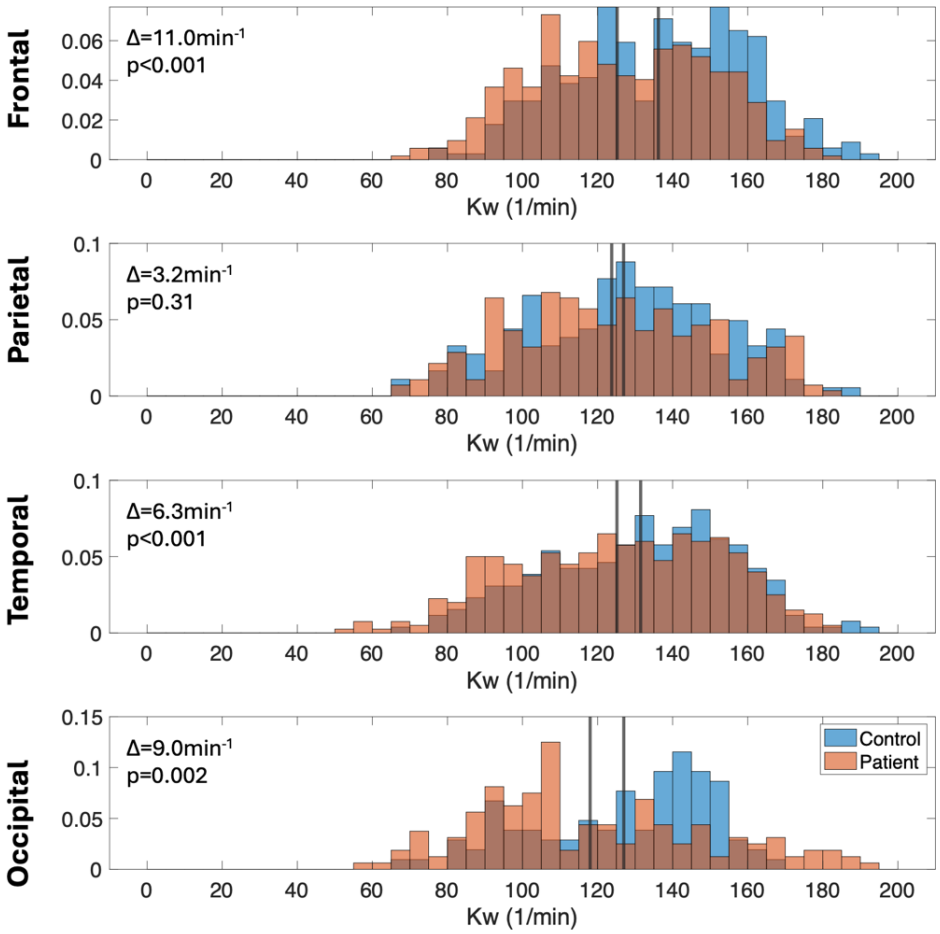

Figure 6.3: Kw distributions between patient and control in 35 FreeSurfer cortical gray matter region.

Figure 6.4 shows violin plots of differences in average whole brain ATT, CBF, and Kw between the schizophrenia and health control groups.

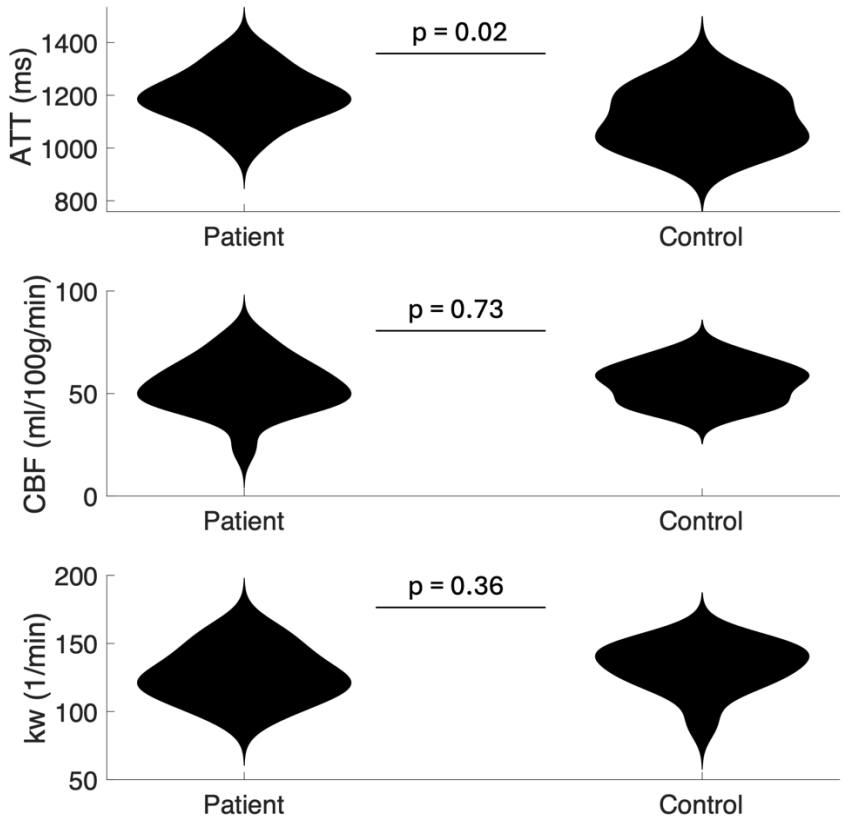

Figure 6.4: Whole brain ATT, CBF, and Kw violin plots between patient and control groups.

Figure 6.5 is the correlation analysis for eighteen schizophrenic participants who had symptom scores, which were correlated to whole brain ATT, CBF, and Kw. Results showed that none of the plots reached statistical significance.

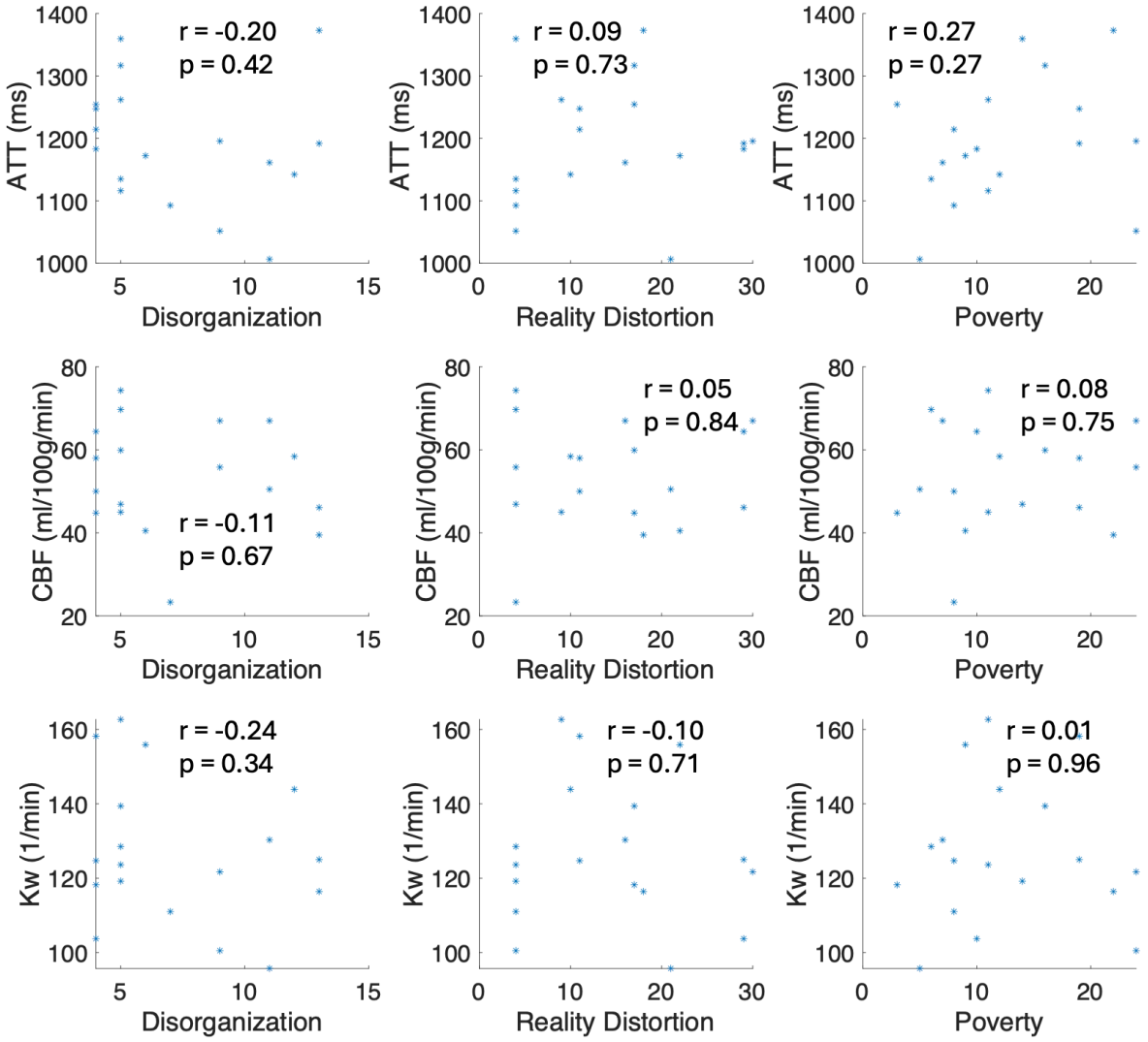

Figure 6.5: Correlation of symptom score to whole brain ATT, CBF and Kw for eighteen participants with schizophrenia.

6.4 Discussion

In this preliminary analysis, we showed that there exist significant differences in average Kw between the healthy control and the schizophrenia groups. These findings are exciting and promising as these Kw differences are seen throughout the cortical gray matter regions. Furthermore, as expected in young healthy brains, we do not see any significant differences in whole brain CBF between the two

groups, but that—surprisingly—we do see that the patient group possesses a slightly longer ATT than the healthy control group.

While these differences were significant at the whole brain and lobar level, they were not significant on a FreeSurfer regional level. A possible explanation for this is that our sample size is currently small (n = 33) as this study is still ongoing and in the data collection phase. These numbers and distribution between controls (n = 13) and patients (n = 20) are reflective of the aging study performed in Chapter 5, which also failed to detect significant regional differences in Kw with DW ASL due to the relatively small sample size. Furthermore, it is important to mention that we did not control for age, sex, or drug use, which could further affect our final results.

There are emerging studies that are beginning to use DCE MRI to study differences between the brains of patients with schizophrenia and those of healthy controls. For instance, one by Moussiopoulou et al. found higher BBB leakage, as measured by K_{trans} calculated by the Patlak model, on a whole brain level with the effect more pronounced in first episode compared with multiple episode psychosis compared to another group of healthy age- and sex- matched controls. [171] Yet, the authors failed to detect associations between BBB leakage and measures of cognition, psychopathology, peripheral inflammation, and albumin CBF/serum ratio. This study is particularly interesting because its experimental set up is very similar to the one that we have implemented in this work. Furthermore, their results very much mirror our preliminary analysis in that while we also see differences BBB leakiness between schizophrenic and health brains, these BBB exchange measures fail to correlate with symptom data. One possible explanation for this could be some of the inherent limitations with assessing psychiatric symptomology, which is largely based on self-reporting and, thus, is difficult to normalize across many participants. Yet, the irony is that it is this very attribute of psychiatry that is driving efforts toward a more biological understanding of psychiatric disorders.

Future work will include both more controls and patients to increase the power of our analysis. Additionally, free water, glutathione, and neuromelanin levels representing central markers of inflammation along with peripheral markers of inflammation that includes plasma cytokine levels will be

analyzed along with the Kw metric to study the relationship between Kw and processes associated with the maternal immune activation (MIA) theory of schizophrenia. This analysis will occur after completion of the data acquisition phase of the Conte Center study. Finally, it is also important to mention that quality control is also being performed on the DW ASL scans to assess for motion, which may be an important confounding factor particularly for psychiatric patients undergoing long scans. This analysis presents with some challenges in the sense that the toolbox to calculate Kw is tightly controlled through a proprietary software.

Chapter 7 Conclusion and Future Directions

7.1 Conclusion

The recent discovery of the glymphatic system—the brain's waste clearance system—has led to increased interest in assessing the functional status of this structure. It is thought that deterioration of glymphatic function can contribute to neurodegenerative diseases, such as Alzheimer's and related dementias where there is aberrant protein accumulation within the brain parenchyma. The blood-brain barrier (BBB) is a cellular structure that is interconnected with the glymphatic system architecture. Assessing water exchange rate (Kw) across the BBB with arterial spin labeling (ASL) MRI has emerged as a candidate noninvasive, nonionizing and contrast-free method to assess this waste clearance structure. In fact, mounting evidence has implicated BBB disruption as a hallmark feature of many neurological diseases.

In this work, we primarily focused on ASL methods to assess structures associated with the glymphatic system, namely the choroid plexus and the BBB. In Chapter 3, we showed that multi-delay ASL can detect perfusion changes within the choroid plexus—an organ within the ventricles that produces cerebrospinal fluid (CSF)—associated with a vasodilation challenge comparable to ^{15}O-water PET, the current gold standard for assessing cerebral perfusion. Further, multi-delay ASL possessed repeatability at baseline conditions comparable to ^{15}O-water PET. The production of CSF by the choroid plexus is a critical physiological function associated with the glymphatic system that enables the brain to deliver nutrients and clear away waste. Assessing choroid plexus perfusion, which was historically only possible through surgery, using ASL could give us clues to the overall health status of the organ and provide us with a marker with which clinicians can assess the overall status of a disease with.

In Chapter 4, we studied and optimized a relatively novel diffusion-weighted (DW) ASL sequence acquired from the University of Southern California on our scanners through both computer simulation studies as well as test runs on a small sample of ten young, healthy participants. Simulation results showed the two-compartment model used to fit Kw from the ASL signal to be robust to different

levels of added white Gaussian noise at physiological arterial transit times (ATT). Additionally, *in vivo* studies affirmed the reliability of the sequence to assessing regional Kw at different post-label delay (PLD) times and suggested that a longer DW PLD time of 2100ms, which may be more appropriate for elderly participants, to possess comparable intrasession repeatability as compared to the standard DW PLD of 1800ms. Our overall findings in Chapter 4 will lay the foundational data to support additional studies using this sequence in different disease states at the University of California, Davis.

Chapters 5 and 6 of this dissertation involves applying the scientific and technical expertise gained in Chapters 3 and 4 to answer clinical questions. Chapter 5 is a comparison study between the multi-echo (ME) ASL sequence, which was acquired from the Fraunhofer Mevis in Bremen, Germany, and the DW ASL sequence as applied in two adult cohorts of different age: one young and one elderly. Results showed significant changes in Kw across different regions of the brain with both sequences, but in opposing direction as consistent with other literature findings. However, ME ASL showed more extreme Kw changes in regions of the brain associated with aging and these changes remained statistically significant even when corrected for false discovery rate (FDR). The importance of chapter 5 is that it reframes a currently unresolved dispute between two competing BBB ASL sequences in a new experimental design with the aim of contributing a different angle to the debate between the opposing directionality of Kw change with age.

Finally, Chapter 6 is an exploratory chapter in collaboration with the University of California, Davis Conte Center to apply the DW ASL BBB sequence in a group of participants with schizophrenia to study changes in BBB exchange dynamics. The purpose is to see if this sequence and analysis pipeline can detect subtle BBB permeability changes in the schizophrenic brain. Preliminary results indicate that there may be subtle detectable and statistically significant differences in Kw in different regions of the schizophrenic brain as compared to their age-matched, healthy controls. As expected, the change in BBB water exchange dynamics in the psychiatric population is not as drastic as that seen with aging.

7.2 Future Direction

The findings in this dissertation has already been utilized to prepare for a multimodal investigation to study BBB exchange dynamics that involves applying dynamic contrast enhanced (DCE) MRI, ME ASL, and DW ASL in a group of participants with Alzheimer's disease (AD) to better understand the role of BBB dysfunction in AD, including its mechanistic links and timing relative to AD neuropathology, modification by genetics and exposome, regional vulnerability, and potential to promote neurodegeneration. Professor Audrey Fan, co-director of the imaging core of the Alzheimer's Disease Research Center (ADRC) at the University of California, Davis and chair of this dissertation committee is partnering with Professor Emilie Reas of the University of California, San Diego to apply a multi-modal MRI imaging approach to correlate the transfer constants with existing plasma markers of AD pathology as well as established genetic markers of AD risk and pathology. Additionally, machine learning algorithms will be trained to develop biomarkers using all three MRI imaging modalities—DCE MRI, DW ASL, and ME ASL—to develop region- and modality-specific models to predict cognitive decline and AD pathology.

At the time of writing, the DW ASL sequence has already been updated to include a multi-PLD acquisition protocol that may be more reliable in measuring Kw. Though this newer version has yet to make it out into the research domain, it would not be surprising to see newer publications using this multi-PLD sequence coming out of the DW ASL developers and collaborators. Additionally, there are efforts to incorporate velocity-selective ASL, instead of pseudo-continuous ASL, as the primary contrast mechanism for the BBB DW ASL sequence. This alteration to the sequence could simplify the overall fitting protocol especially in the instance of having multiple PLDs. This area is currently being pioneered by a researcher in the Laboratory of Functional MRI Technology (LOFT) at the University of Southern California (USC), which I will be joining as a postdoctoral scholar with the completion of the dissertation.

Furthermore, to reconcile the controversy in the opposing direction of Kw change with age and disease, future studies should find a way to merge MRI parametric scans with histological sections that

could give clues to the health of the underlying brain tissue. It may be insightful to include animal models where the integrity of the BBB could either be altered genetically through knocking out either the aquaporin or tight junction genes. By tightly regulating gene and protein expression, we could study whether these two BBB ASL sequences are in fact imaging distinct water exchange mechanisms (i.e. paracellular or transcellular). Finally, there exists pharmacological and ultrasound methods to open the BBB in both humans and animals. Mannitol, for instance, is an osmotic dilator that stretches the tight junctions between endothelial cells thereby allowing more water to traverse the BBB paracellularly. Focused ultrasound (FUS) is another method that rely on injection of microscopic microbubbles in the bloodstream and then applying ultrasound waves to cause these microbubbles to expand and contract to create a temporary mechanical force that loosens the endothelial tight junctions of brain capillary. Future studies involving these BBB ASL sequences could set up a before and after experiment utilizing either the pharmacological or mechanical techniques to open the BBB integrity to investigate the Kw magnitude and direction of change. Either way, given our current knowledge of the discrepancies and limitations of DW ASL, ME ASL, and DCE MRI, it seems reasonable that a clinically useful MRI imaging biomarker would incorporate information from multiple modalities to summarize the underlying Kw within each voxel of the scan as a proxy measure for the health of the underlying tissue.

To conclude, the field of BBB water exchange is one that emerged as a biproduct of the two-compartment model, which initially sought to make more accurate the assessment of cerebral perfusion with ASL MRI. This emerging method has garnered mounting evidence in the past two decades that suggest that there is pronounced changes in Kw with aging and with different neurological diseases affecting the cerebral vasculature. Thus, the current effort is to further validate this method through additional research studies with the aim toward the clinical adoption of this technique within the clinics.

References

1. Benveniste, H., et al., *The Glymphatic System and Waste Clearance with Brain Aging: A Review.* Gerontology, 2019. **65**(2): p. 106-119.
2. Hablitz, L.M. and M. Nedergaard, *The Glymphatic System: A Novel Component of Fundamental Neurobiology.* J Neurosci, 2021. **41**(37): p. 7698-7711.
3. Iliff, J.J., et al., *A Paravascular Pathway Facilitates CSF Flow Through the Brain Parenchyma and the Clearance of Interstitial Solutes, Including Amyloid b.* Science Translational Medicine, 2012. **4**(147).
4. Jessen, N.A., et al., *The Glymphatic System: A Beginner's Guide.* Neurochem Res, 2015. **40**(12): p. 2583-99.
5. Lun, M.P., E.S. Monuki, and M.K. Lehtinen, *Development and functions of the choroid plexus-cerebrospinal fluid system.* Nat Rev Neurosci, 2015. **16**(8): p. 445-57.
6. Fame, R.M. and M.K. Lehtinen, *Emergence and Developmental Roles of the Cerebrospinal Fluid System.* Dev Cell, 2020. **52**(3): p. 261-275.
7. Shen, M.D., *Cerebrospinal fluid and the early brain development of autism.* J Neurodev Disord, 2018. **10**(1): p. 39.
8. Ahmad, A., et al., *The Role of Neurovascular System in Neurodegenerative Diseases.* Mol Neurobiol, 2020. **57**(11): p. 4373-4393.
9. Johnson, S.E., et al., *Choroid plexus perfusion and intracranial cerebrospinal fluid changes after angiogenesis.* J Cereb Blood Flow Metab, 2020. **40**(8): p. 1658-1671.
10. Lehtinen, M.K., et al., *The choroid plexus and cerebrospinal fluid: emerging roles in development, disease, and therapy.* J Neurosci, 2013. **33**(45): p. 17553-9.
11. Mortazavi, M.M., et al., *The choroid plexus: a comprehensive review of its history, anatomy, function, histology, embryology, and surgical considerations.* Childs Nerv Syst, 2014. **30**(2): p. 205-14.
12. Sweeney, M.D., et al., *Blood-Brain Barrier: From Physiology to Disease and Back.* Physiol Rev, 2019. **99**(1): p. 21-78.
13. Dickie, B.R., G.J.M. Parker, and L.M. Parkes, *Measuring water exchange across the blood-brain barrier using MRI.* Prog Nucl Magn Reson Spectrosc, 2020. **116**: p. 19-39.
14. Xing, C.Y., et al., *Distribution of cardiac output to the brain across the adult lifespan.* J Cereb Blood Flow Metab, 2017. **37**(8): p. 2848-2856.
15. Moyaert, P., et al., *Imaging blood-brain barrier dysfunction: A state-of-the-art review from a clinical perspective.* Front Aging Neurosci, 2023. **15**: p. 1132077.
16. Herculano-Houzel, S., *The human brain in numbers: a linearly scaled-up primate brain.* Frontiers in Human Neuroscience, 2009. **3**.
17. Herbet, G. and H. Duffau, *Revisiting the Functional Anatomy of the Human Brain: Toward a Meta-Networking Theory of Cerebral Functions.* Physiol Rev, 2020. **100**(3): p. 1181-1228.
18. Fischl, B., *FreeSurfer.* Neuroimage, 2012. **62**(2): p. 774-81.
19. Padrela, B., et al., *Developing blood-brain barrier arterial spin labelling as a non-invasive early biomarker of Alzheimer's disease (DEBBIE-AD): a prospective observational multicohort study protocol.* BMJ Open, 2024. **14**(3): p. e081635.
20. Shao, X., et al., *Age-Related Decline in BBB Function is More Pronounced in Males than Females.* bioRxiv, 2024.
21. Padrela, B.E., et al., *Blood-brain barrier water permeability across the adult lifespan: A multi-echo ASL study.* Neurobiol Aging, 2025. **147**: p. 176-186.
22. Mader, S. and L. Brimberg, *Aquaporin-4 Water Channel in the Brain and Its Implication for Health and Disease.* Cells, 2019. **8**(2).
23. Bozkurt, A., H. Halici, and M. Yayla, *Aquaporins: Potential Targets in Inflammatory Diseases.* Eurasian J Med, 2023. **55**(1): p. 106-113.

24. Zihni, C., et al., *Tight junctions: from simple barriers to multifunctional molecular gates.* Nat Rev Mol Cell Biol, 2016. **17**(9): p. 564-80.
25. Heye, A.K., et al., *Assessment of blood-brain barrier disruption using dynamic contrast-enhanced MRI. A systematic review.* Neuroimage Clin, 2014. **6**: p. 262-74.
26. Rogosnitzky, M. and S. Branch, *Gadolinium-based contrast agent toxicity: a review of known and proposed mechanisms.* Biometals, 2016. **29**(3): p. 365-76.
27. Tofts, P.S., et al., *Estimating kinetic parameters from dynamic contrast-enhanced t1-weighted MRI of a diffusable tracer: Standardized quantities and symbols.* Journal of Magnetic Resonance Imaging, 1999. **10**(3): p. 223-232.
28. Heye, A.K., et al., *Tracer kinetic modelling for DCE-MRI quantification of subtle blood-brain barrier permeability.* Neuroimage, 2016. **125**: p. 446-455.
29. Fan, A.P., et al., *Comparison of cerebral blood flow measurement with [15O]-water positron emission tomography and arterial spin labeling magnetic resonance imaging: A systematic review.* J Cereb Blood Flow Metab, 2016. **36**(5): p. 842-61.
30. Watabe, H., et al., *PET kinetic analysis--compartmental model.* Ann Nucl Med, 2006. **20**(9): p. 583-8.
31. Chung, K.J., et al., *Quantitative PET imaging and modeling of molecular blood-brain barrier permeability.* medRxiv, 2024.
32. Williams, D.S., et al., *Magnetic resonance imaging of perfusion using spin inversion of arterial water.* Proc Natl Acad Sci U S A, 1992. **89**: p. 212-216.
33. Alsop, D.C., et al., *Recommended implementation of arterial spin-labeled perfusion mri for clinical applications- A consensus of the ismrm perfusion study group and the european consortium for asl in dementia.* Magnetic Resonance in Medicine, 2015.
34. Hernandez-Garcia, L., A. Lahiri, and J. Schollenberger, *Recent progress in ASL.* Neuroimage, 2019. **187**: p. 3-16.
35. Parkes, L.M. and P.S. Tofts, *Improved accuracy of human cerebral blood perfusion measurements using arterial spin labeling: accounting for capillary water permeability.* Magn Reson Med, 2002. **48**(1): p. 27-41.
36. St Lawrence, K.S., D. Owen, and D.J. Wang, *A two-stage approach for measuring vascular water exchange and arterial transit time by diffusion-weighted perfusion MRI.* Magn Reson Med, 2012. **67**(5): p. 1275-84.
37. Gregori, J., et al., *T2-based arterial spin labeling measurements of blood to tissue water transfer in human brain.* J Magn Reson Imaging, 2013. **37**(2): p. 332-42.
38. Detre, J.A., et al., *Applications of arterial spin labeled MRI in the brain.* J Magn Reson Imaging, 2012. **35**(5): p. 1026-37.
39. Alsop, D.C., et al., *Arterial spin labeling blood flow MRI: its role in the early characterization of Alzheimer's disease.* J Alzheimers Dis, 2010. **20**(3): p. 871-80.
40. Alsop, D.C., J.A. Detre, and M. Grossman, *Assessment of cerebral blood flow in Alzheimer's disease by spin-labeled magnetic resonance imaging.* Ann Neurol, 2000. **47**(1): p. 93-100.
41. Hu, W.T., et al., *Distinct cerebral perfusion patterns in FTLD and AD.* Neurology, 2010. **75**(10): p. 881-8.
42. St Lawrence, K.S., J.A. Frank, and A.C. McLaughlin, *Effect of restricted water exchange on cerebral blood flow values calculated with arterial spin tagging: a theoretical investigation.* Magn Reson Med, 2000. **44**(3): p. 440-9.
43. Li, Y., A. Sadiq, and Z. Wang, *Arterial Spin Labelling-Based Blood-Brain Barrier Assessment and Its Applications.* Investig Magn Reson Imaging, 2022. **26**(4): p. 229-236.
44. Wells, J.A., et al., *Characterizing the origin of the arterial spin labelling signal in MRI using a multiecho acquisition approach.* J Cereb Blood Flow Metab, 2009. **29**(11): p. 1836-45.
45. Ohene, Y., et al., *Non-invasive MRI of brain clearance pathways using multiple echo time arterial spin labelling: an aquaporin-4 study.* Neuroimage, 2019. **188**: p. 515-523.

46. Wells, J.A., et al., *Measuring biexponential transverse relaxation of the ASL signal at 9.4 T to estimate arterial oxygen saturation and the time of exchange of labeled blood water into cortical brain tissue.* J Cereb Blood Flow Metab, 2013. **33**(2): p. 215-24.
47. Wang, J., et al., *Arterial transit time imaging with flow encoding arterial spin tagging (FEAST).* Magn Reson Med, 2003. **50**(3): p. 599-607.
48. Buxton, R.B., et al., *A General Kinetic Model for Quantitative Perfusion Imaging with Arterial Spin Labeling.* Magnetic Resonance in Medicine, 1998.
49. Tee, M., et al., *Associations between potential risk factors and blood-brain barrier water permeability in middle-aged and older adults.* J Alzheimers Dis, 2025: p. 13872877251314138.
50. Lee, R.L. and K.E. Funk, *Imaging blood–brain barrier disruption in neuroinflammation and Alzheimer's disease.* Frontiers in Aging Neuroscience, 2023. **15**.
51. Montagne, A., et al., *Imaging subtle leaks in the blood-brain barrier in the aging human brain: potential pitfalls, challenges, and possible solutions.* Geroscience, 2022. **44**(3): p. 1339-1351.
52. Mahroo, A., et al., *Robust Multi-TE ASL-Based Blood-Brain Barrier Integrity Measurements.* Front Neurosci, 2021. **15**: p. 719676.
53. Schuenke M., E. Schulte, and S. U., *Thieme Atlas of Anatomy Head, Neck and Neuroanatomy, Second Edition*. Vol. 3. 2016, New York: Thieme Medical Publishers, Inc.
54. MacAulay, N., R.F. Keep, and T. Zeuthen, *Cerebrospinal fluid production by the choroid plexus: a century of barrier research revisited.* Fluids Barriers CNS, 2022. **19**(1): p. 26.
55. Liddelow, S.A., *Development of the choroid plexus and blood-CSF barrier.* Front Neurosci, 2015. **9**: p. 32.
56. Ghersi-Egea, J.F., et al., *Molecular anatomy and functions of the choroidal blood-cerebrospinal fluid barrier in health and disease.* Acta Neuropathol, 2018. **135**(3): p. 337-361.
57. Eisma, J.J., et al., *Choroid plexus perfusion and bulk cerebrospinal fluid flow across the adult lifespan.* J Cereb Blood Flow Metab, 2022: p. 271678X221129101.
58. Da Mesquita, S., et al., *Functional aspects of meningeal lymphatics in ageing and Alzheimer's disease.* Nature, 2018. **560**(7717): p. 185-191.
59. de Leon, M.J., et al., *Cerebrospinal Fluid Clearance in Alzheimer Disease Measured with Dynamic PET.* J Nucl Med, 2017. **58**(9): p. 1471-1476.
60. Serot, J.M., J. Zmudka, and P. Jouanny, *A possible role for CSF turnover and choroid plexus in the pathogenesis of late onset Alzheimer's disease.* J Alzheimers Dis, 2012. **30**(1): p. 17-26.
61. Tarasoff-Conway, J.M., et al., *Clearance systems in the brain-implications for Alzheimer disease.* Nat Rev Neurol, 2015. **11**(8): p. 457-70.
62. Bechter, K., et al., *Cerebrospinal fluid analysis in affective and schizophrenic spectrum disorders: identification of subgroups with immune responses and blood-CSF barrier dysfunction.* J Psychiatr Res, 2010. **44**(5): p. 321-30.
63. Choi, J.D., et al., *Choroid Plexus Volume and Permeability at Brain MRI within the Alzheimer Disease Clinical Spectrum.* Radiology, 2022: p. 212400.
64. Carroll, T.J., et al., *Quantification of cerebral perfusion using the "bookend technique": an evaluation in CNS tumors.* Magn Reson Imaging, 2008. **26**(10): p. 1352-9.
65. Aanerud, J., et al., *Sex differences of human cortical blood flow and energy metabolism.* J Cereb Blood Flow Metab, 2017. **37**(7): p. 2433-2440.
66. Kaur, C., G. Rathnasamy, and E.A. Ling, *The Choroid Plexus in Healthy and Diseased Brain.* J Neuropathol Exp Neurol, 2016. **75**(3): p. 198-213.
67. Vagal, A.S., et al., *The acetazolamide challenge: techniques and applications in the evaluation of chronic cerebral ischemia.* AJNR Am J Neuroradiol, 2009. **30**(5): p. 876-84.
68. Okudaira, Y., et al., *Evaluation of the Acetazolamide Test.* Stroke, 1995. **26**(7): p. 1234-1239.
69. Faraci F.M., Mayhan W.G., and H. D.D., *Vascular effects of acetazolamide on the choroid plexus.* The Journal of Pharmacology and Experimental Therapeutics, 1990. **254**.
70. Zhao, L., et al., *Non-invasive measurement of choroid plexus apparent blood flow with arterial spin labeling.* Fluids Barriers CNS, 2020. **17**(1): p. 58.

71. Johnson, S.E., et al., *Choroid plexus perfusion in sickle cell disease and moyamoya vasculopathy: Implications for glymphatic flow.* J Cereb Blood Flow Metab, 2021: p. 271678X211010731.
72. Storelli, L., et al., *A Fully Automatic Method to Segment Choroid Plexuses in Multiple Sclerosis Using Conventional MRI Sequences.* J Magn Reson Imaging, 2023.
73. Evans, P.G., et al., *Non-Invasive MRI of Blood-Cerebrospinal Fluid Barrier Function.* Nat Commun, 2020. **11**(1): p. 2081.
74. Petitclerc, L., et al., *Ultra-long-TE arterial spin labeling reveals rapid and brain-wide blood-to-CSF water transport in humans.* Neuroimage, 2021. **245**: p. 118755.
75. Ssali, T., et al., *A Noninvasive Method for Quantifying Cerebral Blood Flow by Hybrid PET/MRI.* J Nucl Med, 2018. **59**(8): p. 1329-1334.
76. Kuttner, S., et al., *Cerebral blood flow measurements with (15)O-water PET using a non-invasive machine-learning-derived arterial input function.* J Cereb Blood Flow Metab, 2021. **41**(9): p. 2229-2241.
77. Fan, A.P., et al., *Identifying Hypoperfusion in Moyamoya Disease With Arterial Spin Labeling and an [(15)O]-Water Positron Emission Tomography/Magnetic Resonance Imaging Normative Database.* Stroke, 2019. **50**(2): p. 373-380.
78. Zhao, M.Y., et al., *Cerebrovascular reactivity measurements using simultaneous (15)O-water PET and ASL MRI: Impacts of arterial transit time, labeling efficiency, and hematocrit.* Neuroimage, 2021. **233**: p. 117955.
79. Zhang, Y., M. Brady, and S.M. Smith, *Segmentation of brain MR images through a hidden Markov random field model and the expectation-maximization algorithm.* IEEE Trans Med Imaging, 2001. **20(1)**: p. 45-57.
80. Chappell, M.A., et al., *BASIL: A toolbox for perfusion quantification using arterial spin labelling.* Imaging Neuroscience, 2023. **1**: p. 1-16.
81. Parkes, L.M., *Quantification of cerebral perfusion using arterial spin labeling: two-compartment models.* J Magn Reson Imaging, 2005. **22**(6): p. 732-6.
82. Fan, A.P., et al., *Long-Delay Arterial Spin Labeling Provides More Accurate Cerebral Blood Flow Measurements in Moyamoya Patients: A Simultaneous Positron Emission Tomography/MRI Study.* Stroke, 2017. **48**(9): p. 2441-2449.
83. Khalighi, M.M., et al., *Image-derived input function estimation on a TOF-enabled PET/MR for cerebral blood flow mapping.* J Cereb Blood Flow Metab, 2018. **38**(1): p. 126-135.
84. Wolak, M.E., D.J. Fairbairn, and Y.R. Paulsen, *Guidelines for estimating repeatability.* Methods in Ecology and Evolution, 2012. **3**(1): p. 129-137.
85. Berridge, M.S., et al., *Measurement of human cerebral blood flow with [15O]butanol and positron emission tomography.* J Cereb Blood Flow Metab, 1991. **11**(5): p. 707-15.
86. Faraci F.M., et al., *Effects of vasoactive stimuli on blood flow to choroid plexus.* American Journal of Physiology, 1988.
87. Page, B.P., et al., *Choroid plexus blood flow in sheep.* Brain Research, 1980: p. 532-537.
88. Morris, E.D., et al., *Kinetic modeling in positron emission tomography.* Emission Tomorgraphy, 2004: p. 499-540.
89. Takata, K., et al., *Assessment of Arterial Transit Time and Cerebrovascular Reactivity in Moyamoya Disease by Simultaneous PET/MRI.* Diagnostics (Basel), 2023. **13**(4).
90. Madhukar, M., et al., *Choroid plexus: normal size criteria on neuroimaging.* Surg Radiol Anat, 2012. **34**(10): p. 887-95.
91. Asllani, I., A. Borogovac, and T.R. Brown, *Regression algorithm correcting for partial volume effects in arterial spin labeling MRI.* Magn Reson Med, 2008. **60**(6): p. 1362-71.
92. Petitclerc, L., et al., *Arterial Spin Labeling Signal in the CSF: Implications for Partial Volume Correction and Blood-CSF Barrier Characterization.* NMR Biomed, 2022: p. e4852.
93. Williamson, M.R., et al., *Acetazolamide Mitigates Intracranial Pressure Spikes Without Affecting Functional Outcome After Experimental Hemorrhagic Stroke.* Transl Stroke Res, 2019. **10**(4): p. 428-439.

94. Wardlaw, J.M., et al., *Perivascular spaces in the brain: anatomy, physiology and pathology.* Nat Rev Neurol, 2020. **16**(3): p. 137-153.
95. Goldwaser, E.L., et al., *Evidence of Neurovascular Water Exchange and Endothelial Vascular Dysfunction in Schizophrenia: An Exploratory Study.* Schizophr Bull, 2023.
96. Kamintsky, L., et al., *Blood-brain barrier imaging as a potential biomarker for bipolar disorder progression.* Neuroimage Clin, 2020. **26**: p. 102049.
97. van de Haar, H.J., et al., *Blood-Brain Barrier Leakage in Patients with Early Alzheimer Disease.* Radiology, 2016. **281**(2): p. 527-535.
98. van de Haar, H.J., et al., *Blood-brain barrier impairment in dementia: current and future in vivo assessments.* Neurosci Biobehav Rev, 2015. **49**: p. 71-81.
99. Shao, X., et al., *Comparison Between Blood-Brain Barrier Water Exchange Rate and Permeability to Gadolinium-Based Contrast Agent in an Elderly Cohort.* Frontiers in Neuroscience, 2020. **14**.
100. Tabanor, K., et al., *Brain Delivery of Drug and MRI Contrast Agent: Detection and Quantitative Determination of Brain Deposition of CPT-Glu Using LC-MS/MS and Gd-DTPA Using Magnetic Resonance Imaging.* Mol Pharm, 2016. **13**(2): p. 379-90.
101. Pullicino, R. and K. Das, *Is it safe to use gadolinium-based contrast agents in MRI?* J R Coll Physicians Edinb, 2017. **47**(3): p. 243-246.
102. Tiwari, Y.V., et al., *Diffusion-weighted arterial spin labeling MRI to investigate mannitol-induced blood brain barrier disruption.* Magn Reson Imaging, 2025: p. 110335.
103. Tanaka, F., et al., *Pseudocontinuous Arterial Spin Labeling: Clinical Applications and Usefulness in Head and Neck Entities.* Cancers (Basel), 2022. **14**(16).
104. Damestani, N.L., et al., *Associations between age, sex, APOE genotype, and regional vascular physiology in typically aging adults.* Neuroimage, 2023. **275**: p. 120167.
105. Liu, Y., et al., *Arterial spin labeling MRI study of age and gender effects on brain perfusion hemodynamics.* Magn Reson Med, 2012. **68**(3): p. 912-22.
106. Mutsaerts, H.J., et al., *Cerebral Perfusion Measurements in Elderly with Hypertension Using Arterial Spin Labeling.* PLoS One, 2015. **10**(8): p. e0133717.
107. Shao, X., et al., *Age-Related Decline in BBB Function is More Pronounced in Males than Females.* eLife, 2024.
108. Palomares, J.A., et al., *Water Exchange across the Blood-Brain Barrier in Obstructive Sleep Apnea: An MRI Diffusion-Weighted Pseudo-Continuous Arterial Spin Labeling Study.* J Neuroimaging, 2015. **25**(6): p. 900-5.
109. Gold, B.T., et al., *Water exchange rate across the blood-brain barrier is associated with CSF amyloid-beta 42 in healthy older adults.* Alzheimers Dement, 2021. **17**(12): p. 2020-2029.
110. Zachariou, V., et al., *Regional differences in the link between water exchange rate across the blood-brain barrier and cognitive performance in normal aging.* Geroscience, 2024. **46**(1): p. 265-282.
111. Morgan, C.A., et al., *Measurement of blood-brain barrier water exchange rate using diffusion-prepared and multi-echo arterial spin labelling: Comparison of quantitative values and age dependence.* NMR Biomed, 2024: p. e5256.
112. Shao, X., et al., *Quantification of blood-brain barrier water exchange and permeability with multidelay diffusion-weighted pseudo-continuous arterial spin labeling.* Magn Reson Med, 2023.
113. Shao, X., et al., *Mapping water exchange across the blood-brain barrier using 3D diffusion-prepared arterial spin labeled perfusion MRI.* Magn Reson Med, 2019. **81**(5): p. 3065-3079.
114. Wang, J., et al., *When perfusion meets diffusion: in vivo measurement of water permeability in human brain.* J Cereb Blood Flow Metab, 2007. **27**(4): p. 839-49.
115. Dai, W., et al., *Effects of arterial transit delay on cerebral blood flow quantification using arterial spin labeling in an elderly cohort.* J Magn Reson Imaging, 2017. **45**(2): p. 472-481.
116. Lu, H., et al., *Determining the longitudinal relaxation time (T1) of blood at 3.0 Tesla.* Magn Reson Med, 2004. **52**(3): p. 679-82.

117. Wright, P.J., et al., *Water proton T1 measurements in brain tissue at 7, 3, and 1.5 T using IR-EPI, IR-TSE, and MPRAGE: results and optimization.* MAGMA, 2008. **21**(1-2): p. 121-30.
118. Gudbjartsson, H. and S. Patz, *The rician distribution of noisy mri data.* Magnetic Resonance in Medicine, 1995. **34**: p. 910-914.
119. Woods, J.G., et al., *VESPA ASL: VElocity and SPAtially Selective Arterial Spin Labeling.* Magnetic Resonance in Medicine, 2022. **87**(6): p. 2667-2684.
120. Zawadzki, M., G. G.D., and N. W.R., *MP RAGE: a three-dimensional, T1-weighted gradient-echo sequence-initial experience in the brain.* Radiology, 1992. **182**: p. 769-775.
121. Jenkinson, M., et al., *Fsl.* Neuroimage, 2012. **62**(2): p. 782-90.
122. Rorden, C. and M. Brett, *Stereotaxic display of brain lesions.* Behav Neurol, 2000. **12**(4): p. 191-200.
123. Chen, Y., D.J. Wang, and J.A. Detre, *Comparison of arterial transit times estimated using arterial spin labeling.* MAGMA, 2012. **25**(2): p. 135-44.
124. Bhogal, A.A., et al., *Quantifying cerebral blood arrival times using hypoxia-mediated arterial BOLD contrast.* Neuroimage, 2022. **261**: p. 119523.
125. White, H. and B. Venkatesh, *Cerebral perfusion pressure in neurotrauma: a review.* Anesth Analg, 2008. **107**(3): p. 979-88.
126. Jacob, M. and D. Chappell, *Reappraising Starling: the physiology of the microcirculation.* Curr Opin Crit Care, 2013. **19**(4): p. 282-9.
127. Michel, C.C., T.E. Woodcock, and F.E. Curry, *Understanding and extending the Starling principle.* Acta Anaesthesiol Scand, 2020. **64**(8): p. 1032-1037.
128. Badaut, J., et al., *Blood-brain borders: a proposal to address limitations of historical blood-brain barrier terminology.* Fluids Barriers CNS, 2024. **21**(1): p. 3.
129. Daneman, R. and A. Prat, *The blood-brain barrier.* Cold Spring Harb Perspect Biol, 2015. **7**(1): p. a020412.
130. Greene, C., N. Hanley, and M. Campbell, *Blood-brain barrier associated tight junction disruption is a hallmark feature of major psychiatric disorders.* Transl Psychiatry, 2020. **10**(1): p. 373.
131. Cheslow, L. and J.I. Alvarez, *Glial-endothelial crosstalk regulates blood-brain barrier function.* Curr Opin Pharmacol, 2016. **26**: p. 39-46.
132. Mahroo, A., S. Konstandin, and M. Günther, *Blood–Brain Barrier Permeability to Water Measured Using Multiple Echo Time Arterial Spin Labeling MRI in the Aging Human Brain.* Journal of Magnetic Resonance Imaging, 2023. **59**(4): p. 1269-1282.
133. Lin, Z., et al., *Noncontrast assessment of blood-brain barrier permeability to water: Shorter acquisition, test-retest reproducibility, and comparison with contrast-based method.* Magn Reson Med, 2021. **86**(1): p. 143-156.
134. Powell, E., et al., *Blood-brain barrier water exchange measurements using FEXI: Impact of modeling paradigm and relaxation time effects.* Magn Reson Med, 2023. **90**(1): p. 34-50.
135. Ohene, Y., et al., *Increased blood-brain barrier permeability to water in the aging brain detected using noninvasive multi-TE ASL MRI.* Magn Reson Med, 2020.
136. Xu, Z., et al., *Tracer kinetic model detecting heterogeneous blood-brain barrier permeability to water and contrast agent in Alzheimer's disease and dementia with Lewy bodies.* Alzheimers Dement, 2025. **21**(2): p. e14529.
137. Mahroo, A., et al., *New physiological insights using multi-TE ASL MRI measuring blood-brain barrier water exchange after caffeine intake.* MAGMA, 2025. **38**(2): p. 207-219.
138. Mutsaerts, H., et al., *ExploreASL: An image processing pipeline for multi-center ASL perfusion MRI studies.* Neuroimage, 2020. **219**: p. 117031.
139. Mandal, P.K., R. Mahajan, and I.D. Dinov, *Structural brain atlases: design, rationale, and applications in normal and pathological cohorts.* J Alzheimers Dis, 2012. **31 Suppl 3**(0 3): p. S169-88.

140. Parkes, L.M., et al., *Normal cerebral perfusion measurements using arterial spin labeling: reproducibility, stability, and age and gender effects.* Magn Reson Med, 2004. **51**(4): p. 736-43.
141. Good, C.D., et al., *A voxel-based morphometric study of ageing in 465 normal adult human brains.* Neuroimage, 2001. **14**(1 Pt 1): p. 21-36.
142. Jernigan, T.L., et al., *Effects of age on tissues and regions of the cerebrum and cerebellum.* Neurobiology of Aging, 2001. **22**: p. 581-594.
143. Hafkemeijer, A., et al., *Associations between age and gray matter volume in anatomical brain networks in middle-aged to older adults.* Aging Cell, 2014. **13**(6): p. 1068-74.
144. Bi, B., D. Che, and Y. Bai, *Neural network of bipolar disorder: Toward integration of neuroimaging and neurocircuit-based treatment strategies.* Transl Psychiatry, 2022. **12**(1): p. 143.
145. Murray, C.J.L., et al., *The Global burden of disease : a comprehensive assessment of mortality and disability from diseases, injuries, and risk factors in 1990 and projected to 2020 : summary / edited by Christopher J. L. Murray, Alan D. Lopez*. 1996, World Health Organization: Geneva.
146. Charlson, F.J., et al., *Global Epidemiology and Burden of Schizophrenia: Findings From the Global Burden of Disease Study 2016.* Schizophr Bull, 2018. **44**(6): p. 1195-1203.
147. Liu S, Z.X., Sweeney JA, Gong Q, *Psychoradiology The Frontier of Neuroimaging in Psychiatry.* Radiology, 2016. **281**.
148. Nickl-Jockschat, T. and T. Abel, *Historical and Clinical Overview*, in *The Neurobiology of Schizophrenia*. 2016. p. 3-13.
149. Johnstone, E., et al., *Cerebral Ventricular Size and Cognitive Impairment in Chronic Schizophrenia.* The Lancet, 1976. **308**(7992): p. 924-926.
150. Kraguljac, N.V. and A.C. Lahti, *Neuroimaging as a Window Into the Pathophysiological Mechanisms of Schizophrenia.* Front Psychiatry, 2021. **12**: p. 613764.
151. Weinstein, J.J., et al., *Pathway-Specific Dopamine Abnormalities in Schizophrenia.* Biol Psychiatry, 2017. **81**(1): p. 31-42.
152. McGuire, P., et al., *Functional neuroimaging in schizophrenia: diagnosis and drug discovery.* Trends Pharmacol Sci, 2008. **29**(2): p. 91-8.
153. Potkin, S.G., et al., *The neurobiology of treatment-resistant schizophrenia: paths to antipsychotic resistance and a roadmap for future research.* NPJ Schizophr, 2020. **6**(1): p. 1.
154. North, H.F., et al., *Increased peripheral inflammation in schizophrenia is associated with worse cognitive performance and related cortical thickness reductions.* Eur Arch Psychiatry Clin Neurosci, 2021. **271**(4): p. 595-607.
155. Anisman, H. and Z. Merali, *Cytokines, stress and depressive illness: brain-immune interactions.* Ann Med, 2003. **35**(1): p. 2-11.
156. Hayley, S., P. Wall, and H. Anisman, *Sensitization to the neuroendocrine, central monoamine and behavioural effects of murine tumor necrosis factor-alpha: peripheral and central mechanisms.* Eur J Neurosci, 2002. **15**(6): p. 1061-76.
157. Kneeland, R.E. and S.H. Fatemi, *Viral infection, inflammation and schizophrenia.* Progress in neuro-psychopharmacology & biological psychiatry, 2013. **42**: p. 35-48.
158. Munshi, S., et al., *Repeated stress induces a pro-inflammatory state, increases amygdala neuronal and microglial activation, and causes anxiety in adult male rats.* Brain Behav Immun, 2020. **84**: p. 180-199.
159. Hong, J. and M. Bang, *Anti-inflammatory Strategies for Schizophrenia: A Review of Evidence for Therapeutic Applications and Drug Repurposing.* Clin Psychopharmacol Neurosci, 2020. **18**(1): p. 10-24.
160. Cho, M., et al., *Adjuvant use of anti-inflammatory drugs for schizophrenia: a meta-analytic investigation of randomized controlled trials.* Australian & New Zealand Journal of Psychiatry, 2019. **58**: p. 742-759.
161. Pollak, T.A., et al., *The blood–brain barrier in psychosis.* The Lancet Psychiatry, 2018. **5**(1): p. 79-92.

162. Sweeney, M.D., A.P. Sagare, and B.V. Zlokovic, *Blood-brain barrier breakdown in Alzheimer disease and other neurodegenerative disorders.* Nat Rev Neurol, 2018. **14**(3): p. 133-150.
163. van de Haar, H.J., et al., *Blood-Brain Barrier Leakage in Patients with Early Alzheimer Disease.pdf>.* Radiology, 2016.
164. Montagne, A., et al., *APOE4 leads to blood-brain barrier dysfunction predicting cognitive decline.* Nature, 2020. **581**(7806): p. 71-76.
165. Double, D. *The Limits of Psychiatry*. BMJ, 2002. **324**, 900-904.
166. McGinty, B., *The Future of Public Mental Health: Challenges and Opportunities.* The Milbank Quarterly, 2023. **101**: p. 532-551.
167. Decker, H.S., *The Development of DSM-III*, in *Oxford Research Encyclopedia of Psychology*. 2021.
168. Williams, L.M., *Precision psychiatry: a neural circuit taxonomy for depression and anxiety.* Lancet Psychiatry, 2016. **3**(5): p. 472-80.
169. Ivleva, E.I., H.B. Turkozer, and J.A. Sweeney, *Imaging-Based Subtyping for Psychiatric Syndromes.* Neuroimaging Clin N Am, 2020. **30**(1): p. 35-44.
170. Winship, I.R., et al., *An Overview of Animal Models Related to Schizophrenia.* Can J Psychiatry, 2019. **64**(1): p. 5-17.
171. Moussiopoulou, J., et al., *Higher blood-brain barrier leakage in schizophrenia-spectrum disorders: A comparative dynamic contrast-enhanced magnetic resonance imaging study with healthy controls.* Brain Behav Immun, 2025. **128**: p. 256-265.